CHEMISTRY-CLIMATE INTERACTIONS: BOUNDARY LAYER OZONE IN THE UNITED STATES AND FREE TROPOSPHERIC METHANESULFONIC ACID OVER THE TROPICS

A Dissertation
Presented to
The Academic Faculty

by

Yuzhong Zhang

In Partial Fulfillment
of the Requirements for the Degree
Doctor of Philosophy in the
School of Earth and Atmospheric Sciences

Georgia Institute of Technology
December 2015

CHEMISTRY-CLIMATE INTERACTIONS: BOUNDARY LAYER OZONE IN THE UNITED STATES AND FREE TROPOSPHERIC METHANESULFONIC ACID OVER THE TROPICS

Approved by:

Dr. Yuhang Wang, Advisor
School of Earth and Atmospheric Sciences
Georgia Institute of Technology

Dr. Paul Wine
School of Earth and Atmospheric Sciences
Georgia Institute of Technology

Dr. Greg Huey
School of Earth and Atmospheric Sciences
Georgia Institute of Technology

Dr. James Crawford
NASA Langley Research Center

Dr. Rodney Weber
School of Earth and Atmospheric Sciences
Georgia Institute of Technology

Date Approved: November 6, 2015

To my parents

ACKNOWLEDGEMENTS

I would like to start by thanking my advisor, Dr. Yuhang Wang, for his support and guidance throughout my Ph.D. I have been benefitted from not only his knowledge and insights, but also his passion for science and dedication to high standards. I am also grateful for my Ph.D. thesis committee members, Dr. Greg Huey, Dr. Rodney Weber, Dr. Paul Wine, and Dr. James Crawford, for their review of my dissertation and for their comments and suggestions.

Thanks also go to all the current members and alumni of Yuhang Wang's group. I have enjoyed my time working with Dr. Zhen Liu, Dr. Dasa Gu, Dr. Ja-Ho Koo, Dr. Yongjia Song, Dr. Tao Zeng, Charles Smeltzer, Yufei Zou, Tom Loadholt, Ruixiong Zhang, Hang Qu, Ye Cheng, Jianfeng Li, Ziming Ke, and Ran Yin. I am also grateful for the DISCOVER-AQ and PASE science team. The data they collected are important foundations of this work. I also thank my coauthors, especially Dr. James Crawford, Dr. Gao Chen, and Burton Gray, for the constructive and insightful discussions.

I am also grateful that I have made many good friends at Georgia Tech. I shared with them interesting discussions, fun events, and precious moments.

Finally, I would like to express my deepest gratitude to my parents for their unending love and support. This work would not have been possible without their constant encouragement throughout my life.

TABLE OF CONTENTS

LIST OF TABLES

LIST OF FIGURES

LIST OF SYMBOLS AND ABBREVIATIONS

SYMBOLS

CO	carbon moxide
CH_2O	formaldehyde
H_2O	water
NO	nitric oxide
NO_2	nitrogen dioxide
NO_x	nitrogen oxides
$N(O_3)$	net chemical production of ozone
O_3	ozone
$[O_3]_{MDA8}$	daily maximum 8-hour average ozone mixing ratio
$O(^1D)$	first electronically excited state of the oxygen atom
OH	hydroxyl radical
PAN	peroxyacyl nitrates
$P(O_3)$	chemical production of ozone
SO_2	sulfur dioxide
T_{max}	daily maximum temperature
τ_c	chemical life time
τ_m	vertical mixing time scale

ABBREVIATIONS

1-D	one-dimensional
3-D	three-dimensional
AMF	air mass factor

ACM2	the asymmetric convective model, version 2 boundary layer scheme
BL	boundary layer
CA	the state of California in the U.S.
CFSR	the Climate Forecast System Reanalysis
DISCOVER-AQ	Deriving Information on Surface Conditions from Column and Vertically Resolved Observations Relevant to Air Quality
DMS	dimethyl sulfide
DMSO	dimethyl sulfoxide
ECDF	empirical cumulative distribution function
EPA	the Environmental Protection Agency
EVD	Explained Variance Decomposition
GOME-2	the Global Ozone Monitoring Experiment-2
GFED	the Global Fire Emission Database
GL	the Great Lakes region in the U.S.
HTAP	the Task Force on Hemispheric Transport of Air Pollutants
MBL	marine boundary layer
MEGAN	the Model of Emissions of Gases and Aerosols from Nature
MODIS	Moderate Resolution Imaging Spectroradiometer
MYJ	Mellor–Yamada–Janjic boundary layer scheme
MSA	methanesulfonic acid
MSIA	methane sulfinic acid
MW	the Midwest region in the U.S.
LFT	lower free troposphere
LT	local time
NE	the Northeast U.S.

PASE	the Pacific Atmospheric Sulfur Experiment
REAM	Regional chEmistry trAnsport Model
RH	relative humidity
RUC	Rapid Update Cycle land-surface scheme
SE	the Southeast U.S.
VOC	Volatile Organic Compounds
VPD	vapor pressure deficit
WRF	the Weather Reanalysis and Forecast model
YSU	the Yonsei University boundary layer scheme

SUMMARY

The chemistry-climate interaction is a two-way process: Atmospheric chemistry can interfere with the radiation budget and subsequently the climate system and climate change, through its impact on atmospheric chemistry, may pose challenges to air quality management. A good understanding of the interactions between atmospheric chemistry and climate is an important piece of information for human to cope with climate change and its consequences. This dissertation employs multi-scale modeling analysis to explore two subtopics pertaining to the chemistry-climate interaction: (1) ground-level ozone pollution in the United States and (2) the marine sulfur chemistry over the tropical oceans.

In contrast to the decreasing trend in ozone concentrations in July resulting mainly from emission reduction, analysis of long-term (1980-2010) surface ozone data finds no appreciable trend during October over the southeast U.S., implicating that the benefit from emission reduction might be diminished by climate change. To understand the drivers for high ozone episodes during the fall, we use a 3-D chemical transport model to analyze the month of October 2010, the most recent ozone extreme over the Southeast in October. Analysis of meteorological conditions shows that the high ozone concentrations are due in part to a dry and warm weather condition, which enhances photochemical production and reduces pollution ventilation. Observational evidence and modeling analysis indicate that another contributor is enhanced emission of biogenic isoprene, a major ozone precursor, from water stressed plants under a dry and warm condition. The latter finding is corroborated by recent laboratory studies. This finding implicates that a drying and warming future, projected by climate models, will likely lead

to ventilation reduction, more biogenic isoprene emissions, an extended ozone season from summer to fall, and an increase of secondary organic aerosols in the Southeast U.S.

We use vertical profiles observed in the DISCOVER-AQ aircraft campaign in July 2011 to examine how NO_x, an important ozone precursor, distributes vertically in the boundary layer and how the vertical distribution is affected by meteorological or climate factors. In contrast to an even distribution in a well-mixed boundary layer, an often-used assumption in air pollution studies, the observed average vertical profile of NO_x shows a large negative gradient with increasing altitude in the boundary layer. Our analysis suggests that the magnitude of the NO_x gradient is highly sensitive to meteorological factors such as atmospheric stability. Using a 1-D chemical transport model, we reasonably reproduce the vertical profiles of NO_x under different boundary layer stability conditions, classified based on potential temperature gradient and boundary layer height. We also use this 1-D model to investigate the impact of parameterizations of the boundary layer and land-surface processes on vertical profiles. Using model simulations, we evaluate the impact of boundary layer NO_x gradient on the calculation of the ozone production rate and satellite NO_2 retrieval. We show that using surface measurements and the well-mixed boundary layer assumption causes a ~45% high bias in the estimated boundary layer ozone production rate and that the variability of NO_2 vertical profiles is responsible for 5~10% variability in the retrieved NO_2 tropospheric vertical columns.

Using the 1-D model, we also examine the sulfur chemistry during the PASE mission in the tropical Pacific. The production of sulfate aerosols through sulfur chemistry in marine environments is critical to the tropical climate system. Our work

focuses on methanesulfonic acid (MSA), a critical compound that has not been studied in detail. The observed sharp decrease in MSA from the surface to 600m implies a surface source of 4.0×10^7 molecules/cm^2/s. Evidence suggests that this source is photolytically enhanced in daytime. We also find that the observed large increase of MSA from the boundary layer into the lower free troposphere (1000-2000m) results mainly from the degassing of MSA from dehydrated aerosols. We estimate a source of 1.2×10^7 molecules/cm^2/s to the free troposphere through this pathway. This source of soluble MSA could potentially provide an important precursor for new particle formation in the free troposphere over the tropics, affecting the climate system through aerosol-cloud interactions.

CHAPTER 1

INTRODUCTION

1.1 Statement of the Problem

Atmospheric chemistry is a critical process in the Earth system that produces, transforms, and removes the trace gas and particle constituents in the atmosphere. Although only accounting for a small fraction of the atmosphere, these gas and particle constituents actively interact with other components of the Earth system and are key to many environmental issues such as photochemical smog, acid rain, and climate change. Being one of the greatest challenges to the human society, climate change, through its impact on atmospheric chemistry, may add to the difficulty of treating other environmental problems (e.g., air pollution). On the other side, species involved in atmospheric chemistry (e.g., aerosols) can interfere with the radiation budget and subsequently the climate system. Therefore, a good understanding of the interactions between atmospheric chemistry and climate provides an important piece of information for human to cope with climate change and its consequences.

In this dissertation, I will focus on two topics pertaining to chemistry-climate interactions: (1) ground-level ozone pollution in the United States and (2) the marine sulfur chemistry over the tropical oceans. In the former topic, I will investigate climate factors that affect ground-level ozone extremes and vertical distributions of ozone precursors. In the latter topic, I will explore the marine sulfur chemistry that modulates the climate system through the production of scattering aerosols, with a focus on the surface and tropospheric sources of methanesulfonic acid (MSA).

1.1.1 Challenges of Climate Change to the Ground-level Ozone Control

Harmful to the health of human [*Brunekreef and Holgate*, 2002] and vegetation [*Reich and Amundson*, 1985], high level of ground-level ozone is a long-standing

environmental problem in the United States and many other countries. Tropospheric ozone is produced through photochemical reactions of nitrogen oxides (NO_x=NO+NO_2) and volatile organic compounds (VOC), the so-called ozone precursors. In the past several decades, to control the ozone pollution, tremendous efforts have been devoted to reducing the anthropogenic emissions of these precursors. Figure 1.1 shows that the emissions of VOC and NO_x in the U.S. have been almost halved from 1970 to 2014 [*EPA*, 2015]. The significant reduction of anthropogenic ozone precursors contributes to the decrease of ozone pollution in the U.S., especially during the summer when photochemistry and ozone production is active. For example, linear regression analysis finds that daily maximum 8-hour average ozone ($[O_3]_{MDA8}$) decreased by 0.46 ppbv/yr and 0.20 ppbv/yr in the northeast (NE) U.S. and southeast (SE) U.S., respectively, during the past three decades (Figure 1.2).

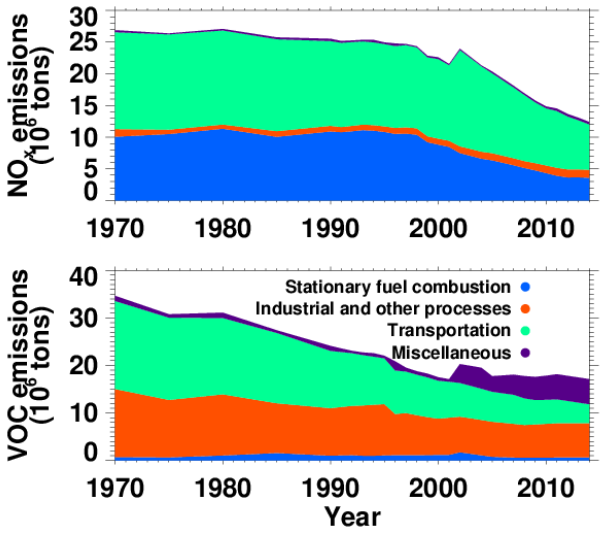

Figure 1.1 Emissions of NO_x and VOC from different sectors in the U.S. from 1970 to 2014. Adapted from *EPA* [2015].

In addition to anthropogenic emissions, it is also well known that ground-level ozone is also influenced by weather and climate [e.g., *Jacob and Winner*, 2009; *Camalier et al.*, 2007]. Trends or cycles of global and regional climate can perturb ground-level ozone on a decadal and regional scale, potentially posing great challenges to air quality

control. Previous climate-chemistry models projections show that, holding anthropogenic emissions constant, ground-level ozone will increase during the ozone season (i.e., summer) over many regions in the U.S. in next 50 years [*Avise et al.*, 2009; *Chen et al.*, 2009; *Nolte et al.*, 2008]. Moreover, modeling and statistical analysis also suggest that some regions are likely to experience an extension of the ozone season into the fall [*Avise et al.*, 2009; *Bloomer et al.*, 2010; *Camalier et al.*, 2007; *Chen et al.*, 2009; *Nolte et al.*, 2008].

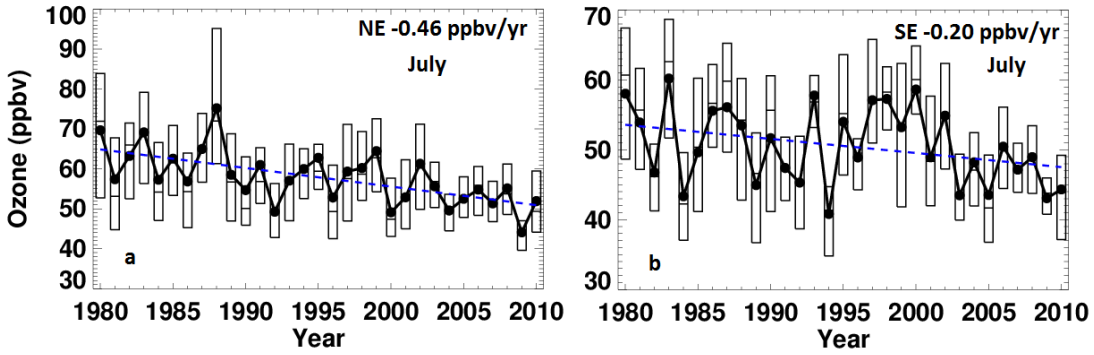

Figure 1.2 The trend of monthly $[O_3]_{MDA8}$ over (a) NE and (b) SE in July from 1980 to 2010.

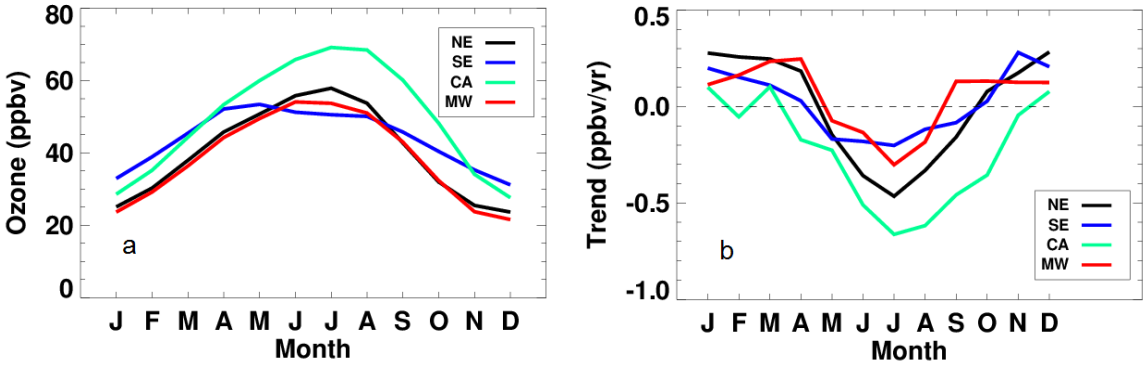

Figure 1.3 (a) The climatological mean of $[O_3]_{MDA8}$ and (b) the linear trend of $[O_3]_{MDA8}$ over NE, SE, CA, and GL regions from 1980 to 2010.

In contrast to the decreasing ozone in the summer months, long-term ground-level ozone observations show a negligible or slightly positive trend in October over the NE, SE, and the Midwest (MW) (Figure 1.3), suggesting that either ozone concentrations are

insensitive to the large emission reduction in the past three decades or the emission reduction benefit is negated by regional climate change during October. Variance decomposition analysis of the long-term data in the SE shows that inter-annual variance is significantly larger in 2000s than that in 1980s and 1990s, which is likely a manifestation of regional climate impact (Figure 1.4).

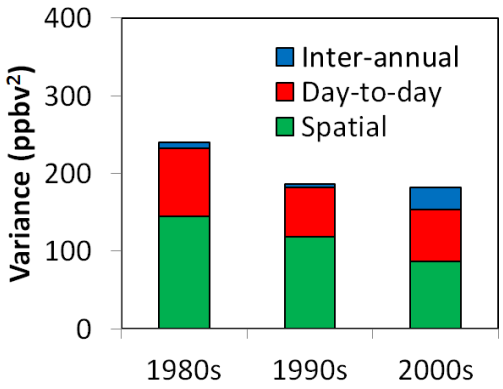

Figure 1.4 Variance decomposition of ground-level ozone observations over the SE in 1980s, 1990s, and 2000s into inter-annual, day-to-day, and spatial variance.

The growing climate influence and the extension of the ozone season pose new challenges to air quality managers to control the ozone pollution. Previous chemistry-climate model projections show large variation in the sign and magnitude of the predicted ozone change during the fall, especially over forested regions such as the SE [*Camalier et al.*, 2007; *Chen et al.*, 2009; *Nolte et al.*, 2008]. The lack of a consensus reflects the uncertainties in modeling regional climate change and the consequent response of ground-level ozone.

1.1.2 Links between Climate Factors and Ground-level Ozone

It has well known that ground-level ozone relates closely with meteorological factors. A long-term trend or cycle of these meteorological parameters can impact ground-level ozone on a climate scale.

The relations between climate factors and ground-level ozone are manifold: (1) Factors such as temperature and humidity influence the natural emissions of ozone precursors such as soil NO_x [*Wang et al.*, 1998], lightning NO_x [*Wang et al.*, 1998], and biogenic isoprene [*Guenther et al.*, 2006; *Pegoraro et al.*, 2007]; (2) Cloud fractions and thickness affect the downward radiation reaching the boundary layer (BL), which is the driver of photochemistry [*Voulgarakis et al.*, 2009]; (3) Meteorological factors such as temperature and humidity influence reaction rates of some key reactions in ozone chemistry, including PAN dissociation [*Racherla and Adams*, 2008] and primary OH production from $O(^1D)$ and H_2O [*Johnson et al.*, 1999; *Dawson et al.*, 2007]; (4) A stable BL reduces the vertical ventilation of ozone and its precursors; (5) Wind patterns determine the horizontal transport of ozone and its precursors [*Fu et al.*, 2015]; (6) The wave activity in the upper troposphere can lead to downward transport of ozone to the ground, found to be important in high-elevated areas [*Lin et al.*, 2015]. Moreover, varied meteorological factors are often inter-related. For example, under the high pressure system, multiple factors such as clear sky, stagnant BL, slow wind, and high temperature all contribute to enhancing ground-level ozone. Studies have reported that the frequency of summertime mid-latitude cyclones across eastern North America [*Leibensperger et al.*, 2008] and the westward extension of the Bermuda high [*Zhu and Liang*, 2013] are strong predictors of ozone pollution in the eastern U.S.

1.1.3 The "Well-mixed" Boundary Layer Assumption and Vertical Distribution of Ozone Precursors

The vertical distribution of air pollutants in the boundary layer (BL) is a complex function of emissions, advection, chemistry, and turbulent mixing. Since the lifetime of ozone is relatively long (several days), ground-level ozone concentrations are closely related to the boundary layer (BL) integrated production rather than the surface

production. Therefore, ground-level ozone concentration depends on the vertical distribution of ozone precursors in the BL. Based on the reasoning that vigorous turbulent mixing in the BL is much faster than chemical loss for many species of interest, air pollution studies often assume a well-mixed boundary layer, where pollutants are evenly distributed. This assumption enables researchers to infer average conditions in the BL from surface observations [e.g., *Petritoli et al.*, 2004; *Fiedler et al.*, 2005; *Leigh et al.*, 2007; *Lee-Taylor et al.*, 2011; *de Arellano et al.*, 2011; *Knepp et al.*, 2013] and thus greatly extends the use of surface measurements. Because of the difficulty in obtaining vertically-resolved measurements, the validity of the assumption has not been well evaluated. Moreover, the impact of meteorological/climate parameters on the vertical distribution of precursors is potentially an important factor that affects the response of ozone production to climate change, which is also not well evaluated before.

In an emission region under a minor advection condition, the well-mixed BL assumption readily works as a first-order approximation for long-lived species such as carbon monoxide and ethane but is invalid for very reactive species such as isoprene. However, for moderately reactive species which has a chemical life time comparable to the BL mixing time scale, the validity of the well-mixed BL assumption over emission regions and its implications have not been evaluated. One such species is nitrogen oxides (NO_x=NO_2+NO), a major precursor for ozone [*Liu et al.*, 1992; *Chameides et al.*, 1992], nitrate aerosol [*Bassett and Seinfeld*, 1983], and secondary organic aerosol [*Ng et al.*, 2007]. Loss of NO_x through formation of nitric acid and organic nitrates results in a NO_x chemical life time of several hours in daytime, which is comparable to the BL mixing time scale, indicating that the vertical distribution of NO_x may be sensitive to the relative

importance between chemical loss and turbulent mixing. Inadequate knowledge of the vertical distributions of NO_x can lead to biases in a variety of calculations, for example, the calculation of the BL-average ozone production rate [*Liu et al.*, 2012a] and satellite NO_2 retrieval [*Boersma et al.*, 2004; *Gu et al.*, 2014].

1.1.4 The Impact of Marine Sulfur Chemistry on Climate

Organic sulfur is emitted from the ocean and, through oxidation, produces sulfate aerosols, which is critical to the tropical climate system [e.g., *Charlson et al.*, 1987]. Since the discovery that dimethyl sulfide (DMS) is emitted in large quantities from the ocean [*Barnard et al.*, 1982], marine sulfur chemistry has been studied extensively. The oxidation of DMS is mainly by the hydroxyl radical (OH), which converts more than half of DMS to sulfur dioxide (SO_2) [*Davis et al.*, 1998; *Davis et al.*, 1999; *Chen et al.*, 2000; *Wang et al.*, 2001]. Further oxidation of SO_2 in the gas or aerosol phase produces sulfuric acid (H_2SO_4), which can either condense onto existing particles or form new particles under favorable conditions [*Davis et al.*, 1999; *Mauldin et al.*, 1999; *Weber et al.*, 2001]. In addition to SO_2 and H_2SO_4, marine sulfur chemistry also involves other sulfur-containing compounds such as dimethyl sulfoxide (DMSO), methane sulfinic acid (MSIA), and methanesulfonic acid (MSA). These species, although believed to be important, have not been studied as extensively as DMS and SO_2.

During the Pacific Atmospheric Sulfur Experiment (PASE) over the tropical Pacific in August and September of 2007, the vertical distributions of a relatively complete set of sulfur-containing compounds, including DMS, SO_2, H_2SO_4, and MSA, were measured, providing observational constraints to test our understanding of sulfur chemistry in the marine boundary layer (MBL) and lower free troposphere (LFT) over

tropical regions. Model analysis shows that although simulated vertical profiles of DMS and SO_2 are in reasonable agreement with observations [*Gray et al.*, 2011], the model underestimates MSA in the MBL and the LFT.

1.2 Description of the Chemical Transport Model

To explore the topics outlined in Section 1.1, we take a multi-scale modeling approach using the Regional chEmical trAnsport Model (REAM). Specifically, we use the 1-D REAM to analyze the aircraft campaign data to understand the vertical distributions of species; and we use the 3-D REAM to analyze the factors that affect regional ozone extreme episodes.

1.2.1 3-D REAM

We use the 3-D REAM to explore the mechanisms behind regional ozone extreme episodes in the SE U.S. in the fall. The 3-D REAM has been applied over North America, East Asia, and the Polar Regions [*Choi et al.*, 2005; *Choi et al.*, 2008a; *Choi et al.*, 2008b; *Zhao and Wang*, 2009; *Zhao et al.*, 2009a; *Zhao et al.*, 2009b; *Yang et al.*, 2010; *Zhao et al.*, 2010; *Liu et al.*, 2012b; *Gu et al.*, 2013; *Gu et al.*, 2014]. The model has a horizontal resolution of 36 km and 30 vertical layers in the troposphere. Transport is driven by the Weather Research and Forecasting (WRF) model assimilated meteorological fields constrained by the CFSR data. Most meteorological inputs are archived every 30 min except those related to convective transport and lightning parameterizations, which are archived every 5 min. Chemical initial and boundary conditions in the REAM are obtained from the global simulation for the same period using the GEOS-CHEM model (v9-02) driven by GEOS-5 assimilated meteorological fields [*Bey et al., 2001*].

The chemistry mechanism is adopted from GEOS-Chem v9-02 with expansion on aromatics chemistry [*Liu et al.*, 2010]. The anthropogenic emissions are from the emission inventory of 2010 for the Task Force on Hemispheric Transport of Air Pollution version two (HTAPv2). The biogenic isoprene emissions are calculated using the Model of Emissions of Gases and Aerosols from Nature (MEGAN v2.1) algorithm, which take into account factors such as temperature, solar radiation, leaf area index, and vegetation functional type. The leaf area index that fed into the MEGAN module was from the Moderate Resolution Imaging Spectroradiometer (MODIS, MOD15A2). Cloud fraction and optical depth are calculated based on WRF meteorological fields [*Choi et al.*, 2008a].

1.2.2 1-D REAM

To facilitate the use of aircraft measurements to constrain the model, we use the 1-D REAM to analyze the vertical profile of NO_x during DISCOVER-AQ 2011 and MSA during the PASE. The 1-D REAM has been applied to analyze the campaign measurements in China [*Liu et al.*, 2010; *Liu et al.*, 2012a; *Liu et al.*, 2014], at the South Pole [*Wang et al.*, 2007], and over the tropical Pacific [*Gray et al.*, 2011; *Zhang et al.*, 2014]. The 1-D REAM is a column chemical transport model that inherits relevant modules for photochemistry, convective transport, vertical diffusion, and wet/dry deposition from the original 3-D REAM. Similar to 3-D REAM, meteorological parameters (e.g., water vapor concentrations, temperature, pressure, and the diffusion coefficient) are also obtained from WRF assimilation. For the PASE study, we add a sulfur chemistry module including six sulfur chemistry reactions (Table 1.1).

Table 1.1 Gas-phase sulfur reactions and rate constants. Adapted from Zhu et al. [2006].

Reaction	Rate constants, k(T), cm^3 $molec^{-1}$ s^{-1}
$DMS + OH \rightarrow 0.9SO_2 + 0.1H_2SO_4$	[a] $1.10\times10^{-11}\exp(-240/T)$
$DMS + OH \rightarrow 0.5DMSO + 0.2DMSO_2 + 0.3MSIA$	$\frac{1.0\times10^{-39}\exp(5820/T)[O_2]}{1+5.0\times10^{-30}\exp(6280/T)[O_2]}$
$DMSO + OH \rightarrow 0.9MSIA + 0.1DMSO_2$	9.0×10^{-11}
$MSIA + OH \rightarrow 0.9SO_2 + 0.1MSA$	9.0×10^{-11}
$SO_2 + OH \rightarrow H_2SO_4$	[b] $F\times K_0\times K_\infty/(K_0+K_\infty)$
$DMS + BrO \rightarrow DMSO + MSIA$	$1.4\times10^{-14}\exp(940/T)$

[a] *Sander et al.* (2006)
[b] $\log F = \log(0.525)/(1+[\log(k_0/k_\infty)]^2)$, $k_0 = 4.5\times10^{-31}(T/300)^{-3.9}$ [M], $k_\infty = 1.26\times10^{-12}(T/300)^{-0.7}$

1.3 Scope of This Work

Combining multi-scale modeling analysis with statistical analysis, this dissertation (1) identifies key climate factors that drives extreme episodes of ground-level ozone during the fall; (2) investigates the sensitivity of NO_x vertical gradient to the BL stability; and (3) explores the missing sources of MSA in the MBL and the LFT over the tropical Pacific.

Specifically, the remainder of this dissertation is organized as follows.

Chapter 2, "Climate driven ground-level ozone extremes in the Southeast United States during the fall," analyzes the recent ozone extreme over the SE in October, 2010. Analysis shows that a dry and warm weather condition that enhances photochemical production and reduces pollution ventilation contributes to the episodes. In addition, observational evidence and modeling analysis indicate that another contributor is enhanced biogenic isoprene from water stressed plants under a dry and warm condition. This result implicates a novel climate-biosphere-chemistry interaction mechanism. Simulations show that the ground-level ozone is more sensitive to biogenic

isoprene during the fall than during the summer, indicating that this mechanism is likely to be a significant factor pertaining to the issue of extended ozone season.

Chapter 3, "Large vertical gradient of reactive nitrogen oxides in the boundary layer," examines the vertical distributions of pollutants over the Washington-Baltimore area measured during the DISCOVER-AQ 2011 aircraft campaign. The observed NO_x, an important ozone precursor, show a large negative gradient with increasing altitude in the BL. Our analysis shows the magnitude of the NO_x vertical gradient is highly sensitive to atmospheric stability, which is likely to change in response to climate change. Using 1-REAM simulations, the chapter also evaluates (1) the variation in vertical NO_x profiles resulting from varied parameterizations of the BL and land-surface processes; (2) the bias in the BL-averaged ozone production rate by extrapolating surface measurements to the entire BL; and (3) the impact of temporal variability of NO_2 vertical profiles on the satellite retrieval of NO_2 tropospheric vertical columns.

Chapter 4, "Surface and tropospheric sources of methanesulfonic acid (MSA) over the tropical Pacific Ocean," investigates the missing surface and tropospheric sources MSA over the tropical Pacific Ocean. The observed sharp decrease in MSA from the surface to 600m implies a surface source that is likely to be photolytical in nature. The observed large increase of MSA from the MBL into the LFT (1000-2000m) results mainly from the degassing of MSA from dehydrated aerosols. This source potentially provides an important precursor for new particle formation in the free troposphere over the tropics, affecting the climate system through aerosol-cloud interactions.

Chapter 5, "Conclusions and Future Work," summarizes the findings in Chapter 2-4 and make recommendations for the future work.

CHAPTER 2

[1]CLIMATE DRIVEN GROUND-LEVEL OZONE EXTREMES IN THE SOUTHEAST UNITED STATES DURING THE FALL

2.1 Introduction

Ground-level ozone is an air pollutant that adversely affects the health of humans and ecosystems [*Brunekreef and Holgate,* 2002; *Reich and Amundson,* 1985]. High ground-level ozone events are typically found in the summer when the formation of ozone is active through photochemical reactions of nitrogen oxides (NO_x=NO+NO_2) and volatile organic compounds (VOCs). However, ozone concentrations are sensitive to weather and climate [e.g., *Jacob and Winner*, 2009] and the high-ozone season could extend beyond summer in the future [*Avise et al.*, 2009; *Bloomer et al.*, 2010; *Camalier et al.*, 2007; *Chen et al.*, 2009; *Nolte et al.*, 2008]. Previous climate-chemistry model studies estimated the change of ground-level ozone (ΔO_3) in the U.S. resulting only from climate change. These results show large variation in the sign and magnitude of ΔO_3 in the fall, especially over forested regions such as the southeastern U.S. (SE) [*Camalier et al.*, 2007; *Chen et al.*, 2009; *Nolte et al.*, 2008]. The lack of a consensus reflects the uncertainties in modeling regional climate change and the consequent response of ground-level ozone. Although the impact of meteorology and climate on ozone during the summer ozone season has been extensively studied [*Bloomer et al.*, 2010; *Bloomer et al.*,

---

[1] This chapter is an extension of "Climate driven ground-level ozone extreme in the fall over the Southeast United States," in preparation. Co-authors are Yuhang Wang, Tao Zeng, and Yongjia Song.

2009; *Leibensperger et al.*, 2008; *Olszyna et al.*, 1997; *Steiner et al.*, 2010], much less efforts have been devoted to understand the climate response of ozone in the fall.

Most of present studies on the climate impact on ground-level ozone focus on the ozone-temperature relationship [*Jacob and Winner*, 2009; *Rasmussen et al.*, 2012; *Rasmussen et al.*, 2013; *Wu et al.*, 2008]. Although good correlations between ground-level ozone and temperature are observed in many places and seasons, model analysis shows that the direct impact of temperature on ground-level ozone, mainly through PAN chemistry and biogenic isoprene emissions [e.g., *Racherla and Adams*, 2008], cannot fully explain the observed ozone-temperature sensitivity. Many other indirect mechanisms that correlate with temperature contribute to the ozone-temperature sensitivity, including regional transport, ventilation, and cloudiness [*Voulgarakis et al.*, 2009; *Zhu and Liang*, 2013; *Fu et al.*, 2015; *Lin et al.*, 2015]. Their correlations with temperature may vary with time and locations. Therefore, in the case of surface ozone, temperature is just a surrogate of all meteorological or climate factors and can be unreliable or misleading. To truly understand the climate penalty for ground-level ozone, it is important to figure out how the correlations between these mechanisms and temperature vary with time and location and whether other critical mechanisms exist.

The remainder of this chapter will proceed as follows. Section 2.2 describes the long-term ozone (Section 2.2.1) and isoprene (Section 2.2.2) data from EPA ground monitoring stations, long-term meteorological reanalysis data (Section 2.2.3), GOME-2 satellite formaldehyde data (Section 2.2.4), 3-D REAM model experiments (Section 2.2.5), and statistical analysis methods (Section 2.2.6). Section 2.3.1 examines the fall high ozone extremes over the SE in last three decades. Using statistical analysis, Section

2.3.2 finds humidity being a good predictor of ground-level ozone over the SE during October. Section 2.3.3 applies model simulations to study the high-ozone extreme in October 2010 and finds underestimation of ozone by the model during the episodes. Section 2.3.4 proposes a humidity-driven mechanism that explains the underestimation and presents modeling, observational, and laboratory evidence that supports the hypothesis. Section 2.3.5 demonstrates that alternative explanations are unlikely to explain the model bias. Finally, in Section 2.4, we summarize our findings and discuss the implications of our findings to the regional air pollution management in the context of climate change.

2.2 Data and Methods

2.2.1 EPA Ground-level Ozone Observations

We downloaded the hourly ground-level ozone measurements (1980-2010) from the EPA Data Mar (https://ofmext.epa.gov/AQDMRS/aqdmrs.html). Among ~1500 stations across the U.S. in the dataset, 18.6%, 38.0%, and 41.3 are classified as urban, suburban, and rural sites. The site type is unknown for about 2.1% sites. Figure 2.1 plots the distribution of these sites. To obtain a policy-relevant measure, we calculated the maximum daily 8-hour average ozone ($[O_3]_{MDA8}$) for each station using hourly data. $[O_3]_{MDA8}$ is used for most of our analysis.

Because a meteorological system is usually on a synoptic scale (~1000 km), chapter 2 will study the regional-scale ozone feature rather than ozone concentrations at each individual station. So we average over all the stations within a region (i.e., SE, NE, MW, and CA) to obtain the regional daily $[O_3]_{MDA8}$. Dashed lines in Figure 2.1 show the definitions of these regions. Particularly, the area of the SE, the focus of Chapter 2,

mainly includes the states of Arkansas, Louisiana, Tennessee, Mississippi, Alabama, Georgia, North Carolina, and South Carolina. To explore the long-term features, we also derive the regional monthly mean $[O_3]_{MDA8}$ by taking average of the regional daily $[O_3]_{MDA8}$ within a month. While the analysis will focus on SE, we also compare results from SE with those from NE, MW, and CA to better understand the regional difference.

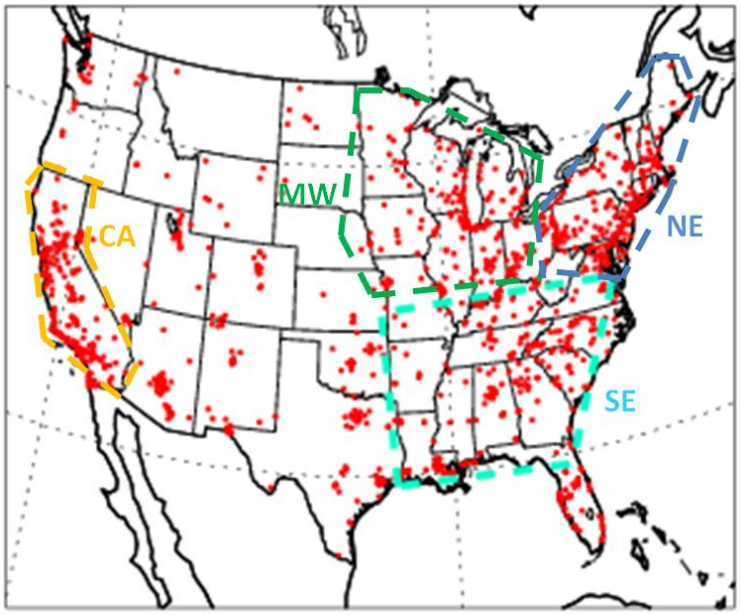

Figure 2.1 Ground-level ozone monitoring stations in the U.S. Areas enclosed in the yellow, green, blue, and cyan dashed lines are defined as CA, NW, NE, and SE, respectively.

2.2.2 EPA Ground-level Isoprene Measurements

We also downloaded the hourly ground-level isoprene measurements from the EPA Data Mar. Among a few sites that have regular long-term measurements, the Yorkville, Georgia site (33.9285 N, 85.04534 W) locates in a rural area surrounded by forests and agricultural lands and is away from significant anthropogenic sources. The records last from 1998 to 2013. Daily canister samples are measured about every week

using gas chromatography with the flame ionization detector (GC-FID). The reported detection limit is 0.1 ppbvC for isoprene.

2.2.3 Long-term Meteorological Reanalysis Data

We use National Centers for Environmental Prediction (NCEP) Climate Forecast System Reanalysis (CFSR) data [*Saha et al*., 2010] to study meteorological patterns associated with ozone events. The original data are in hourly resolution and meteorological parameters include temperature, relative humidity, surface pressure, geopotential height at 850 mbar, wind direction, and wind speed. To obtain daily measures relevant to ozone production, we derived daily maximum temperature (T_{max}) and daytime-averaged relative humidity (RH), wind speed, and other parameters. For wind direction, hourly wind data were first decomposed into u and v, which were then averaged over the daytime; then, a representative wind direction was calculated from daytime-averaged u and v. For comparison with phytological studies, we computed daytime-averaged vapor pressure deficit (VPD, defined as the difference between saturation vapor pressure and ambient vapor pressure) from temperature and relative humidity data. Like ground-level ozone, we derived regional daily and regional monthly-mean series for these meteorological parameters to investigate the regional features on both daily and monthly scales.

2.2.4 Satellite Formaldehyde Observations

We use satellite formaldehyde column density data measured by GOME-2 onboard METOP-A for model comparison (http://h2co.aeronomie.be/) [*De Smedt et al.*, 2012]. The overpass time for GOME-2 is around 10:00 in the morning. Model results at

the overpass time are sampled. For the detailed retrieval algorithm, readers are referred to *De Smedt et al.* [2012].

2.2.5 3-D REAM Simulation

We use the 3-D REAM to simulate ground-level ozone. As introduced in Section 1.2.1, the model has a horizontal resolution of 36 km and 30 vertical layers in the troposphere, driven by the Weather Research and Forecasting (WRF) model assimilated meteorological fields constrained by the CFSR data. The chemistry mechanism is adopted from GEOS-Chem v9-02, with expansion on aromatics chemistry. The anthropogenic emissions are from the emission inventory from HTAPv2 for 2010. The biogenic isoprene emissions are calculated with the MEGAN v2.1 algorithm [*Guenther et al.*, 2006]. The leaf area index that fed into the MEGAN module was from the MODIS product MOD15A2. Cloud fraction and cloud optical depth is parameterized using the scheme described by *Geleyn* [1981]. To compare with observed $[O_3]_{MDA8}$ simulated $[O_3]_{MDA8}$ is computed with hourly output from the simulation.

To evaluate the model performance in varied conditions, we conducted the base simulations for three Octobers with significantly different ozone levels in the SE. They are October 2008 (normal), October 2009 (extremely low), and October 2010 (extremely high). While the model performs well for the normal and low cases, it significantly underestimates the high episodes in October 2010 (Figure 2.4).

To explore the mechanism driving the ground-level high-ozone extremes over the SE during October 2010, we conducted a series of simulations by perturbing the base simulation. To evaluate the contributions of biogenic isoprene emissions, we run the model with zero or doubled isoprene emissions. To characterize the impact of

temperature on the chemistry, we increase the BL temperature in the chemistry module by 1K or 2K. In another two simulations, we increase the BL temperature in both the chemistry and biogenic emission modules by 1K or 2K. To evaluate the humidity impact on chemistry, we also perturb the BL RH by +10% and -10%.We also design a simulation with no cloud cover and no biomass burning emissions to estimate the uncertainties brought by the cloud over parameterization and biomass burning, respectively.

We simulate July 2010 to assess the seasonal difference between the summer and the fall. We also apply emission perturbation for anthropogenic NO_x and biogenic isoprene to the both July 2010 and October 2010 base simulation, to calculate the sensitivity of $[O_3]_{MDA8}$ to anthropogenic NO_x reduction and climate-driven biogenic increase in the summer and the fall.

2.2.6 Explained Variance Decomposition (EVD) method

We use the explained variance decomposition (EVD) method to attribute the contribution of correlated meteorological variables to the ground-level ozone. Note that unlike in other sections, the variables used in this section are normalized for simplicity of mathematical derivation.

Given normalized $[O_3]_{MDA8}$, T_{max}, and VPD, let EV be the coefficient of determination (R^2) for a bivariate linear regression model $[O_3]_{MDA8} \sim T_{max} + VPD$. EV represents the fraction of total variance in $[O_3]_{MDA8}$ that can be explained by T_{max} and VPD. The EVD method described here attempts to decompose $EV_{T\text{-}VPD}$ into three parts: a) Variance solely explained by T_{max}, denoted as EV_T; b) Variance solely explained by

VPD, denoted as EV_{VPD}; and c) Variance explained by the correlation between T_{max} and VPD, denoted as $EV_{T\text{-}VPD}$.

$$EV = EV_T + EV_{VPD} + EV_{T\text{-}VPD} \quad \ldots(1)$$

In the first step to compute EV_T , EV_{VPD}, and $EV_{T\text{-}VPD}$ from the normalized data, do the following transformation:

$$z_1 = T_{max} \quad \ldots(2)$$

$$z_2 = [-\frac{r}{\sqrt{1+r^2}}, \frac{1}{\sqrt{1+r^2}}][\begin{matrix} T_{max} \\ VPD \end{matrix}]$$

where r is the Pearson correlation coefficient between T_{max} and VPD. Note that z_1 and z_2 are orthogonal. A bivariate linear regression ($[O_3]_{MDA8} \sim z_1+z_2$) leads to $[O_3]_{MDA8} = a \cdot z_1 + b \cdot z_2$, where a and b are coefficients for z_1 and z_2, respectively. Since z_1 and z_2 contain the same amount of information as T_{max} and VPD do, R^2 for this model is also EV. Furthermore, since z_1 and z_2 are orthogonal, EV can be decomposed into two parts:

$$EV = a^2 \sum_i z_{1,i}^2 + b^2 \sum_i z_{2,i}^2 \quad \ldots (3)$$

The transformation in (2) also leads to

$$EV_T + EV_{T-VPD} = a^2 \sum_i z_{1,i}^2 \quad \ldots (4)$$

$$EV_{VPD} = b^2 \sum_i z_{2,i}^2 \quad \ldots (5)$$

Similarly to (2), we can also do the following transformation and regression:

$z_3 = VPD$

$$z_4 = [-\frac{r}{\sqrt{1+r^2}}, \frac{1}{\sqrt{1+r^2}}][\begin{matrix} VPD \\ T_{max} \end{matrix}] \quad \ldots(6)$$

$[O_3]_{MDA8} = c \cdot z_3 + d \cdot z_4$

We then have another decomposition of EV

$$EV = c^2 \sum_i z_{3,i}^2 + d^2 \sum_i z_{4,i}^2 \quad \ldots (7)$$

$$EV_{VPD} + EV_{T-VPD} = c^2 \sum_i z_{3,i}^2 \quad \ldots (8)$$

$$EV_T = d^2 \sum_i z_{4,i}^2 \quad \ldots (9)$$

Combining (4), (5), (8), (9), we can solve for EV_T , EV_{VPD}, and $EV_{T\text{-}VPD}$.

2.3 Results and Discussion

2.3.1 High-ozone Extremes over the Southeast in October

Figure 2.2 shows the surface observations of monthly mean maximum daily 8-hour average ozone concentration ($[O_3]_{MDA8}$) in October 2010. The high regional $[O_3]_{MDA8}$ concentrations over the SE (enclosed in the grey line in Figure 2.2) are higher than all other regions of the U.S. except a small area in the southern California. 133 exceedances with daily $[O_3]_{MDA8}$ values greater than 75 ppbv occurred at 66 sites in the SE (Figure 2.3a). The numbers increase to 324 exceedances at 112 sites if the new ambient ozone standard threshold value by the EPA, 70 ppbv, is used.

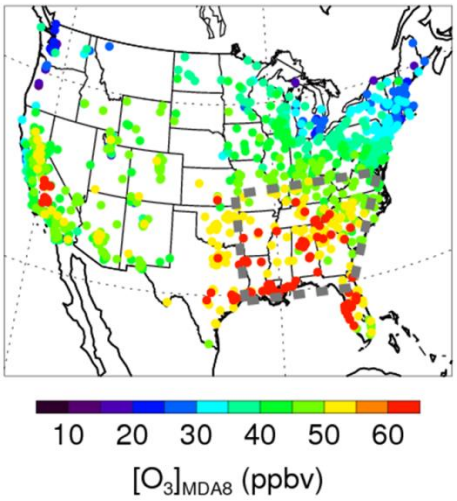

Figure 2.2 The high monthly-mean $[O_3]_{MDA8}$ observed in October 2010 over the SE U.S.

Figure 2.3 puts the 2010 observations in the context of regional monthly mean $[O_3]_{MDA8}$ in October over the SE in the past three decades. The 30-year climatology mean of $[O_3]_{MDA8}$ is ~40 ppbv, considerably lower than that in the summer ozone season (~ 50 ppbv in July). However, in the two extreme years, 2000 and 2010, $[O_3]_{MDA8}$ are 52 and 49 ppbv, respectively, two inter-annual standard deviations higher than the climatological mean. These two extreme years also stand out with high counts of exceedances ($[O_3]_{MDA8}$ >75 ppbv) in the region. There is clearly no obvious ozone trend in October in the last 3 decades, in contrast to the significant decrease of $[O_3]_{MDA8}$ in the summer since 1980s (Figure 1.2b), suggesting that either ozone concentrations are insensitive to the large emission decreases (*EPA*, 2015) in the past three decades or the emission reduction benefit is diminished by regional climate change.

2.3.2 Humidity: a Good Predictor of Ground-level Ozone over the Southeast during October

Observation-based statistical analysis showed that surface ozone is affected by a number of meteorological factors, including temperature, humidity, pressure, wind speed, and wind direction [*Camalier et al.*, 2007; *Vukovich and Sherwell*, 2003]. Correlations between surface ozone and these meteorological parameters vary with region and season, but temperature is usually found to best correlate with ozone [*Fu et al.*, 2015; Rasmussen et al., 2012]. In October over the SE, using the monthly mean data from 1980-2010, we find that the correlation of $[O_3]_{MDA8}$ with daily maximum temperature (T_{max}, R^2=0.24) is much lower than with two humidity measures, relative humidity (RH, R^2=0.71) and vapor pressure deficit (VPD, R^2=0.67) (Figure 2.3b, 2.3c). We use VPD in this study since it is directly related to water stress of plants [*Pegoraro et al.*, 2007]. Using daily

data, the correlation of $[O_3]_{MDA8}$ with VPD (R^2=0.68) is also much higher than with T_{max} (R^2=0.32) (Figure 2.3d, 2.3e).

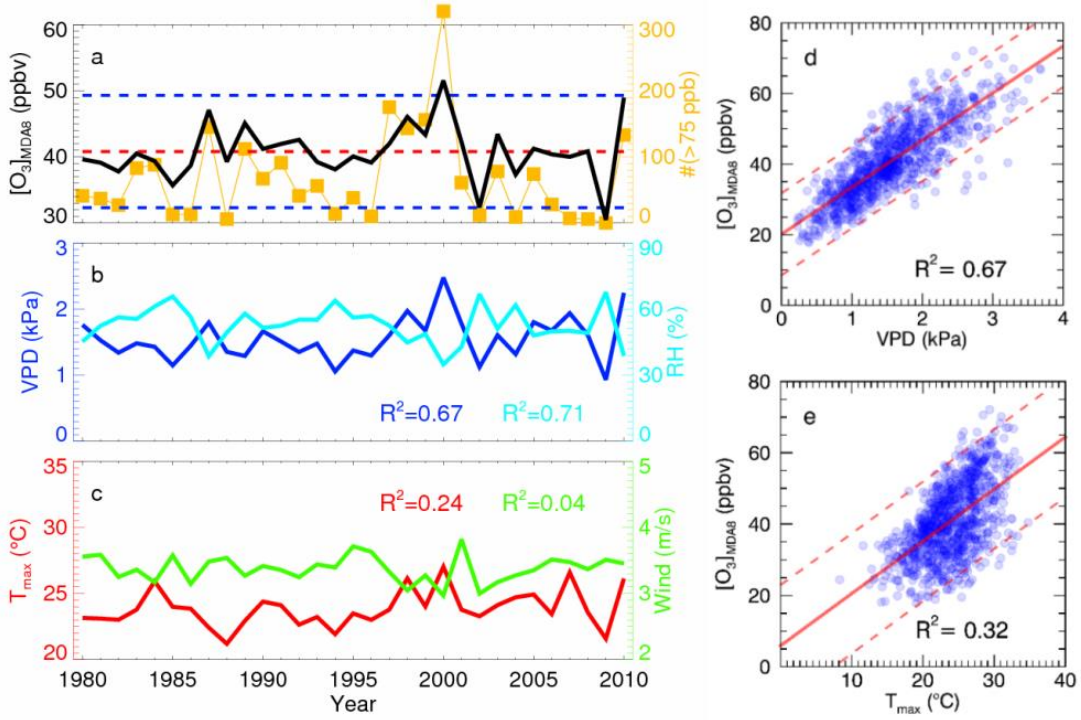

Figure 2.3 Observed ground-level $[O_3]_{MDA8}$ and its relationship with meteorology over the SE in October from 1980 to 2010. a, Regional-averaged monthly mean $[O_3]_{MDA8}$ (black solid) has no significant trend, with a climatology mean ~ 40 ppbv (red dash). In the years 2000 and 2010, $[O_3]_{MDA8}$ reached 2σ (blue dash) above the climatology mean. These two years also feature high violation counts (yellow squares). b and d, $[O_3]_{MDA8}$ is well correlated with two humidity measures, VPD and RH. c and e, $[O_3]_{MDA8}$ is correlated moderately with T_{max}, but poorly with wind speed. Red solid lines in d and e are linear fits and red dash lines the confidence intervals. a-c show monthly mean data and d-e show daily data.

The interpretation of simple linear correlation analysis is often complicated by the colinearity between meteorological factors resulting in part from the synoptic-scale weather [*Camalier et al.*, 2007]. We use the explained variance decomposition (EVD) method (see Section 2.2.6 for method description) to analyze the variance contributions

of T_{max}, and VPD to daily $[O_3]_{MDA8}$ in four regions, SE, Northeast (NE), Midwest (MW), and California (CA) during 1980-2010. We compare the explained variance (EV) of daily $[O_3]_{MDA8}$ attributable solely by T_{max} (EV_T) or VPD (EV_{VPD}) and that to the correlation between T_{max} and VPD ($EV_{T\text{-}VPD}$) in July and October (Table 2.1). In most cases, almost all EV is due to the correlated contribution by T_{max} and VPD. The exception is the October case of SE, where 68% of the variance in $[O_3]_{MDA8}$ can be explained by the two meteorological variables and more than half of the contribution is solely from VPD.

The analysis above implicates that humidity-related mechanisms are governing the ground-level ozone concentrations over the SE during the fall.

Table 2.1 EVD analysis results for the explained variance of $[O_3]_{MDA8}$ by T_{max} and VPD over varied regions in the US in July and October.

	July				October			
	CA	**NE**	**MW**	**SE**	**CA**	**NE**	**MW**	**SE**
$\mathbf{EV_{T\text{-}VD}}$	0.46	0.40	0.39	0.42	0.50	0.45	0.58	0.32
$\mathbf{EV_T}$	0.00	0.14	0.05	0.00	0.00	0.08	0.04	0.00
$\mathbf{EV_{VD}}$	0.05	0.00	0.01	0.07	0.04	0.11	0.11	0.36
EV	0.51	0.54	0.45	0.49	0.54	0.64	0.73	0.68

2.3.3 Simulations Underestimates Ground-level Ozone during Episodes

To investigate the physical mechanism for the correlated increase of VPD and surface ozone, we examine in detail the extreme monthly $[O_3]_{MDA8}$ in October 2010, when the ozone enhancement is regional in nature (Figure 2.2) and the SE regional mean ~ 10 ppbv higher than the climatological value (Figure 2.3a). The ozone enhancement in the monthly mean is mainly due to three episodes, October 7-12, 16-18, and 21-24, with concurrent high temperature and VPD (Figure 2.3b, 2.3c).

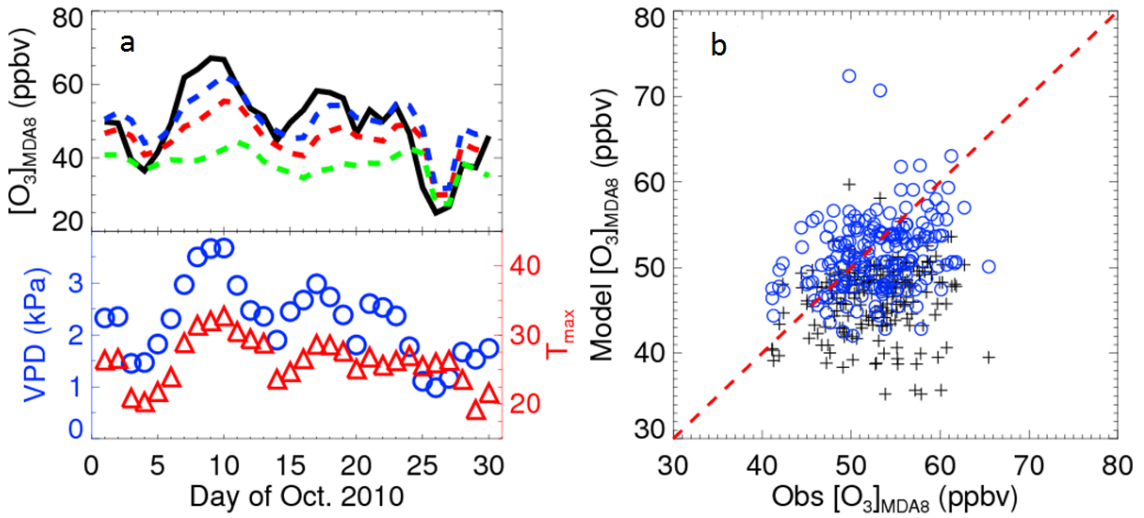

Figure 2.4 Model simulation of regional mean $[O_3]_{MDA8}$ in the SE during October 2010. a, Comparing with the observed regional-mean $[O_3]_{MDA8}$ (black solid), the base simulation (red dash) underestimates by ~ 15 ppbv during the episodes. The bias is greatly reduced in the simulation with doubled biogenic isoprene emissions (blue dash). The simulation without biogenic isoprene emissions (green dash) gives a reference for the importance of biogenic emission during the month. The two episodes are concurrent with high VPD (i.e., dry conditions, blue circles) and high temperature (red triangles). b, The simulation with doubled isoprene emissions (blue circles) is in better agreement with observations than the base simulation (black cross). Every symbol represents a station within the grey dash line in a. The red line is the 1:1 line.

Figure 2.4a and 2.4b show that the base simulation underestimate $[O_3]_{MDA8}$ by ~ 15 ppbv during the three episodes in October 2010. In comparison, the sharp decrease towards the end of the month around October 26, due to an intensive extra-tropical cyclone, is well simulated by the model. The coupling between weather condition and surface ozone is clearly shown in the figure. During the period of warm and dry weather (i.e., high VPD values), ozone concentrations tend to be higher because a lower wind

speed reduces ventilation of high ozone air mass by advection and less cloud (and no precipitation) increases photochemical production.

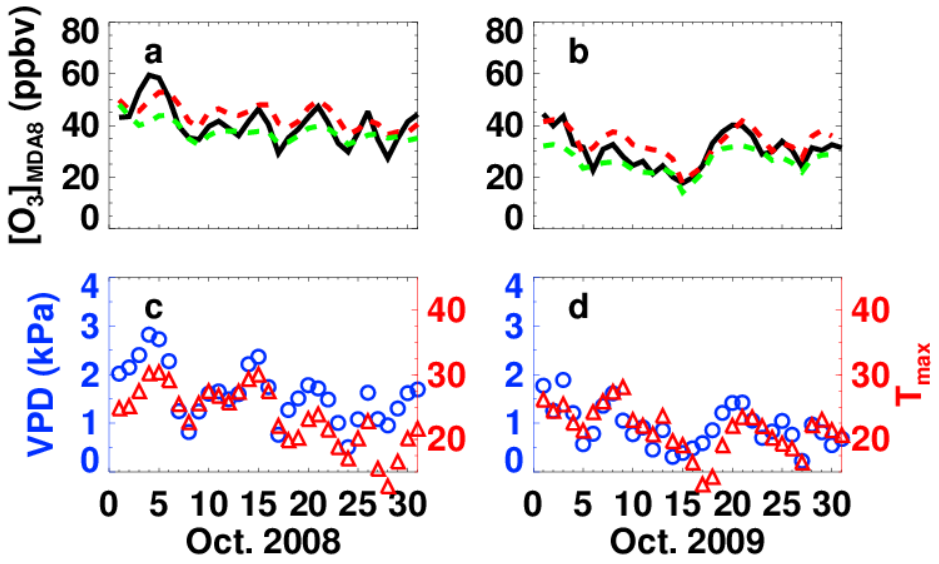

Figure 2.5 Simulated $[O_3]_{MDA8}$ in a low-ozone month, Oct. 2009, and a normal-ozone month, Oct. 2008 over the SE. a and b, Black solid lines are observations, red dashed lines are the base simulation, and green dashed lines are simulations with no isoprene emissions. c and d, Blue symbols are VPD and red symbols T_{max}.

The coupling of weather and surface ozone is also a function of emissions. Figure 2.4a shows that the ozone enhancement during the episodes is much larger in the base simulation than a sensitivity simulation without biogenic isoprene emissions, reflecting the sensitivity of ozone production to VOC emissions in October [*Jacob et al.*, 1995]. Thus, the ozone underestimations during dry and warm weather conditions may reflect errors in anthropogenic or natural emissions. We consider further that the model simulations do not have large biases when VPD values are low in October 2010 and that the model can simulate well ozone observations in the October of the low-ozone year of 2009 or the average-ozone of 2008 (Figure 2.5) when VPD values are lower than 2010.

These results indicate that anthropogenic emissions, which do not vary much with weather, are reasonably estimated in the model. On the other hand, natural emissions of isoprene, the most significant VOC precursor for ozone in eastern U.S., are heavily affected by weather conditions. Indeed, the model biases of surface ozone in the warm and dry episodes in October 2010 are largely corrected in the sensitivity simulation with model estimated isoprene emissions being doubled (Figure 2.4).

2.3.4 Humidity-driven Biosphere Feedback

The fact that the model underestimation does not occur in simulations of low-ozone (e.g., October 2009) or average-ozone (e.g., October 2008) Octobers (Figure 2.5) indicates caveats of model representation in high-ozone events. We conduct a series of sensitivity simulations (Section 2.2.5) to examine the drivers that are potentially responsible for the underestimation. One of these simulations shows that we can greatly reduce the bias during the episodes if we double the biogenic isoprene emissions (Figure 2.4 and Figure 2.6).

In addition to a reduction of bias in ground-level ozone, the increase in isoprene emissions also brings the simulated column density of formaldehyde (CH_2O), a high-yield product from isoprene chemistry often used for validating the isoprene emission inventory [*Palmer et al.*, 2003; *Palmer et al.*, 2006; *Millet et al.*, 2006; *Fu et al.*, 2007], to a better agreement with GOME-2 satellite observations (Figure 2.7). Note that the CH_2O column in the base simulation agrees with GOME-2 observations in Octobers of 2008 and 2009. These results suggest that the model may have underestimated the response of isoprene emissions to the meteorological conditions of both high temperature and low humidity (Figure 2.4).

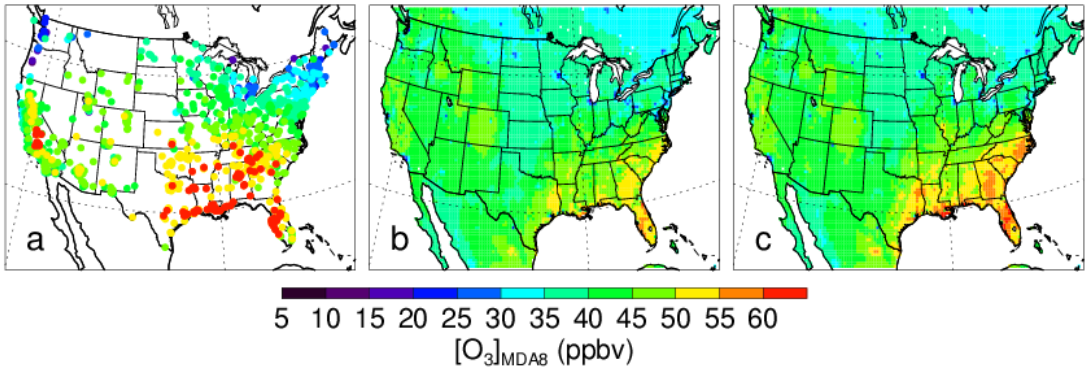

Figure 2.6 The comparison between observed and simulated monthly mean $[O_3]_{MDA8}$ in October 2010. a, observations b, the base simulation; c, the simulation with doubled isoprene emissions.

It is worthwhile to notice that compared with the intensive isoprene emissions in the summer over the SE, the doubled isoprene emissions (~20-30 mg/m^2/day) are still relatively small. However, because of the shift of chemistry regime from NO_x-sensitive in the summer to VOC-sensitive in the fall [*Jacob et al.*, 1995], the ozone production becomes quite sensitive to isoprene in October (Figure 2.8). The significant contribution of isoprene to the ozone episodes, shown as the difference between the no-isoprene simulation and the doubled-isoprene simulation (Figure 2.4) in the October 2010 case, also underscores the importance of accurately modeling biogenic isoprene emissions in the fall, which has been paid inadequate attention in the community.

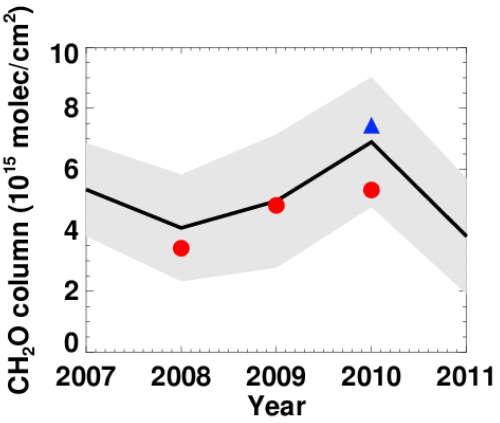

Figure 2.7 GOME-2 observed CH_2O column density (black) over Southeast US during October from 2007 to 2011 features a peak in 2010, suggesting strong biogenic emissions. The simulated CH_2O column density with standard MEGAN algorithm (red) is in agreement with satellite in 2008 and 2009, but has underestimation in 2010. Doubling biogenic emissions (blue) in 2010 reduces the bias.

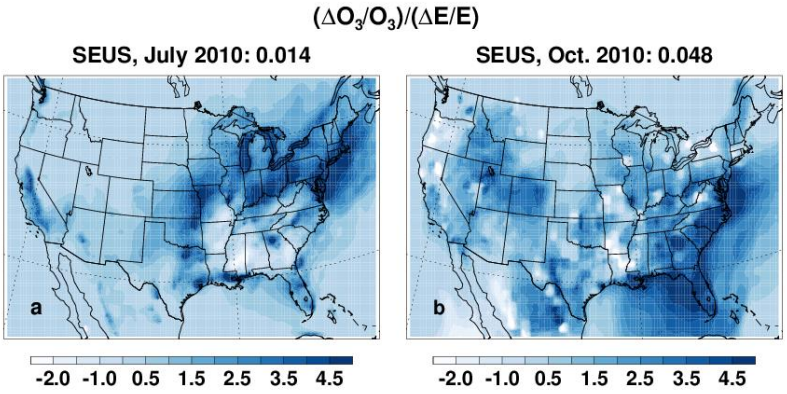

Figure 2.8 The relative sensitivity of daytime ozone to the change of isoprene emissions is larger in October, 2010 (SE average 0.048) than in July, 2010 (SE average 0.014) over the SEUS, demonstrating that the ozone production is more sensitive to biogenic VOC emissions in the fall because of the chemical regime shift.

The 3-D REAM model uses the MEGAN, a state-of-the-art biogenic emission module, to calculate biogenic isoprene emissions. The MEGAN algorithm takes into account environmental variables such as temperature, radiation, and soil moisture but includes no humidity-emission relationship [*Guenther et al.*, 2006]. However, an examination of long-term isoprene measurements at Yorkville, GA, a forested site representative in the SE [*Xu et al.*, 2015], during October from 1998 to 2013, suggests that the humidity-emission relationship may be more important than the well-known temperature-emission relationship in October. Because the inference of ambient isoprene concentration to the emissions is confounded by OH concentrations and boundary layer mixing, we compare empirical cumulative distribution functions (ECDF) of isoprene concentrations under different humidity or temperature conditions. The ECDFs show that high concentrations of isoprene occurs much more frequently in the low humidity case (VPD>2 kPa) than in the high humidity case (VPD<2 kPa) (Figure 2.9) suggesting that low humidity stimulate isoprene emissions. In contrast, no significant difference in ECDFs is found between high temperature (T_{max}>30^{o}C) and low temperature (T_{max}<30 ^{o}C) cases, implying that dependence of isoprene emissions on temperature is weaker than that on humidity in October.

The enhancement of isoprene emissions in a low-humidity episode is noticed in a few laboratory studies [*Pegoraro et al.*, 2005; *Pegoraro et al.*, 2007]. For example, a study conducted in Biosphere 2, by controlling multiple factors, including air temperature, radiation, carbon dioxide concentration, soil moisture, and water vapor, demonstrated that the gross isoprene production from cottonwood trees could enhance by a factor of two when VPD increased from 1 kPa to 3 kPa (RH decreased from ~80% to

~40% under the experiment condition. See Figure 2.10). The doubling of isoprene emissions under the conditions of the October 2010 episodes is consistent with this laboratory study. It is also interesting to notice that the relationship between humidity and emissions observed in the field is rather contradictory [*Geron et al.*, 1997; *Pier*, 1995; *Potosnak et al.*, 2014]. However, most of these studies are subject to confounding factors such as soil moisture and are conducted in the main growing season instead of the fall.

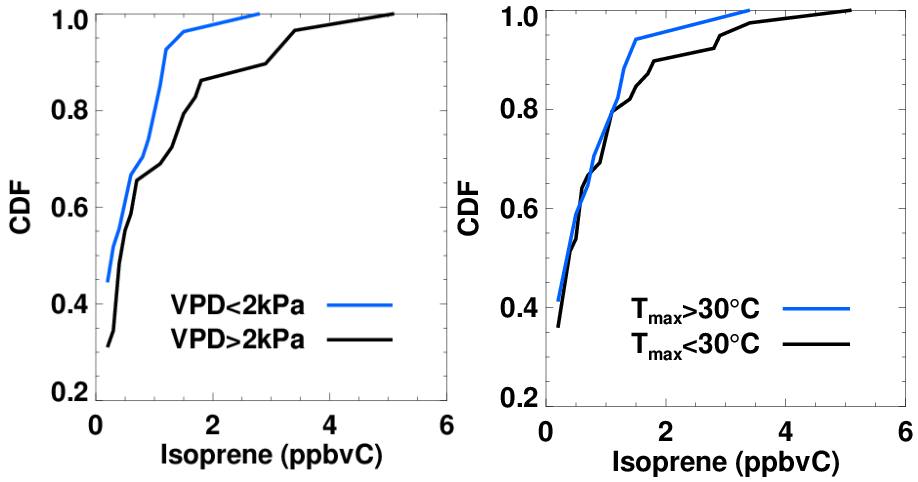

Figure 2.9 Comparisons of ECDFs under varied conditions of VPD and T_{max}. (Left) Comparisons of ECDFs of isoprene measurements indicate that high isoprene concentrations are more likely to occur when VPD is greater than 2kPa. (Right) Comparisons of ECDFs do not find a higher probability of high isoprene concentrations for T_{max} greater than 30 ℃.

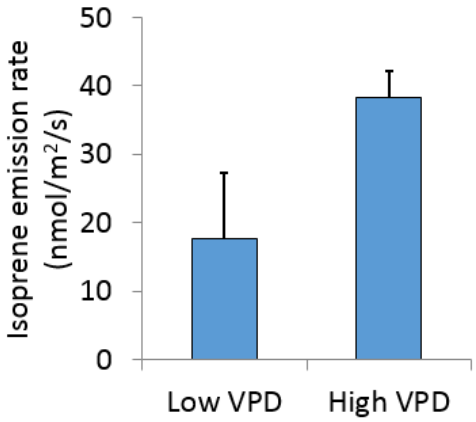

Figure 2.10 The experiment conducted in Biosphere 2 by *Pegoraro et al.* [2007] shows that isoprene emission rate enhances by a factor of two from low VPD (humid, ~ 1 kPa) condition to high VPD (dry, ~3 kPa) condition.

2.3.5 Exploration of Other Known Mechanisms

To explore alternative explanations (Section 2.2.5) for the underestimation of ozone during the episodes, we also evaluate the sensitivities of multiple ozone-impacting factors, including temperature, water contents, and cloud cover. Our simulations find that an increase of temperature by 2 K results in an increase of $[O_3]_{MDA8}$ by less than 3 ppbv, mainly because of increased biogenic isoprene emissions (Figure 2.11). The simulations also show that perturbation of RH by 10% (without biogenic emission feedback) leads to change of $[O_3]_{MDA8}$ by less than 0.5 ppbv and that the effect is of variable signs, demonstrating that the direct impact of water content on ozone chemistry is small (Figure 2.11). To rule out the possibility that underestimation of ozone is caused by overestimation of cloud cover, we conduct a simulation with zero cloud cover, which only negligibly increase $[O_3]_{MDA8}$ from the base simulation. Biomass burning, which

emits ozone precursors, can be more intensive during a drought. But examination of the Global Fire Emission Database (GFED) burning area shows that October 2010 is not an extraordinary month of biomass burning over the region (Figure 2.12). Regional mean $[O_3]_{MDA8}$ changes only negligibly in a simulation taken out the biomass burning emissions, indicating that the contribution of biomass burning to ozone is likely to be insignificant on a regional scale. These results from sensitivity simulations show that the modeling uncertainties of temperature, water contents, cloud cover, and biomass burning are unlikely to explain the ~ 15 ppbv underestimation of $[O_3]_{MDA8}$ during the episodes.

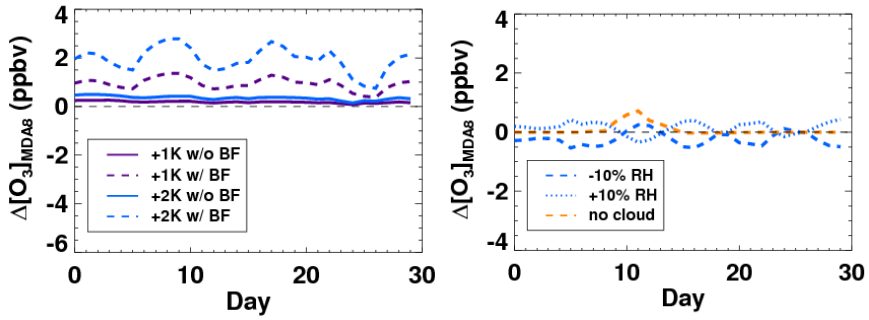

Figure 2.11 The response of surface ozone ($[O_3]_{MDA8}$) to perturbation of temperature with or without biogenic emission feedback (left), relative humidity, and cloud (right) shows that the uncertainties in these factor are inadequate to explain the underestimation of $[O_3]_{MDA8}$ during the episodes of October 2010.

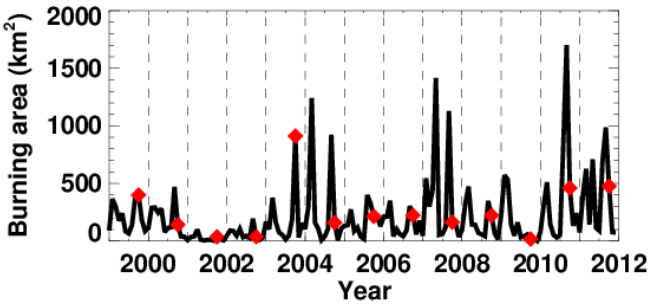

Figure 2.12 The GFED biomass burning area over the SE from 1999 to 2011 (black line) and data for Octobers of each year (red dot).

2.4 Summary and Implications

Previous studies have raised concerns that climate change drives the extension of the ozone season into the fall [*Avise et al.*, 2009; *Chen et al.*, 2009]. Current discussions on the ozone climate penalty (the response of ground-level ozone to climate change) mainly focus on the ozone-temperature relationship [e.g., *Jacob and Winner*, 2009; *Rasmussen et al.*, 2012; *Wu et al.*, 2008]. However, our study finds ozone-humidity effect being a more important relationship regionally in October. Despite the great spread among members, the ensemble mean of a group of the state-of-art climate models (e.g., GFDL, CESM, and GISS) does show a decreasing trend of humidity over the SE region (Figure 2.13). Some model members (i.e., GFDL) even project a decreasing trend in the lower percentiles of relative humidity in the next 50 years, suggesting that it is probable that dry October similar to 2000 and 2010 will occur more frequently (Figure 2.13). Note that the VPD values in Figure 2.13 are significantly smaller than those in Figure 2.3 and 2.4. That is because climate models use VPD for all 24 hours, but our analysis uses only daytime values. These results suggest that a drier SE is likely in the future; therefore, the humidity-regulated biogenic emission feedback proposed in this work may be a key factor for the extension of the ozone season. In addition, it is also expected that increased biogenic emissions in the SE will also lead to an increase of secondary organic aerosols, an air pollutant and a mediator in the climate feedback.

Despite the regional projection of humidity is still subject to great uncertainty, our work highlights the complexity of biosphere-chemistry-climate interactions. Predictions of future ozone changes outside the conventional ozone season require more accurate representation of biogenic emissions, especially the possible linkage between humidity

and isoprene emissions, which warrants further study. We suggest that the humidity effect be included in the evaluation of the future air quality control strategy in addition to the temperature penalty.

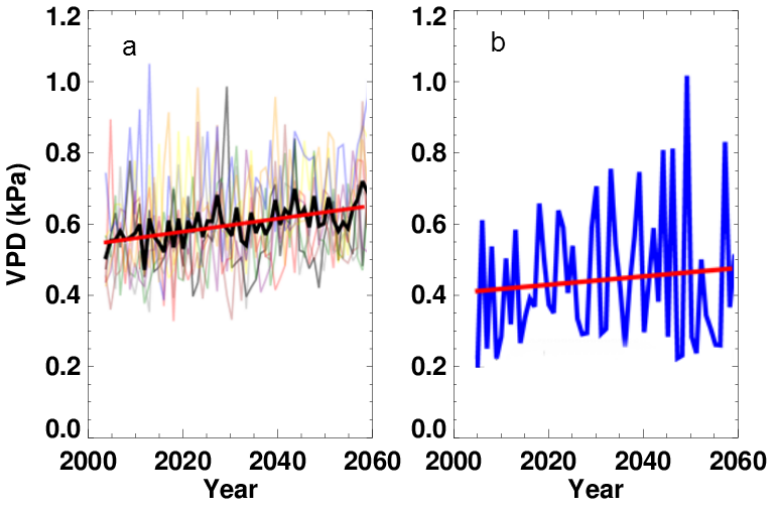

Figure 2.13 Projections of VPD by climate models over the SE in next 50 years. a, Ensemble means from the GISS model (RCP 4.5) show increasing trend of VPD in the SE in the next 50 years; b, One GFDL model member with RCP 4.5 emissions predicts that high VPD events may become more extreme in the future.

CHAPTER 3

[2]LARGE VERTICAL GRADIENT OF REACTIVE NITROGEN OXIDES IN THE BOUNDARY LAYER

3.1 Introduction

The vertical distribution of air pollutants in the boundary layer (BL) is a complex function of emissions, advection, chemistry, and turbulent mixing. In homogeneously polluted areas (e.g., Washington-Baltimore region. See Figure 3.1) with relatively strong surface emissions, the vertical distribution of a pollutant is largely dependent on the competition between chemistry and turbulent mixing. Based on the reasoning that vigorous turbulent mixing in the BL is much faster than chemical loss for many species of interest, air pollution studies often assume a well-mixed BL. This assumption enables researchers to extrapolate surface observations into the entire BL [e.g., *Petritoli et al.*, 2004; *Fiedler et al.*, 2005; *Leigh et al.*, 2007; *Lee-Taylor et al.*, 2011; *de Arellano et al.*, 2011; *Knepp et al.*, 2013] and thus greatly extends the use of surface measurements. This assumption readily works as a first-order approximation for long-lived species such as carbon monoxide and ethane but is invalid for very reactive species such as isoprene.

---

[2] This chapter is an extension of "Large Vertical Gradient of Reactive Nitrogen Oxides in the Boundary Layer: Modeling Analysis of DISCOVER-AQ 2011 Observations", submitted to Journal of Geophysical Research – Atmospheres. Coauthors are Yuhang Wang, Gao Chen, Charles Smeltzer, James Crawford, Jennifer Olson, James Szykman, Andrew J. Weinheimer, David J. Knapp, Denise D. Montzka, Armin Wisthaler, Tomas Mikoviny, Alan Fried, Glenn Diskin.

However, for moderately reactive species which has a chemical life time comparable to the BL mixing time scale, the validity of the well-mixed BL assumption over emission regions is determined by the competition between chemistry and mixing and has not been thoroughly evaluated.

In this chapter, we will focus on one such species, nitrogen oxides (NO_x=NO_2+NO), a primary pollutant that plays a critical role in the formation of tropospheric ozone [*Liu et al.*, 1992; *Chameides et al.*, 1992], nitrate aerosol [*Bassett and Seinfeld*, 1983], and secondary organic aerosol [*Ng et al.*, 2007]. We will use aircraft measurements from a NASA Earth Venture campaign in July 2011, DISCOVER-AQ 2011, to investigate the factors regulating the vertical profile of NO_x and evaluate the bias of the BL-average ozone production rate [*Liu et al.*, 2012a] and satellite NO_2 retrieval [*Boersma et al.*, 2004; *Gu et al.*, 2014] calculation resulting from the inadequate knowledge of the vertical distributions.

The remainder of this chapter will proceed as follows. Section 3.2 describes the data and methods used in this study. Section 3.2.1 documents the aircraft measurements from DISCOVER-AQ 2011. To gain insight into how BL conditions impact the vertical profile of NO_x, we classify the observed vertical profiles based on BL height and potential temperature gradient in Section 3.2.2. Section 3.2.3 describes the setup of the 1-D REAM. Section 3.2.4 and Section 3.2.5 describe the calculation of model diagnostics and NO_2 air mass factor, respectively. We present results and discussions in Section 3.3. In Section 3.3.1, we present modeling results and comparisons with observations based on the profile classification presented in Section 3.2.2. We then explore the sensitivity of the NO_x vertical profile to BL stability in Section 3.3.2. To characterize the uncertainty in the modeling analysis, we analyze in Section 3.3.3 the impact of BL and land-surface parameterizations on the vertical profiles of NO_x. In Sections 3.3.4 and 3.3.5, we quantitatively assess the influence of the BL NO_x gradient on the calculation of the BL-

averaged ozone production rate and tropospheric NO_2 column retrieval, respectively. Finally, in Section 3.4, we summarize our findings.

3.2 Data and Methods

3.2.1 DISCOVER-AQ Aircraft Measurements

Deriving Information on Surface Conditions from Column and Vertically Resolved Observations Relevant to Air Quality (DISCOVER-AQ 2011) is a NASA Earth Venture campaign taken over the Washington-Baltimore region in July 2011. DISCOVER-AQ is unique in that the aircraft systematically sampled the BL and to obtain a large dataset of vertical profiles of trace gases and aerosols. During DISCOVER-AQ 2011, 14 research flights using the NASA P-3-B aircraft took place around the Washington-Baltimore region. By performing spiral profiling over six surface sites and occasionally over the Chesapeake Bay (Figure 3.1), extensive measurements were made in the BL and the LFT, providing a total of 253 daytime vertical profiles of various species from ~300 m to 5 km.

NO, NO_2, and ozone were measured by the NCAR 4-channel chemiluminescence instrument [*Brent et al., 2013*]. Formaldehyde was measured by a difference frequency generation absorption spectrometer [*Weibring et al., 2010*]. Volatile organic compounds, including isoprene, toluene, and xylene, were measured using a proton-transfer-reaction mass spectrometer [*Lindinger et al., 1998*]. CO was measured by a diode laser spectrometer [*Sachse et al., 1987*]. Table 3.1 summarizes the measurement methods and data uncertainties in DISCOVER-AQ 2011.

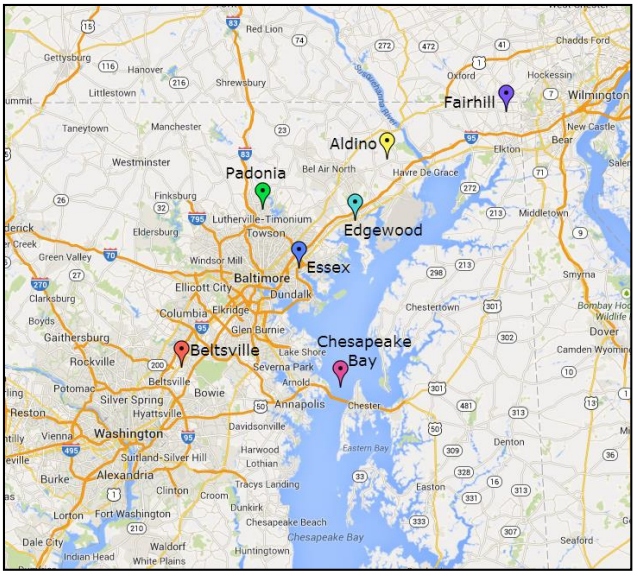

Figure 3.1 The sampling region of DISCOVER-AQ 2011. The colored symbols denote the surface sites above which extensive aircraft sampling in a spiral manner were made.

Table 3.1 The measurement methods and data uncertainties in DISCOVER-AQ 2011

Species	Method	Frequency	Typical Uncertainty
NO	4-channel chemiluminescence instrument	1 Hz	10%
NO_2			15%
O_3			5%
CH_2O	Difference frequency generation absorption spectrometer	1 Hz	4%
CO	Diode laser spectrometer	1 Hz	2% or 2ppbv
Toluene	Proton transfer reaction mass spectrometer	0.07 Hz	10%
Xylenes			10%
Isoprene			10%
Acetaldehyde			10%
MVK_MAC			10%

3.2.2 Classification of Vertical Profiles

During DISCOVER-AQ 2011, extensive aircraft measurements were made by spiral profiling in the BL and the lower free troposphere, providing a total of 253 daytime vertical profiles of various species including NO and NO_2 from ~300 m to 5 km. To calculate these vertical profiles, raw measurements of each spiral sampling are binned and averaged based on the model vertical levels in part to remove the fine-scale horizontal variation that cannot be simulated in a 1-D model.

To investigate the impact of turbulent mixing on the vertical profile of NO_x, we classify over 200 vertical profiles based on BL height and stability. The BL height is determined as the height where the potential temperature gradient is larger than 5 K/km [*Heffter, 1980*]. We classify a vertical profile as "deep", "medium", or "shallow" if the BL height is higher than 1 km, between 0.5 km and 1 km, or lower than 0.5 km, respectively. To characterize the stability of the BL, we calculate the average linear potential temperature gradient within the BL. We classify a vertical profile as "turbulent", "neutral", or "stable" if the potential temperature gradient is less than 0.1 K/km, between 0.1 K/km and 1 K/km, or greater than 1 K/km, respectively. Note that our definitions of a turbulent, neutral, or stable BL are different from conventional ones, in which an unstable, neutral, or stable BL is usually defined as potential temperature gradient less than, equal to, or greater than 0 K/km, respectively. Our definition is designed to reflect the non-linear scale observed in the relationship between NO_x vertical gradient and BL stability (See discussion in Section 3.3.2).

Table 3.2 shows a summary of profile classification. Because our algorithm cannot identify the BL height for some of the vertical profiles, the total count of classified

profiles is 209. The vertical profiles in DISCOVER-AQ 2011 distribute unevenly among the categories. The dominant category is “deep and neutral” (123 profiles), accounting for more than half of all classified vertical profiles. Following “deep and neutral” are categories “deep and turbulent” (40 profiles), “medium and neutral” (24 profiles), “shallow and stable” (12 profiles), and “medium and stable” (7 profiles). As expected, the two dimensions, BL height and BL stability, overlap to a large extent and no profile falls in the categories “deep and stable”, “medium and turbulent”, “shallow and turbulent”, and “shallow and neutral”. Therefore, we exclude these four categories in our discussion. Because “shallow and stable” and “medium and stable” categories show similar vertical profiles and the profile numbers are relatively low, we also merge these two groups into the category “stable” so as to simplify our discussion.

Table 3.2 Counts of vertical profile categories, classified based on BL height and potential temperature gradient.

Height / Stability	Deep >1km	Medium 0.5-1km	Shallow <0.5km
Turbulent (<0.1K/km)	40	-	-
Neutral (0.1-1K/km)	123	24	-
Stable (>1K/km)	-	7	12

Table 3.3 summarizes the distribution of profile categories among the time of the day and among surface sites. As a result of the sampling design, the classified vertical profiles are more frequent towards midday (10:00-14:00 LT) than late afternoon (14:00-18:00 LT) and early morning (6:00-10:00 LT). On the other hand, the distributions of classified vertical profiles are similar among various sites, except for Chesapeake Bay and Beltsville. The underrepresentation of the Beltsville site is partly due to air traffic

control, which leads to difficulty in identifying the BL height from inadequate vertical sampling. Because of the cooler water surface relative to land at daytime, the BL over the Chesapeake Bay tends to be more shallow and stable. The similar category distributions of NO_x profiles among land sites reflect homogeneity of BL conditions over the region. Table 3.3 also shows that "deep and turbulent" and "deep and neutral" cases are more frequent and "stable" cases are less frequent in midday and late afternoon than in early morning. However, it is noteworthy that we also find a few "deep and turbulent" and "deep and neutral" cases in the morning and a few "stable" cases in the afternoon.

Table 3.3 Distributions of profile categories with respect to local time and location during DISCOVER-AQ 2011.

	Deep &Turbulent	**Deep &Neutral**	**Medium &Neutral**	**Stable**	**Total**
Distribution of profile categories at varied local time					
6:00 -10:00	2	10	8	9	29
10:00 - 14:00	29	75	12	7	123
14:00 - 18:00	9	38	4	3	54
Distribution of profile categories at varied sites					
Padonia	5	24	2	3	34
Fairhill	9	25	5	1	40
Aldino	8	21	5	2	36
Edgewood	7	27	5	2	41
Essex	6	22	3	3	34
Beltsville	5	3	3	4	15
Chesapeake Bay	0	1	1	4	6

3.2.3 1-D REAM Setup

We use the 1-D REAM to analyze the vertical profile of NO_x during DISCOVER-AQ 2011. The 1-D REAM is constrained with measurements from DISCOVER-AQ 2011. We specify surface-emitted species, including NO, NO_2, aromatics, and isoprene, with observations at the lowest altitude of aircraft measurements (~300 m). While the emissions of these species can be estimated in the 1-D model, we did not carry out the analysis due to a lack of reliable observations below 300 m (A.1 in Appendix 1). For the same reason, all the analysis results presented in this work are above 300 m. For the species with relatively long lifetimes such as O_3 and CO (Figure 3.3 (f)), we constrain the model with the measured vertical profiles. The diurnal variations of constrained species (e.g., NO_x at 300 m, O_3) are estimated by aggregating daytime observations when possible. Any measurement data gap is interpolated using 3-D REAM simulation results (e.g., at night). The unmeasured VOCs (e.g., alkanes) are specified at ~300 m with 3-D REAM simulation results. Their effects on O_3 chemistry are not large. All model evaluations are done for the time of the observations. Comparing 1-D REAM results with observations, we find that model is able to reproduce the vertical profile of observed NO_x (Figure 3.2) and other species (Figure 3.3 (a)-(e)). To achieve a quasi-steady state, we run the 1-D REAM with a 1-min time step for 20 simulation days with repeated diurnal meteorological fields in the day of the observation. Only the results from the last day are used for analysis.

To investigate how the parameterizations of the BL and land-surface processes impact the simulation, we test three BL schemes, Asymmetric Convective Model version 2 (ACM2) [*Pleim*, 2007], Yonsei University (YSU) [*Hong et al.*, 2006], and Mellor–

Yamada–Janjic (MYJ) [*Mellor and Yamada*, 1982; *Janjić*, 1990], and two land-surface schemes, Noah and RUC, in the WRF model. For MYJ and YSU, we use a local turbulent diffusion scheme to do the vertical mixing. Although YSU includes non-local terms in its formulation, the local turbulent diffusion scheme is used because of the lack of a consistent treatment for meteorological parameters and chemical tracers [*Pleim*, 2011]. For the hybrid local and non-local scheme ACM2, we implement the vertical transport scheme following *Pleim* [2007]. For comparison purposes, the sensitivity tests of BL schemes use only the Noah land-surface scheme and the sensitivity tests of land-surface schemes use only the MYJ BL scheme. Section 3.3.3 summarizes and compares the performance of these BL and land-surface schemes.

3.2.4 Model Diagnostics

To investigate the factors controlling the vertical profile, we compute chemical lifetime (τ_c) and turbulent mixing time (τ_m) using model results. τ_c varies from species to species and is calculated as $\tau_c = [X]/L_x$, where [X] is modeled concentration of species X and L_x the chemical loss rate of X. On the other side, τ_m is independent of the species in question and is defined as the time that a model layer takes to accumulate the concentration of an inert gas to 1/e of the first layer, given a fixed concentration in the first layer and zero initial concentrations in the rest of model layers. We use a simplified 1-D model with only vertical turbulent transport driven by the WRF generated vertical turbulent diffusivity to calculate τ_m.

Using the simulated concentrations of NO, HO_2, and various peroxy radicals (RO_2), we diagnose the vertical profile of the ozone production rate and derive the BL-

averaged ozone production rate. The ozone production rate for a model layer i, denoted as $P(O_3)_i$, is calculate as

$$P(O_3)_i = k_{0,i}[NO]_i[HO_2]_i + \sum_{j=1}^{n} k_{j,i}[NO]_i[RO_2]_{j,i},$$

where $k_{0,i}$ is the rate constant for the NO+HO_2 reaction, $k_{j,i}$ are rate constants for various NO+RO_2 reactions, and $[NO]_i$, $[HO_2]_i$, $[RO_2]_{j,i}$ are concentrations for NO, HO_2, and various RO_2 radicals in layer i. The BL-averaged ozone production rate, denoted as $P(O_3)_{BL}$, is calculated as the average of the ozone production rate in each layer within the BL weighted with the layer thickness,

$$P(O_3)_{BL} = \frac{\sum_{i=k_{BLB}}^{k_{BLT}} P(O_3)_i \cdot h_i}{h_{BL}},$$

where h_i is the thickness of layer i, k_{BLB} is the lowest model layer with aircraft observations (~ 300 m), k_{BLT} is the model layer that encloses the BL top, and h_{BL} is the thickness of the boundary layer. We also compute the vertical profile of the net ozone production rate ($N(O_3) = P(O3) - L(O3)$) and the BL-averaged net ozone formation rate

$$\mathbf{N(O_3)_{BL}} = \frac{\sum_{\mathbf{i=k_{BLB}}}^{\mathbf{k_{BLT}}} \mathbf{N(O_3)_i \cdot h_i}}{\mathbf{h_{BL}}}.$$

3.2.5 Calculation of the NO_2 Air Mass Factor

The air mass factor (AMF), defined as the ratio of the slant column observed by a satellite to the vertical column to be retrieved, is a key quantity in retrieving the NO_2 tropospheric column. In addition to satellite measurement error, the AMF calculation constitutes an important source of retrieval error [*Boersma et al.*, 2004]. Studies have

shown that using an inaccurate NO_2 a priori profile shape leads to biases in the AMF [*Boersma et al.*, 2004; *Boersma et al.*, 2011].

Based on simulated NO_2 vertical profiles, we calculate the AMF for each individual profiles (AMF_{ind}) and the AMF for site-average and campaign-average vertical profiles (AMF_{avg}). The difference between AMF_{ind} and AMF_{avg} provides information on how the temporal variation in vertical profiles impacts NO_2 column retrievals. To explore the contribution of BL stability to the temporal variability, we calculate the AMF for each profile category. In our calculation, we use the DAK2 radiation scheme provided by the Koninklijk Nederlands Meteorologisch Instituut (KNMI).

3.3 Results and Discussion

3.3.1 NO_x Vertical Profiles

Figure 3.2(a) shows good agreement between the observed and simulated vertical profile of NO_x. Note that the aircraft sampling during DISCOVER-AQ 2011 was usually conducted in daytime with no significant cloud cover reported. Therefore, a well-developed BL is expected. In fact, the average BL height during aircraft sampling is 1.4 km. However, to the contrary of what a well-mixed BL would suggest, both the observations and model simulations show a substantial vertical gradient of NO_x. The median concentration of NO_x decreases from 1.5 ppbv at ~300 m to 0.4 ppbv at the average BL height (1.4 km), a 70% concentration decrease in 1 km. A closer examination of individual NO_x vertical profile affirms the prevailing negative gradient of NO_x in the BL during the campaign. The magnitude of the gradient, however, varies greatly from profile to profile (Figure 3.4 (a)).

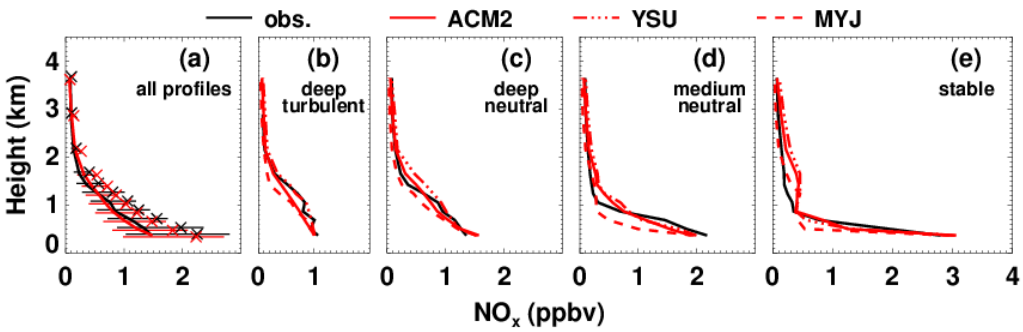

Figure 3.2 (a) Observed (black) and simulated (red) median vertical profiles of NO_x during DISCOVER-AQ 2011. Error bars indicate the interquartile ranges and crosses show the arithmetic means. (b)-(e) Observed (black) and modeled (red) median vertical profile of NOx for varied profile categories: (b) "deep and turbulent", (c) "deep and neutral", (d) "medium and neutral", and (e) "stable". Red lines show simulated results using ACM2 (solid), YSU (dash-dotted), and MYJ (dashed).

Research-quality ground-level NO_2 measurements are only available at two sites, Edgewood and Padonia. Therefore, analysis of vertical gradient in the lowest 300 m is not included in the main text. See A.1 and Figure A.1 in the Appendix A for the information.

Although not dedicated to the vertical gradient of NO_x in the BL, a few previous studies trying to link column tropospheric NO_2 to surface concentration hinted the existence of the vertical gradient [*Petritoli et al.*, 2004; *Knepp et al.*, 2013]. Assuming a well-mixed BL, these studies derived surface NO_2 ($C_{derived}$) from dividing column NO_2 measurements by BL height and compared $C_{derived}$ to surface measurements ($C_{measured}$). Regression analysis ($C_{derived} = a\ C_{measured} + b$) showed the slope, a, is always less than one, indicating that column-derived surface NO_2 tends to underestimate when NO_x is assumed to be well mixed in the BL. In addition, the observations by *Petritoli et al.* [2004] lasted for about a year in Northern Italy, so the implication of vertical NO_x gradient from their

data also underscores the pervasive existence of the phenomenon. Furthermore, *Petritoli et al.* [2004] showed that the regression slope, a, is close to one in the winter but is much lower (0.1-0.3) in the summer. This seasonal cycle of the regression slope indicates that the gradient of NO_x is more prominent in the summer than in the winter.

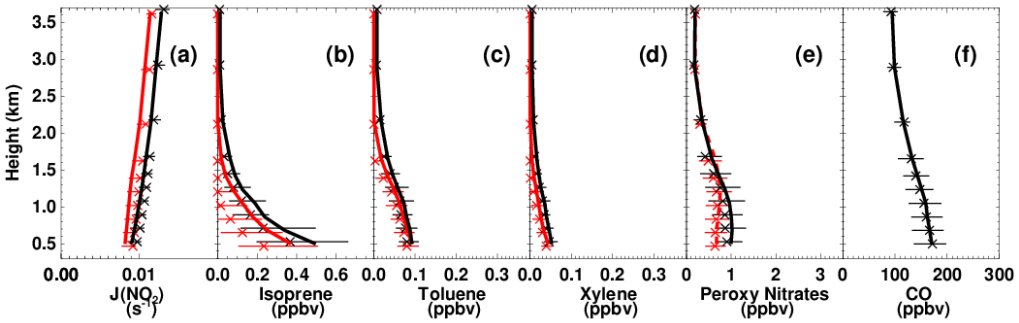

Figure 3.3 Average vertical profiles for (a) $J(NO_2)$, (b) isoprene, (c) toluene, (d) xylene, and (e) peroxy nitrates, respectively. Solid black lines denote observations and dashed red lines model results; (f) Observed average vertical profile for carbon monoxide.

3.3.2 Sensitivity of NO_x Gradient to BL Stability

Figure 3.4(a) shows that the relationship between the NO_x gradient and BL stability (i.e., potential temperature (θ) gradient) has roughly three regimes. When the BL is in the turbulent regime ($\partial\theta/\partial z < 0.1\text{K/km}$), NO_x is well mixed; when the BL is in the stable regime ($\partial\theta/\partial z > 1\text{K/km}$), the magnitude of the NO_x gradient is largest (median gradient at ~ -3 ppbv/km); most interestingly, when the BL is in the transitional regime ($0.1\text{K/km} < \partial\theta/\partial z < 1\text{K/km}$), the vertical gradient of NO_x appears to be highly sensitive to BL stability (or θ gradient). Based on this observation, we define in Section 3.2.2 the criteria for "turbulent", "neutral", and "stable" categories. The predominance of the "deep and neutral" category (Table 3.2) implies that even when the BL is well

developed it is common that the atmosphere is in the neutral or transitional regime, in which the vertical gradient of NO_x is sensitive to BL stability.

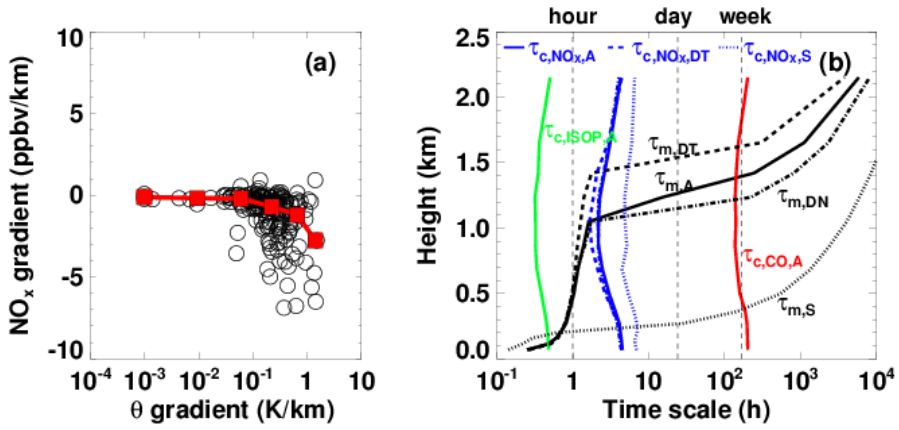

Figure 3.4 (a) Relationship between the NO_x gradient and the potential temperature (θ) gradient in the BL. Circles represent individual profiles and red squares represent the medians of NO_x gradients in θ gradient bins. The six bins are defined as 0-0.002, 0.002-0.02, 0.02-0.1, 0.1-0.5, 0.5-1, 1-10 K/km, respectively; (b) NO_x chemical lifetime ($\tau_{c,\mathrm{NO_x}}$) and vertical mixing time scale (τ_m) as a function of height in different cases: "deep and turbulent" (DT), "deep and neutral" (DN), "stable" (S), and all DISCOVER-AQ 2011 profiles (A). Note that NOx chemical lifetime in the "deep and neutral" case is not discernible from that for the all profiles and thus is not plotted. To compare, chemical lifetimes of CO ($\tau_{c,\mathrm{CO}}$) and isoprene ($\tau_{c,\mathrm{ISOP}}$) for all profiles are also plotted.

The vertical gradient over a homogeneous region is largely a result of the competition between chemical loss and turbulent mixing. While chemical loss is determined by the chemical property of the species of interest and the photochemical environment, turbulent mixing is a function of BL stability. Qualitatively, for a surface-emitted species, fast (slow) chemical loss and slow (fast) vertical mixing contribute to a large (small) vertical gradient. In Figure 3.4(b), we show average chemical life time (τ_c) and turbulent mixing time (τ_m) as a function of altitude for all categorized profiles and

each profile category. Consistent with previous studies conducted during the summer over the eastern US [*Spicer*, 1982; *Sillman*, 2000], τ_c for NO_x during DISCOVER-AQ 2011 is 2-5 hours throughout the BL, in "deep and neutral" and "deep and turbulent" cases, two dominant categories. In the "stable" case, τ_c is slightly longer (6-9 hours), likely due to cloud cover and hence reduced photochemical loss. In contrast, τ_m differs greatly under "turbulent", "neutral" and "stable" conditions. The implication of this observation is that the difference in the vertical NO_x gradient among the categories during the campaign is mainly attributable to the difference in BL stability (τ_m) rather than photochemical lifetime (τ_c). In contrast, the seasonal cycle of the vertical NO_x gradient inferred from *Petritoli et al.* [2004] can be explained by the seasonal variation in photochemical conditions (i.e., solar radiation).

Figure 3.4(b) also contrasts NO_x with other species such as isoprene and carbon monoxide (CO). Average τ_c for isoprene is less than an hour, faster than τ_m in the BL, and thus resulting in a vertical profile with strong gradient in the BL (Figure 3.3(b)). On the other hand, average τ_c for CO is about a week, much longer than τ_m, allowing a well-mixed vertical profile (Figure 3.3(f)).

3.3.3 Impact of BL and Land-surface Schemes on NO_x Vertical Profiles

The simulation of vertical profiles depends on model representations of vertical mixing. In the 1-D REAM, vertical mixing is driven by the WRF-generated parameters such as turbulent diffusivity, which is computed by BL and land-surface schemes in WRF. A number of studies compared the performance of these WRF schemes in terms of meteorological parameters such as temperature and humidity [*Gilliam and Pleim*, 2010; *Hu et al.*, 2010; *Shin and Hong*, 2011; *Xie et al.*, 2012], but few evaluated their influence

on chemical tracers [*Yerramilli et al.*, 2010; *Pleim*, 2011]. To test how the choices of BL and land-surface schemes impact vertical mixing in the 1-D REAM, we choose three BL schemes (MYJ, YSU, and ACM2) and two land-surface schemes (Noah and RUC) in WRF and evaluate their performance with the DISCOVER-AQ 2011 observations.

Figure 3.2 (b)-(e) shows the comparison of model results using aforementioned BL schemes with observations. Statistics for model performance of simulated NO_x mixing ratios, including bias, linear correlation coefficient, and root mean squared error (RMSE), are summarized in Table 3.4. In general, all these schemes are able to generate mixing parameters that result in reasonable agreement with observations. However, the performance of the BL schemes differs among profile categories. For "turbulent" categories, YSU performs better than MYJ and ACM2 because YSU generates more mixing in the BL than the other two. But for "neutral" and "stable" categories, MYJ and ACM2 outperform YSU, which overestimates vertical mixing. It is noteworthy that *Pleim* [2011] points out that the formulation of YSU is inherently inconsistent between meteorological and chemical tracers. As a result, despite YSU being a non-local scheme, its implementation in the 1-D REAM only utilizes the vertical diffusion coefficient generated from WRF. This inconsistency may cause more BL mixing with the YSU scheme in our test. On the other hand, although the inclusion of non-local terms in ACM2 does enhance vertical mixing relative to MYJ, ACM2 still seems to underestimate in "turbulent" cases. Unlike BL schemes, two land-surface schemes result in negligible difference in performance for all profile categories (Table 3.4).

Based on these results and the fact that the "deep and neutral" category dominates in DISCOVER-AQ 2011, we recommend using the ACM2 or MYJ BL scheme and the Noah or RUC land-surface scheme in WRF simulations for air pollution modeling.

Table 3.4 Performance of BL and land-surface schemes for varied profile categories. Metrics for performance of simulated NO_x mixing ratios include bias, correlation coefficient (R), and root mean squared error (RMSE). Bias and RMSE are in the unit of ppbv and R value is unitless.

	Deep & Turbulent			**Deep & Neutral**			**Medium & Neutral**			**Stable**		
	Bias	R	RMSE	Bias	R	RMSE	Bias	R	RMSE	Bias	R	RMSE
BL schemes												
MYJ	-0.23	0.66	0.94	0.01	0.46	2.17	-0.10	0.73	0.92	-0.14	0.77	1.18
YSU	-0.07	0.83	0.67	0.32	0.44	2.49	0.24	0.71	1.07	0.09	0.87	0.90
ACM2	-0.20	0.82	0.73	0.13	0.50	2.06	0.14	0.75	0.90	0.04	0.88	0.89
Land-surface schemes												
Noah	-0.23	0.66	0.94	0.01	0.46	2.17	-0.10	0.73	0.92	-0.14	0.77	1.18
RUC	-0.26	0.64	0.97	-0.01	0.44	2.20	-0.12	0.72	0.94	-0.18	0.72	1.30

3.3.4 BL-averaged Ozone Production Rate

The net ozone production rate, $P(O_3)$, calculated as the sum of reaction rates of NO with HO_2 and organic RO_2 (see Section 3.2.4 for details), quantifies how fast the in situ chemical production of ozone occurs. The calculation of $P(O_3)$ is crucial for diagnosis of the ozone production regime [*Liu et al.*, 2012a]. Most studies report surface $P(O_3)$ based on ground-level measurements [e.g., *Ren*, 2003; *Shirley et al.*, 2006; *Kanaya et al.*, 2008]. However, in principle, because of a relatively long lifetime of ozone, BL-averaged ozone production rate, $P(O_3)_{BL}$, is a more appropriate quantity to characterize the contribution of local chemistry to the surface concentration of ozone. In this regard, the ozone production rate derived from surface measurements, $P(O_3)_{surf}$, can be biased high relative to $P(O_3)_{BL}$ if a gradient of $P(O_3)$ exists in the BL. Using the 1-D REAM, *Liu*

et al. [2012a] found that the $P(O_3)_{BL}$ is about a factor of four lower than surface $P(O_3)_{surf}$ in highly polluted urban Beijing and the authors attributed it to the large gradient of NO_x in the BL. In this work, with aircraft measurements providing much more information to constrain the model, we derive vertical profiles of $P(O_3)$ and assess the uncertainty of $P(O_3)_{BL}$.

Figure 3.5 shows that $P(O_3)$ has a substantial gradient within the BL. The campaign median decreases from 10.5 ppbv/hr at 300 m to 3 ppbv/hr at 1.5 km. $P(O_3)$ of 10 ppbv/hr near the surface is comparable to previous studies conducted in US urban regions such as New York and Philadelphia [e.g., *Ren*, 2003; *Kleinman*, 2005]. The analysis also shows that ozone is produced mainly through the reaction of HO_2+NO (~80%) with minor contribution from organic RO_2+NO reactions (Figure 3.6 (a)). In contrast to NO_x, which decreases by 70% in the BL (Section 3.3.1), Figure 3.6 (b) shows that HO_2 varies slightly from 300 m to 1.5 km (<10%). Therefore, we conclude that the gradient of $P(O_3)$ results primarily from the gradient of NO_x rather than that of HO_2 or RO_2, which is consistent with *Liu et al.* [2012a]. In addition, we find that the vertical profiles of the net ozone production rate, $N(O_3)$, are similar to those of $P(O_3)$ because the ozone chemical loss rate during the campaign is relatively small (Figure 3.7).

To assess the bias induced from approximating $P(O_3)_{BL}$ as $P(O_3)_{surf}$, we calculate the relative difference between the $P(O_3)_{BL}$ and $P(O_3)$ at 300 m. The latter is a proxy for $P(O_3)_{surf}$ because we do not have true surface measurements from aircraft. As shown in Figure 3.5, $P(O_3)$ at 300 m is on average 48% larger than $P(O_3)_{BL}$, which is close to the value of 46% for the "deep and neutral" category. The relative bias becomes larger as the BL gets more stable and shallower, from 21% for the "deep and turbulent" category to

62% for the "medium and neutral" category. We also find that the relative bias between $N(O_3)_{BL}$ and $N(O_3)$ at 300 m is about 39%, varying from 12% for the "deep and turbulent" category to 55% for the "stable" category (Figure 3.7).

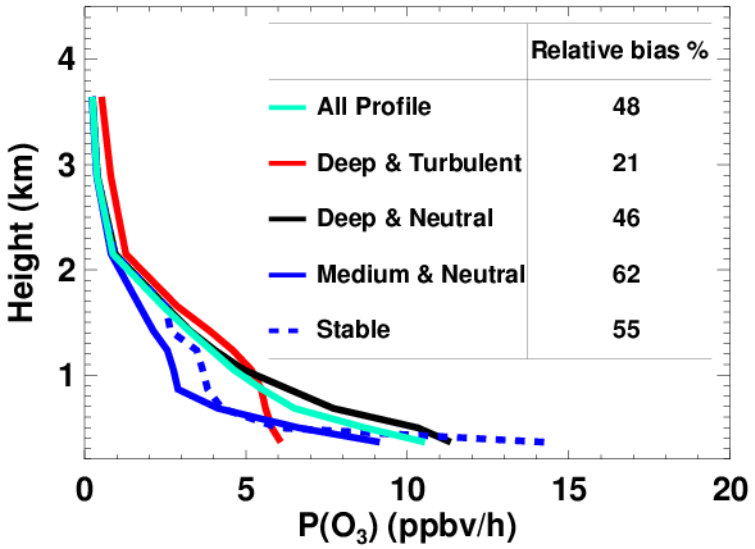

Figure 3.5 Median vertical profile of $P(O_3)$ for all profiles and each profile category. Relative biases of BL O_3 production rates calculation using an assumed well-mixed NO_x profile in the BL with NO_x measured at ~300 m ($P(O_3)_{300m}/P(O_3)_{BL}$-1) are tabulated (inset).

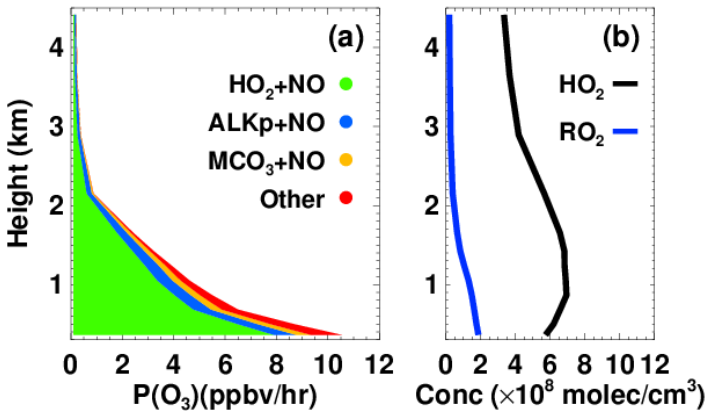

Figure 3.6 (a) Contributions of various reactions to $P(O_3)$ as a function of altitude; ALK_p represents alkane-derived peroxy radicals and MCO_3 acyl peroxy radicals; (b) Modeled vertical profiles for HO_2 (black) and RO_2 (blue).

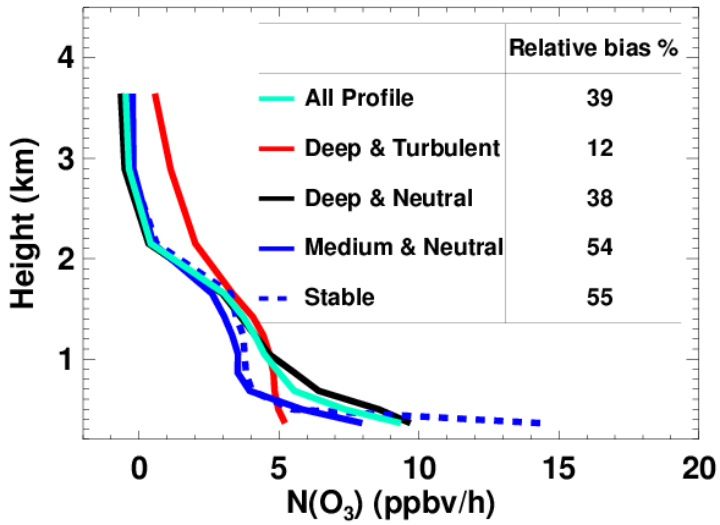

Figure 3.7 Median vertical profile of $N(O_3)$ for all profiles and each profile category. Relative biases of BL net ozone production rate calculation using an assumed well-mixed NO_x profile in the BL ($N(O_3)_{300m}/N(O_3)_{BL}$-1) are tabulated.

3.3.5 Tropospheric NO_2 Column Retrievals

Retrievals of tropospheric NO_2 columns from satellite measurements require calculation of the air mass factor (AMF), which characterizes the relationship between NO_2 abundance along the slant column (photon path from the sun to the satellite) and that in the vertical column for a given pixel [*Boersma et al.*, 2011]. In practice, the AMF is calculated as an average of altitude-dependent AMFs weighted by a prescribed NO_2 vertical profile, following the equation

$$\mathrm{AMF} = \frac{\int \mathrm{amf_h} \cdot \mathrm{c_h} \cdot d\mathrm{h}}{\int \mathrm{c_h} \cdot d\mathrm{h}},$$

where $\mathrm{amf_h}$ is the altitude-dependent AMF that describes the sensitivity to NO_2 at altitude h and is usually obtained through radiative transfer calculation, and $\mathrm{c_h}$ is the prescribed concentration of NO_2 at altitude h and is usually provided by a 3-D chemical transport model. Estimates suggest that the uncertainty in the simulated a priori NO_2

vertical profiles leads to a 5%-15% uncertainty in the calculated AMF [*Hains et al.*, 2010; *Boersma et al.*, 2011].

Various studies have been devoted to investigating how the uncertainties of NO_2 retrievals are affected by the a priori NO_2 vertical profile. While a great number of studies [e.g., *Eskes and Boersma*, 2003; *Boersma et al.*, 2011; *Russell et al.*, 2011; *Heckel et al.*, 2011] discuss the impact of the model spatial resolution on NO_2 retrievals, only a few studies have examined the impact of temporal resolution [*Lamsal et al.*, 2011; *Heckel et al.*, 2011]. However, different retrieval algorithms sample simulated vertical profile at varied temporal resolutions, ranging from daily [e.g., *Boersma et al.*, 2007], monthly [e.g., *Russell et al.*, 2011; *Valks et al.*, 2011], to annually [e.g., *Bucsela et al.*, 2006]. In this section, we use the aircraft measurements during DISCOVER-AQ 2011 to assess the impact of variability in NO_2 vertical profiles on the calculation of the AMF.

Figure 3.8 (a) shows the relative difference of AMF between individual (AMF_{ind}) and average (AMF_{avg}) vertical profiles at various sites. Note that in this case, NO_x at the lowest 300 m is specified as that at 300 m. Results that account for the lowest 300 m at two sites with available research-quality ground-level NO_2 measurements are presented in A.2 and Figure A.2 in Appendix A. Under the DISCOVER-AQ 2011 conditions, on average, using the campaign-average vertical profiles causes ~2-5% low bias. Additionally, the deviation of individual profiles from the average profile results in about ±5% difference at all sites between AMF_{ind} and AMF_{avg} (the boxes in Figure 3.8 (a) denotes the inter-quartile relative difference) and even larger difference for particular vertical profiles (the triangles in Figure 3.8 (a) denotes the largest positive or negative relative difference). We suggest that one should take into account this uncertainty in

temporal variability along with that in the horizontal resolution when developing and/or evaluating an NO_2 retrieval algorithm.

The statistics shown in Figure 3.8 (a) are quite consistent across all the sites, indicating that the variability in the AMF can be largely attributed to variability in the mixing property of the BL rather than spatial inhomogeneity. Figure 3.8 (b) shows that the AMF tends to decrease as the NO_2 gradient becomes sharper in a shallower and more stable BL. The difference in the BL category explains the ~5% variability from the AMF_{avg}, supporting the idea that the mixing property of the BL is primarily responsible for the variability of AMF observed in Figure 3.8 (a).

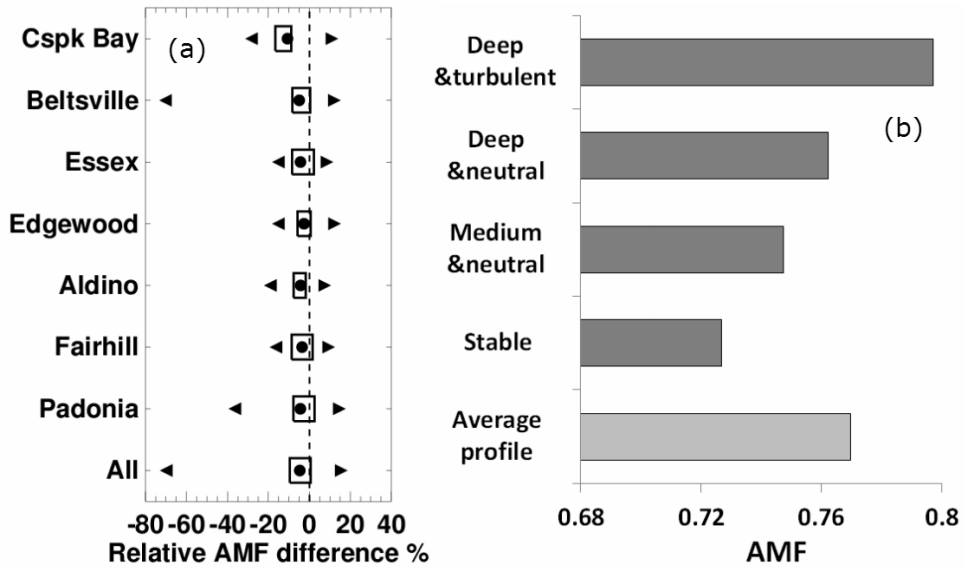

Figure 3.8 (a) Relative difference between AMF_{ind} and AMF_{avg} (AMF_{ind}/AMF_{avg}-1) at each site and for the whole campaign. Dots represent average, boxes represent interquartile ranges, and triangles represent maximum and minimum of the relative difference, respectively; (b) AMF calculated from average vertical profile for each profile category.

3.4 Summary

During DISCOVER-AQ 2011, we find frequent occurrences of significant NO_x gradients within the BL, suggesting that the well-mixed BL assumption must be applied cautiously to BL NO_x. The median vertical profile derived from aircraft spirals shows that NO_x concentration decreases by ~ 70% from 300 m to 1.4 km. The observed vertical profiles of NO_x can generally be reproduced by our 1-D photochemical model driven by WRF-generated meteorological fields. Analysis of the model results shows that the chemical lifetime of NO_x is comparable to the vertical mixing time scale in the BL, resulting in the observed sensitivity of NO_x gradient to BL stability.

Model simulations using different BL and land-surface schemes in WRF found no significant impact on the 1-D model results. All of the three boundary layer schemes (MYJ, YSU, and ACM2) were able to generate a reasonable representation of the vertical mixing under DISCOVER-AQ 2011 conditions. Non-local schemes, ACM2 and YSU, moderately improved performance in a turbulent BL, but the YSU scheme tends to overestimate in "neutral" and "stable" cases. Using two land-surface schemes (Noah and RUC) resulted in little difference in simulated NO_x vertical profiles.

The gradient of NO_x in the BL can confound the extrapolation of surface measurements to the entire BL. For example, using surface measurements in calculating the ozone production rate in the BL without considering the NO_x gradient can result in a ~45% high bias. In addition, since satellite retrieval of column density utilizes a priori vertical profiles, the model skill to reproduce a realistic vertical profile of NO_x also affects our ability to correctly retrieve tropospheric NO_2 column from satellite

measurements. Both spatial and temporal (inter-day) variations of BL NO_x vertical profiles affect the accuracy of the retrievals.

In this study, we have focused on understanding the vertical profiles of NO_x observed in July, 2011 over Washington-Baltimore region during the DISCOVER-AQ campaign. However, we expect that the large gradient of NO_x within the BL is not uncommon. More vertically resolved observations using aircraft, tethered balloon, and remote sensing techniques in other seasons and locations are necessary to understand the implications of BL NO_x gradients on various applications of surface and satellite measurements in air quality studies. In addition, all the results presented here are based on aircraft measurements at least ~300 m above ground. Model results suggest that the NO_x gradient between 300 m and surface tends to be larger than above 300 m due to surface NO_x emissions. Therefore, reliable profile measurements in the lowest few hundred meters are also an important area of future field experiments targeting air quality.

CHAPTER 4

[3]SURFACE AND TROPOSPHERIC SOURCES OF METHANESULFONIC ACID (MSA) OVER THE TROPICAL PACIFIC OCEAN

4.1 Introduction

Critical to the tropical climate system is the production of sulfate through organic sulfur emission and oxidation in marine environments [e.g., *Charlson et al.*, 1987]. Since the discovery that dimethyl sulfide (DMS) is emitted in large quantities from the ocean [*Barnard et al.*, 1982], marine sulfur chemistry has been studied extensively. The oxidation of DMS is mainly by the hydroxyl radical (OH), which converts more than half of DMS to sulfur dioxide (SO_2) [*Davis et al.*, 1998; *Davis et al.*, 1999; *Chen et al.*, 2000; *Wang et al.*, 2001]. Further oxidation of SO_2 in the gas or aerosol phase produces sulfuric acid (H_2SO_4), which can either condense onto existing particles or form new particles under favorable conditions [*Davis et al.*, 1999; *Mauldin et al.*, 1999; *Weber et al.*, 2001]. In addition to SO_2 and H_2SO_4, marine sulfur chemistry also involves other sulfur-containing compounds such as dimethyl sulfoxide (DMSO), methane sulfinic acid

---

[3] This chapter is an extension of "Surface and free tropospheric sources of methanesulfonic acid (MSA) over the tropical Pacific Ocean," published on Geophysical Research Letters in 2014. Coauthors are Yuzhong Zhang, Yuhang Wang, Burton Alonza Gray, Dasa Gu, Lee Mauldin, Christopher Cantrell, and Alan Bandy.

(MSIA), and methanesulfonic acid (MSA). These species, although believed to be important, have not been studied as extensively as DMS and SO_2.

Extensive airborne measurements onboard the NSF/NCAR C130 aircraft were carried out to study sulfur chemistry and its interaction with dynamics during the Pacific Atmospheric Sulfur Experiment (PASE) over the tropical Pacific (in the vicinity of Christmas Island, 157 °20 ′W, 1 °52 ′N) in August and September of 2007. Vertical distributions of a relatively complete set of sulfur-containing compounds, including DMS, SO_2, H_2SO_4, and MSA, were measured, providing observational constraints to test our understanding of sulfur chemistry in the marine boundary layer (MBL) and lower free troposphere (LFT) over tropical regions. Using the 1-D REAM, *Gray et al.* [2011] showed that the modeled vertical profiles of DMS and SO_2 during the PASE are in reasonable agreement with observations. They estimated an average DMS-to-SO_2 conversion efficiency of 73%. However, the budget analysis by *Faloona et al.* [2009] using PASE measurements found a close to unity conversion efficiency from DMS to SO_2. *Bandy et al.* [2011] suggested that the discrepancy might be an indication of an unknown sulfur source, whose strength is approximately half that for DMS. In this work, we analyze the vertical distributions of MSA measured during PASE to understand its sources and transport over the tropical Pacific.

The remainder of this chapter proceeds as follows. Section 4.2 describes the data and model setups. Section 4.2.1 documents the aircraft measurements from the PASE. Section 4.2.2 describes the 1-D REAM setup and the design of model experiments. Section 4.3 presents the major results. In Section 4.3.1 and 4.3.2, we use model experiments to explore the explanations for the enhancement of MSA at the surface and

in the LFT. Section 4.3.3 represents the MSA budget diagnosed from the 1-D REAM simulations. Section 4.4 discusses the implications of our findings to marine sulfur chemistry and the chemistry-climate interactions.

4.2 Data and Model Description

4.2.1 PASE Aircraft Data

During PASE, fourteen research flights using the NSF/NCAR C-130 took place. Extensive aircraft measurements were obtained in the marine boundary layer (down to ~50 m), the buffer layer (BuL, 600-1300 m), and the lower free troposphere (up to 2000 m), providing well-resolved vertical profiles from the ocean surface to ~2000 m. The sampling strategy and flight patterns are described in *Conley et al.* [2009] and *Faloona et al.* [2009]. As in the work by *Gray et al.* [2011], our analysis used only Flight 2, 3, 5, 8, 11, and 12. We excluded Flight 7 because of short sampling duration. Flights 1, 9, and 10 were excluded because of incomplete measurement data. We also eliminated Flight 4 because it was a cloud-sampling mission. We did not include the two nighttime flights (6 and 13) in our analysis because of our research focus in daytime chemistry. A more detailed discussion concerning the choice of flights can be found in *Gray et al.* [2011].

In this study, we make use of the full suite of PASE measurements such as aerosol size distribution and concentrations of MSA, DMS, SO_2, OH, CO, O_3, and water vapor. MSA was measured with selected-ion chemical-ionization mass spectrometry (SICIMS) [*Mauldin et al.*, 1999]. Dry aerosol size distributions were measured using a combination of HiGEAR DMA, OPC, and APS instrumentation [*Clarke et al.*, 2004]. To account for the uptake of water at ambient relative humidity [*Bandy et al.*, 2011], we applied a humidity correction on the aerosol size distribution and used corrected values to calculate

aerosol scavenging. DMS measurements were taken by atmospheric-pressure ionization mass spectrometers (APIMS) [*Bandy et al.*, 2002], OH was measured with selected-ion chemical-ionization mass spectrometry (SICIMS) [*Mauldin et al.*, 1998], and O_3 was recorded using a fast chemiluminescence instrument [*Ridley et al.*, 1992]. Readers can refer to *Bandy et al* [2011] for more information on the PASE measurements.

4.2.2 1-D REAM Simulations

Previously, we have applied the 1-D REAM to investigate polar photochemistry at the South Pole [*Wang et al.*, 2007], urban photochemistry in China [*Liu et al.*, 2010; *Liu et al.*, 2012], and sulfur chemistry over the tropical Pacific [*Gray et al.*, 2011]. In this work, we use the 1-D REAM, which incorporates modules for O_3-NO_x-hydrocarbon photochemistry, marine sulfur chemistry, cloud/aerosol scavenging, turbulent and convective transport, and dry/wet deposition, to analyze the vertical distribution and sources of MSA over the tropical Pacific. The sulfur chemistry module utilizes a condensed sulfur chemistry mechanism involving gas-phase species of DMS, SO_2, H_2SO_4, DMSO, $DMSO_2$, MSIA, and MSA [*Chen et al.*, 2000]. To test the possible impact of BrO, we also include the reaction between DMS and BrO in the mechanism. Kinetic data of the reactions are updated following *Zhu et al.* [2006] (Table 1.1). Vertical transport is simulated using WRF-assimilated meteorological fields based on the NCEP reanalysis data. Aerosol scavenging rate constant is calculated based on measured aerosol size distribution during the PASE [*Bandy et al.*, 2011]. We calculate the aerosol scavenging rate constant (k) using the following equation,

$$k = D_g \int \frac{2F(Kn, \gamma)}{D_p} \frac{dA}{d \log D_p} d\log D_p$$

where D_g is gas diffusivity in air, A is aerosol surface area, D_p is aerosol diameter, and F is a function of Knudsen number (Kn) and sticking coefficient (γ) [*Daheke*, 1983]. We specify a D_g value of 0.09 cm^2/s and a γ value of 0.15 for MSA [*De Bruyn et al.*, 1992; *Schweitzer et al.*, 1998].

To simulate marine sulfur chemistry, near-surface DMS concentrations are specified as the observed values and model simulated DMS profiles are in good agreement with the observations [*Gray et al.*, 2011]. We scale the simulated OH profile to match the observations and use the scaled values for sulfur chemistry calculation. In addition, observed concentrations of CO, O_3, and water vapor are also used to constrain the model. For each flight, we run the model in a 1-min time step repeatedly using the chemical constraints and meteorological fields of that day for a period of 30 days to achieve a quasi-steady state and only the results of the last day is used for analysis.

Gray et al. [2011] has shown that the 1-D REAM with such setups is able to reproduce the observed vertical profiles and daytime variations of DMS and SO_2 during the PASE (Figure 4.1). In this study, we use the model by *Gray et al.* [2011], referred to as the BASE simulation, as the starting point of our analysis. Recognizing that the BASE simulation cannot fully describe the observed vertical profile of MSA, we design several exploratory simulations with varying model configurations (Table 4.1). To investigate the sharp gradient near the surface, we specify in the near-surface layer MSA as observed, BrO as 2 pptv, and DMSO as 4 pptv, respectively, in the FIX, BrO, and DMSO simulations. To explore the cause of the enhancement of MSA in the LFT, we turn off aerosol scavenging in the LFT in the NOSCAV simulation. We further allow MSA to degas from aerosols in the DEGAS simulation, in which aerosol-phase MSA is treated as

a tracer and degassing takes place when relative humidity is lower than 40%. The aerosol-phase MSA includes MSA either directly scavenged by aerosols or rapidly produced in aqueous phase from scavenged DMSO and MSIA [*Zhu et al.*, 2006].

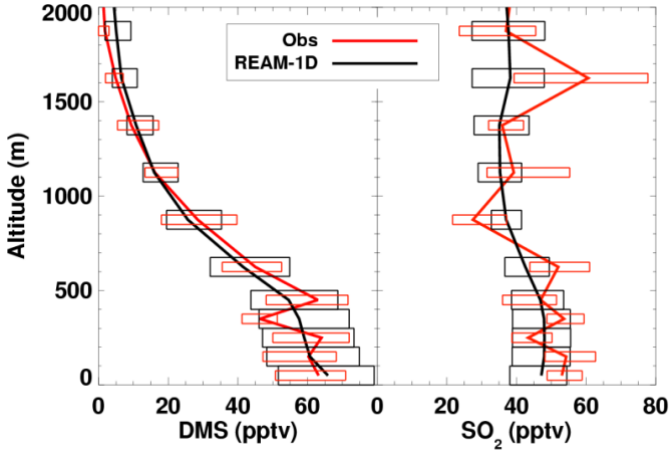

Figure 4.1 Observed and simulated daytime median vertical profiles of DMS and SO_2 from the model simulation. The red lines are observation data and black lines model results. Boxes indicate inner quartiles.

Table 4.1 Simulations conducted with the 1-D REAM in this study

Name	Description
BASE	A 1-D REAM simulation follows Gray et al. (2011). All other simulations are based on this simulation.
FIX	MSA in the bottom layer is specified to the observations.
BrO	BrO in the bottom layer is fixed at 2 pptv.
DMSO	DMSO in the bottom layer is fixed at 4 pptv.
NOSCAV	Aerosol scavenging is turned off in the LFT.
DEGAS DF10/DF20	Aerosol scavenging is turned off in the LFT. In addition, a fraction of MSA is degased from fine-mode aerosols if relative humidity is < 40%. Aerosol-phase MSA originates from scavenged MSA and MSA produced from scavenged DMSO and MSIA. We conducted two DEGAS simulations with degassing fractions (DF) of 10% and 20%, denoted as DEGAS DF10 and DEGAS DF20, respectively.

4.3 Results and Discussion

4.3.1 MSA Gradient in the MBL

One of the remarkable features revealed in the PASE data is a pronounced negative gradient of MSA from the ocean surface to ~600 m. Unlike well-mixed SO_2 [*Gray et al.*, 2011], the observed median MSA concentrations decrease rapidly in the MBL, from 2.1×10^6 molecules/cm^3 near the ocean surface to 0.6×10^6 molecules/cm^3 at 600 m (Figure 4.2). This change in concentrations translates to a negative gradient of 2.5×10^6 molecules/cm^3/km in the MBL. The BASE simulation, with chemical production from DMS oxidation being the only MSA source, fails to reproduce the gradient and significantly underestimates MSA concentrations in the lower MBL (Figure 4.2). The discrepancy between simulated and observed vertical profiles implies a missing MSA source close to the ocean surface that is not included in the BASE simulation.

Constrained with observed MSA concentrations at the surface layer, the FIX simulation is able to reproduce both the concentrations and the gradient of MSA in the MBL (Figure 4.2), supporting the idea that an additional surface source can explain the discrepancy between the observations and BASE simulation. The budget calculation of the FIX simulation indicates a missing source of 4.0×10^7 molecules/cm^2/s (Figure 4.9), which is much stronger than the estimated chemical production from DMS oxidation (9.0×10^6 molecules/cm^2/s). The comparison between daytime and before-dawn measurements (Figure 4.3) implies that this source is photolytically enhanced in daytime. However, we cannot conclusively determine the nature of this source using only the observations from the PASE. We therefore explore several possible mechanisms with the aid of the 1-D model.

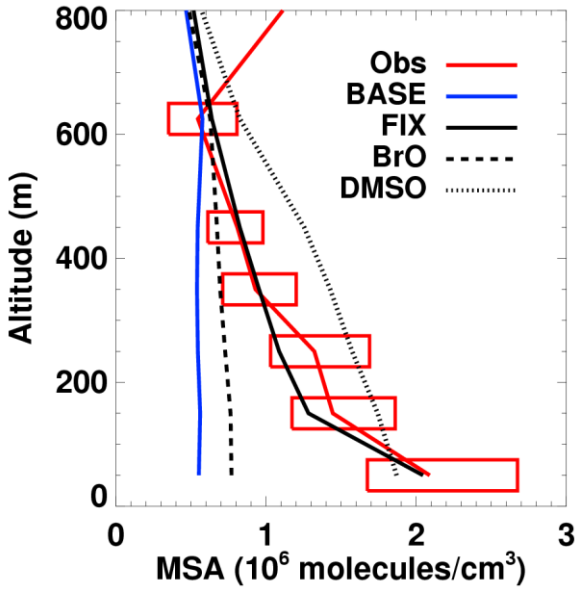

Figure 4.2 Observed and simulated daytime median vertical profiles of MSA in the MBL. Observational data are represented with red solid lines. Red boxes indicate inner quartiles. Model results from BASE, FIX, BrO, and DMSO simulations are shown with blue solid, black solid, black dashed, and black dotted lines, respectively.

One possible explanation is the oxidation of DMS by BrO, which is not modeled in the BASE simulation. Since the DMS+BrO reaction is through the addition channel, which favors MSA production, it is plausible that the DMS+BrO reaction contributes to the missing source of MSA. Previous studies on the PASE (e.g., *Gray et al.* [2011]) found that based on SO_2 simulations, they could not either prove or rule out the presence of BrO in the MBL at a level of 1 pptv. To test the impact of BrO on MSA production, we assume in the BrO simulation the daily maximum BrO mixing ratio at the ocean surface to be 2 pptv. The BrO simulation results in the additional chemical production of MSA of 1.0×10^6 molecules/cm^2/s. This addition, however, is insignificant in comparison to the missing source of 4.0×10^7 molecules/cm^2/s and is unable to sustain the negative

gradient in the MBL (Figure 4.2). Therefore, we conclude that the presence of BrO, if any, is unlikely to be the primary reason for the missing source of MSA.

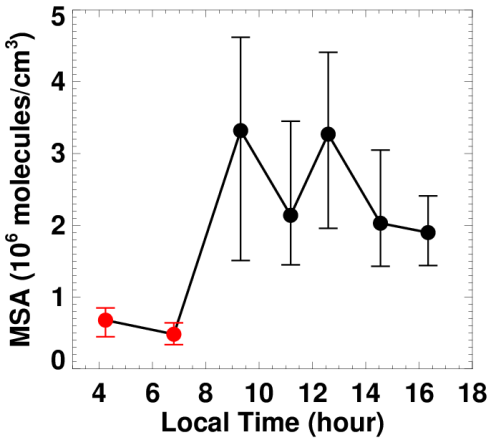

Figure 4.3 Diurnal variation of MSA near the surface (0-200) m. Red and black dots represent median MSA concentrations from a before-dawn flight (Flight 13) and daytime flights (Flight 2, 3, 5, 8, 11, and 12), respectively. Vertical (error) bars represent the interquartile ranges of the data.

Another possible reason for the underestimation of MSA production can be uncounted-for sources of MSA precursors such as DMSO. Unexpected high levels of DMSO (10-50 pptv) have been previously reported over the tropical ocean [*Bandy et al.*, 1996; *Nowak et al.*, 2001]. Although DMSO measurements are unfortunately unavailable in the PASE, we are able to test the impact of high DMSO concentrations on MSA production with the model. In the DMSO simulation, we fix surface DMSO at 4 pptv, a moderately high concentration [*Nowak et al.*, 2001]. The enhanced DMSO concentrations increase the chemical production of MSA to 4.9×10^7 molecules/cm^2/s, which is comparable to the strength of the missing source. However, the median vertical gradient of MSA from the DMSO simulation appears to be smaller than observations (Figure 4.2). The gradient is not maintained in the model because DMSO is vertically mixed in the

MBL and the resulting MSA production from DMSO is not limited to the surface layer (as in the FIX case), leading to a model overestimate in most of the MBL. Despite imperfect agreement between the simulated and observed gradients, the results underscore the potential role of DMSO in MSA production. To further test this hypothesis, future studies require concurrent measurements of DMSO and MSA.

In addition to unidentified chemistry, another possible explanation for the missing source of MSA is a primary emission directly from the ocean. This explanation is supported by the correlation between MSA concentrations and wind speeds in lower altitudes (<200m) (Figure 4.4). However, this correlation can also be a signal that MSA is being produced from very reactive sulfur species emitted from the ocean. Furthermore, because MSA is far more soluble than DMS (Henry's law constant is 10^{15} for MSA and 0.5 mole kg^{-1} atm^{-1} for DMS), it cannot easily degas from the water surface, unless aided by other mechanisms such as a thin organic film at the surface of the ocean, in which MSA is moderately soluble.

4.3.2 MSA Increase in the LFT

The vertical profile of MSA observed during PASE features a large increase in the LFT. The average mixing ratio of MSA in the LFT is 2.2×10^7 molecules/cm^3, one order of magnitude larger than that in the MBL (Figure 4.5a). Similar features of enhanced MSA in the free troposphere are also found in the data from the PEM-A and PEM-B campaigns [*Davis et al.*, 1999; *Mauldin et al.*, 1999] (Figure 4.6). Analyses of measurements show that the controlling factor of the MSA concentrations in the LFT is humidity. Figure 4.5 also shows that MSA concentrations are negatively correlated with

relative humidity (RH) in the LFT during PASE. Similar relationships between MSA and RH in the LFT are also found in PEM-A and PEM-B data (Figure 4.6).

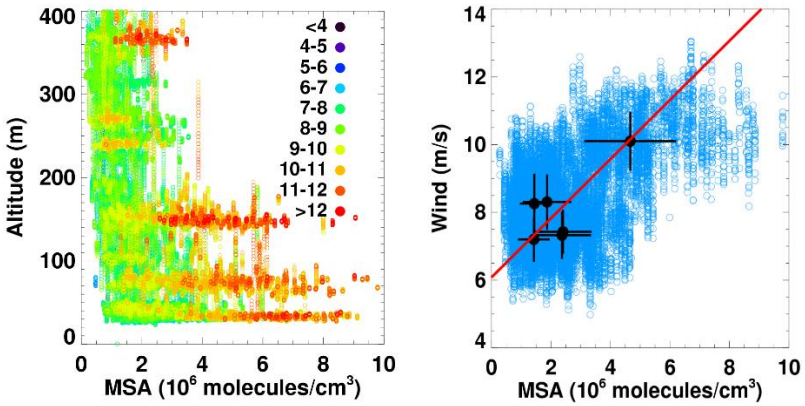

Figure 4.4 (Left) MSA observational raw data, with different colors reflecting wind speeds. (Right) Scatter plot of wind speed and MSA concentration below 200 m. Blue dots represent raw data. Black dots represent flight averages, with bars indicating standard deviations. The red line represents a least-squares regression of the observation data.

The BASE simulation fails to reproduce MSA enhancement in the LFT. Recognizing that the affinity of gaseous MSA to aerosols is mainly due to its high solubility and that aerosols in the dry LFT tend to lose their water content, we perform the NOSCAV simulation, in which we turn off aerosol scavenging in the LFT. With the NOSCAV simulation, the model is able to generate a peak at the right altitude (~2 km), but the magnitude (0.7×10^7 molecules/cm^3 at 2 km) is still much smaller than the observations (an average of 2.2×10^7 molecules/cm^3 at 2 km) (Figure 4.5a). Model analysis shows that to reproduce the observed magnitude would require a source of MSA in the LFT at ~1.2×10^7 molecules/cm^2/s (Figure 4.9).

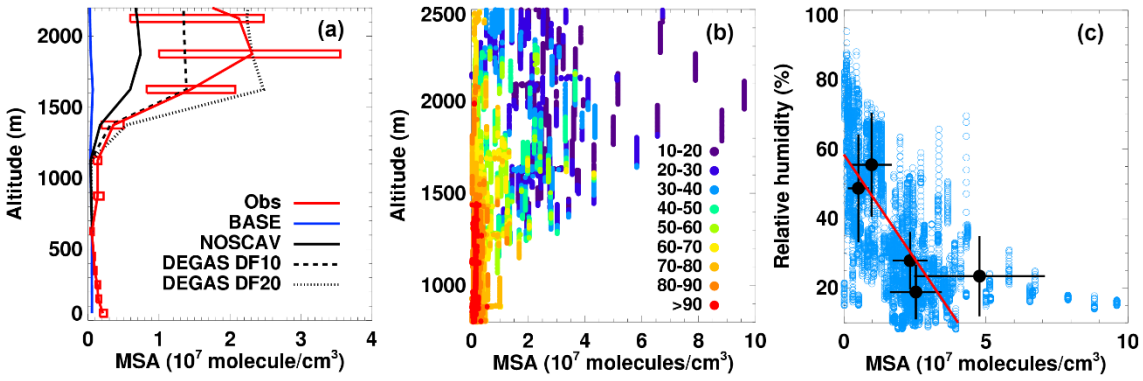

Figure 4.5 (a) Observed and simulated daytime median vertical profiles of MSA from surface to 2000 m. Observational data are represented with red lines. Red boxes indicate inner quartiles. Model results from BASE, NOSCAV, DEGAS DF10, and DEGAS DF20 simulations are shown with blue solid, black solid, black dashed, and black dotted lines, respectively. (b) Raw observational data of MSA in LFT, with color showing relative humidity (%). (c) Relative humidity and MSA concentrations anti-correlation in LFT. Blue dots represent raw data. Black dots represent flight averages, with bars indicating standard deviations. The red line represents a least-squares regression of the observation data.

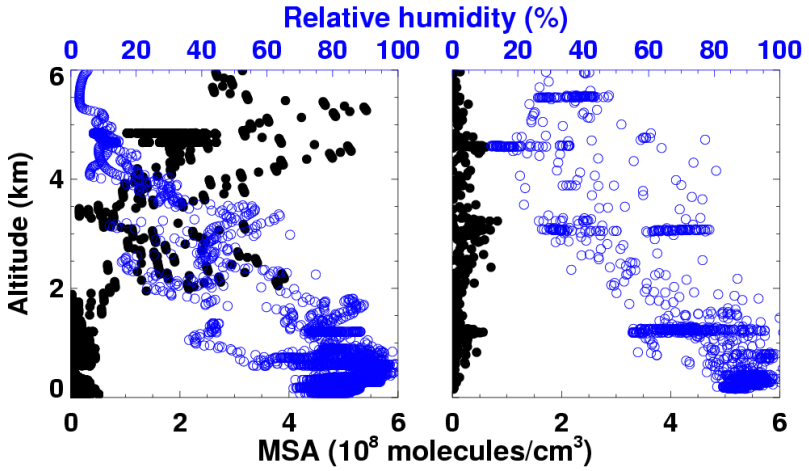

Figure 4.6 Observation data of MSA and relative humidity in PEM-Tropics A (left) and PEM-Tropics B (right) as a function of altitude.

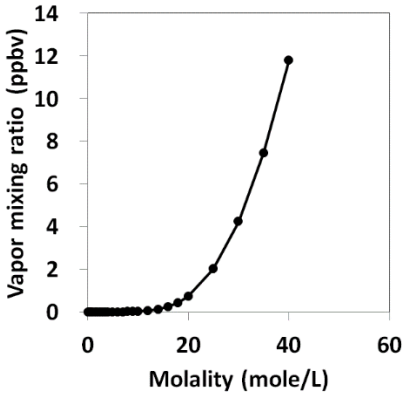

Figure 4.7 MSA vapor pressure as a function of its concentration in water solution Adapted from *Covington et al.* [1973] and *Hoppel* [1987].

We hypothesize that the source of MSA in the LFT is degassing from aerosols as a result of high vapor pressure in the dry LFT. Previous experiments showed that the vapor pressure of MSA increases rapidly as the concentration of the solution increases (about 10 ppbv at 40 mole/L, see Figure 4.7) [*Covington et al.*, 1973; *Hoppel*, 1987]. To maintain equilibrium, MSA tends to degas from dehydrated aerosols in the dry LFT, which constitutes a non-negligible source of MSA in the LFT. Since a full description of degassing entails detailed modeling of aerosols (e.g., composition, structure, acidity, efflorescence process, etc.), which is beyond the scope of this study, here we describe degassing with a simplified model that requires two parameters, an efflorescence point (EP) and a degassing fraction (DF). In the DEGAS simulation, we assign an EP of 40% (a value close to the EP of sea salt); a RH value of 40% also separates two clusters of high and low MSA observations during PASE (Figure 4.5c). We carry out a series of sensitivity simulations, and determine the best estimate of DF to be 10-20%. Figure 4.5a shows that the DEGAS simulations with a 40% EP and a DF between 10% and 20% are able to bracket the observed median profile. More detailed simulation of the degassing

mechanism requires more information on the microphysical property of PASE aerosols, which we do not currently have.

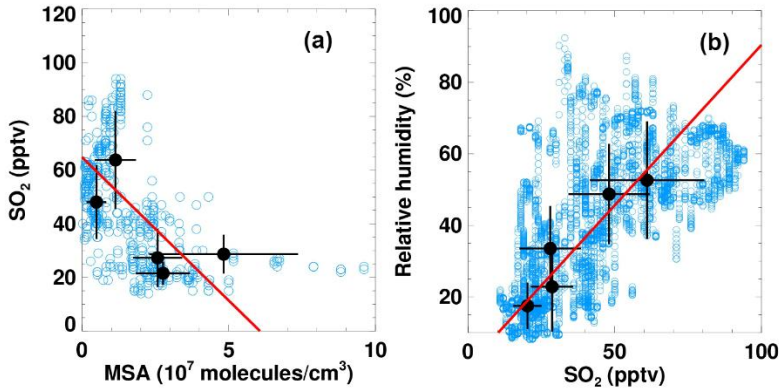

Figure 4.8 (a) Observed negative correlation between MSA and SO2, and (b) positive correlation between SO2 and relative humidity in the LFT (1500-2500 m) are consistent with the degassing mechanism rather than long-range transport of MSA along with SO2. Blue dots represent raw data. Black dots represent flight averages, with bars indicating standard deviations. The red line represents a least-squares regression of the observation data.

An alternative explanation of the LFT source relates to the long-range transport of MSA in the dry LFT. Previous studies have speculated that long-range transport contributes to SO_2 in the LFT [*Gray et al.*, 2011] and high CCN concentrations [*Hudson and Noble*, 2009] during PASE. Back-trajectory from the NOAA HISPLIT model also suggests that the air mass in the LFT encountered in the PASE was advected from a region with intensive biogenic activity over the East Pacific [*Gray et al.*, 2011]. Although we are unable to simulate long-range transport because of the limitation of the 1-D model, observational evidence suggests that long-range transport is unlikely a major contributor to the enhancement of MSA in the LFT. The sharp increase of MSA from 1500-2000 m is inconsistent with a uniform vertical distribution of SO_2 as result of advection and vertical transport [*Gray et al.*, 2011]. In addition, we cannot find a positive

correlation between MSA and SO_2 if long-range transport is significant. In contrast, observations show a negative correlation between MSA and SO_2 in the LFT (Figure 4.8). Furthermore, relative humidity is negatively correlated with MSA (Figure 4.5c) but is positively correlated with SO_2 (Figure 4.8) in the LFT. These relationships are all consistent with degassing MSA in the LFT under dry conditions.

4.3.3 MSA Budget during the PASE

Figure 4.9 summarizes the MSA budget in the MBL, the BuL, and the LFT, with a focus on required sources to explain the observations in the MBL and the LFT. In the MBL, we identify a missing source of 4.0×10^7 molecules/cm^2/s from the ocean surface. In contrast, chemical production from DMS oxidation constitutes only 9.0×10^6 molecules/cm^2/s on a daily basis. For sinks, dry deposition (2.0×10^6 molecules/cm^2/s) is small relative to the missing source. The dominant sink in the MBL is aerosol scavenging (4.7×10^7 molecules/cm^2/s). However, since the strength of aerosol scavenging varies little with altitude in the MBL (Figure 4.10), the missing source from the surface is manifested by the observed negative concentration gradient in the MBL. In the LFT, degassing from aerosols constitutes an important source of 1.2×10^7 molecules/cm^2/s. The strength of chemical production in the LFT is 2.0×10^6 molecules/cm^2/s on a daily basis. Unlike in the MBL, the sink of aerosol scavenging is negligible owing to dry conditions in the LFT. The sole significant sink in the LFT is transport to the BuL, which is estimated at 1.6×10^7 molecules/cm^2/s. The total source strength in the LFT, the sum of degassing and chemical production, is much less than that in the MBL, but the weak sink and thus a long lifetime implies a much higher concentration of MSA in the LFT.

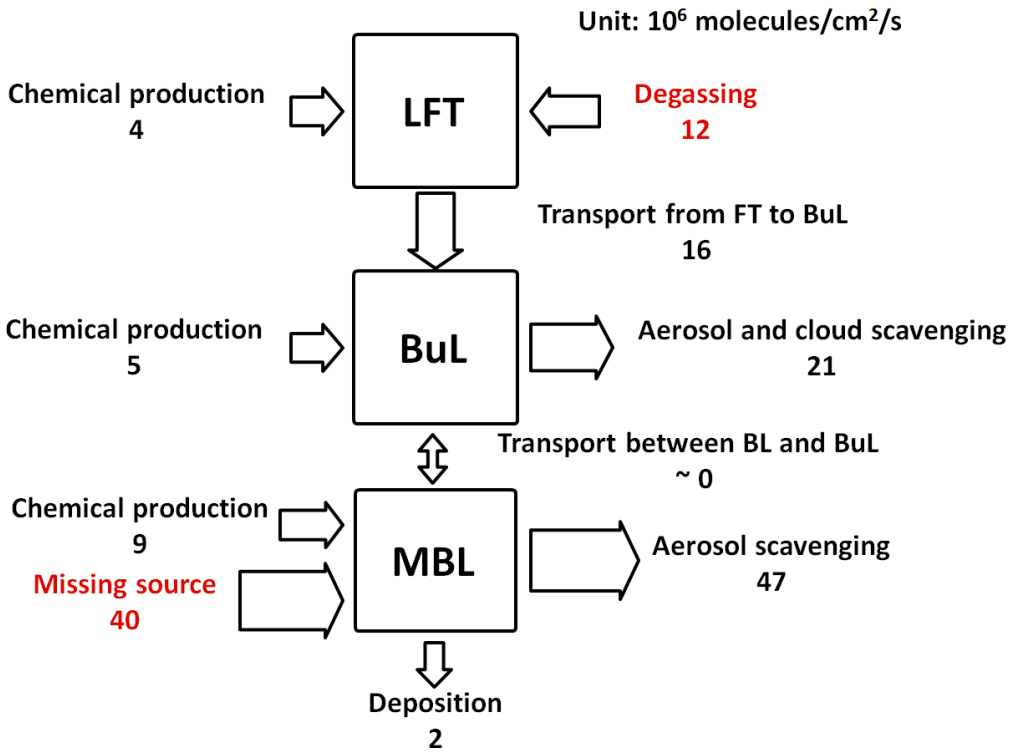

Figure 4.9 The budget of MSA in the MBL, the BuL, and the LFT.

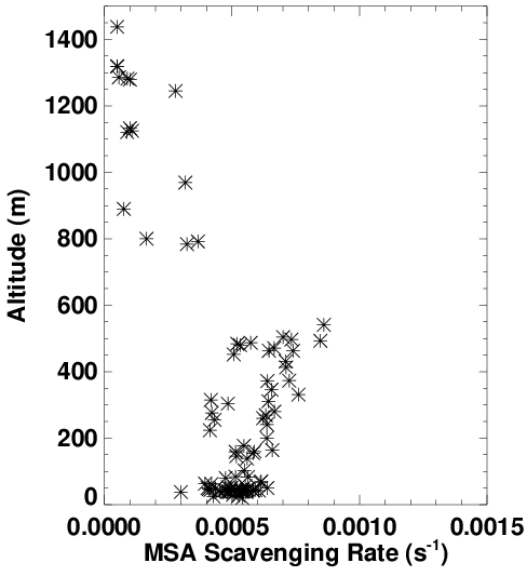

Figure 4.10. Vertical distribution of the MSA aerosol scavenging rate constant during PASE.

4.4 Summary and Implications

The budget of MSA shown in Figure 4.9 highlights the missing surface source in the MBL and the degassing source in the LFT. Previous studies indicate that our knowledge of oceanic sulfur sources may be incomplete. For example, *Bandy* et al. [2011] suggested that the discrepancy in DMS-to-SO_2 conversion efficiency from two PASE studies [*Gray et al.,* 2011; *Faloona et al.,* 2009] can be reconciled if an additional oceanic sulfur source, half as strong as the DMS source, is present. The additional surface MSA source found here is only 2% of the DMS source during PASE, thus it is insufficient to reconcile the discrepancy. However, this MSA source may represent a group of organic sulfur compounds that have significant oceanic sources. If true, it would have significant implications to the marine sulfur budget and climate feedbacks over the tropical ocean. Model sensitivity analysis indicates that halogen (~1 pptv of BrO) oxidation of DMS is not a major contributor to MSA but MSA directly emitted or chemically produced could be important. Concurrent DMSO and MSA measurements will be necessary to constrain the model simulations presented here.

This study suggests that aerosols can act as a source of MSA under dry conditions (e.g., the LFT in the PASE). We note that the net transport between the MBL and BuL is negligible (Figure 4.9), indicating that gas-phase MSA above the MBL is almost exclusively due to degassing from the aerosol phase. In addition, degassed MSA is not only MSA that aerosols scavenged elsewhere but also MSA produced from DMSO and MSIA in the aerosol phase [*Davis et al.*, 1999; *Zhu et al.*, 2006]. Therefore, the degassing source of MSA greatly enhances the apparent DMS-to-MSA conversion efficiency, which is quite small if only gas-phase chemistry is accounted for. Furthermore, after

transporting to humid and/or cold regions, these MSA gases may become an important contributor to new particle formation in the free troposphere [*Hoppel*, 1987]. For example, *Froyd et al.* [2009] reported previously that the enhancement of MSA/(MSA+sulfate) to ~0.5 in the aerosol phase in the upper free troposphere is accompanied by frequent formation of new particles (50% of flight time) over the tropical Pacific Ocean.

Our results suggest that degassing from dehydrated aerosols of soluble compounds like MSA could potentially provide important precursors for new particle formation in the free troposphere over the tropics, affecting the climate system through aerosol-cloud interactions. More broadly, we propose that aerosols may be an important media for transporting a suite of (sulfur or other) soluble compounds from the marine boundary layer to the free troposphere through the degasing mechanism. The potential for new particle formation from these soluble gases and the resulting climate forcing in the tropics will require targeted field experiments and modeling analysis to address.

CHAPTER 5

CONCLUSIONS AND FUTURE WORK

5.1 Summary of Findings

5.1.1 Novel Mechanisms Potentially Important in Chemistry-Climate Interactions

This dissertation discovers two novel important mechanisms of chemistry-climate interactions. First, our analysis in Chapter 2 reveals that the warm and dry weather is the main reason causing the high ozone extreme in October 2010. During the episodes, reduced ventilation, reduced cloud fraction, enhanced photochemistry, and increased biogenic isoprene emissions due to temperature all contribute to increased regional $[O_3]_{MDA8}$. In addition, we propose that the enhanced biogenic isoprene emissions from water-stressed vegetation contributes another ~ 5-10 ppbv to the regional $[O_3]_{MDA8}$ over the SE during the three episodes in October 2010. The mechanism is not well-known, but is supported by laboratory and field observations. The mechanism is also consistent with the strong relationship between $[O_3]_{MDA8}$ and humidity (both RH and VPD). Because the chemistry regime shifts to VOC-sensitive during the fall, this mechanism, likely to be ineffective in the summer, can have a large impact on ground-level ozone in the fall, indicating that the fall is more vulnerable to the climate change through the climate-biosphere-chemistry feedback.

Second, our analysis in Chapter 4 indicates that dehydrated aerosols release gaseous MSA to the LFT. The degassing mechanism adds a large amount of MSA to the clean LFT. When the environment is cold and /or wet, the gaseous MSA in the LFT may form new particles, which upon growth affects the radiation budget. Our analysis also

finds that unknown surface emissions rather than Br chemistry result in the vertical gradient of MSA in the MBL. The unknown source can either be MSA or other unknown reactive sulfur compounds. This result underscores the incompleteness of our knowledge of marine sulfur emissions. Budget of MSA diagnosed reveals an interesting picture: (1) most MSA, DMSO, and MSIA in the MBL are removed by aerosols; (2) some of these aerosols are lifted into the LFT, dehydrated, and release MSA into the gas phase. Part of the degassed MSA is generated from DMSO and MSIA through aqueous reactions in the aerosol phase. Therefore, the apparent DMS-to-MSA conversion efficiency is much higher in the LFT than that in the MBL. In addition, because of the long life time in the LFT, MSA can potentially transport a long distance, impacting the new particle formation in a large area.

5.1.2 Temperature is Not a Perfect Proxy for the Climate Penalty

Current discussions on the ozone climate penalty (the response of ground-level ozone to climate change) mainly focus on the ozone-temperature relationship [*Jacob and Winner*, 2009; *Rasmussen et al.*, 2012; *Rasmussen et al.*, 2013; *Wu et al.*, 2008], in which temperature is assumed to be a good proxy for all climate factors that impact on ground-level ozone. Our results suggest that humidity, in addition to temperature, may be a key factor for the extension of the ozone season through the feedback of humidity on isoprene emissions. Our analysis also shows that temperature and humidity are not well correlated over the SE during the fall. Furthermore, the statistical analysis (Chapter 2) finds that relationships between meteorological parameters and ground-level ozone vary with season and region. Therefore, using only temperature projection to estimate the change of

ozone concentration due to climate change can potentially lead to misleading conclusions.

Climate model simulations (e.g., GFDL, CESM, and GISS) project a decreasing trend of humidity over the SE region in next 50 years. Some of these models even project frequent occurrence of dry extremes. Although the regional projection of humidity is still subject to great uncertainties, our work highlights the complexity of climate-biosphere-chemistry interactions and we suggest that the effect be included in the evaluation of the challenge to the air quality control in the future.

5.1.3 Implications for Air Quality Management

Sensitivity simulations (Chapter 2) demonstrate that the extension of the ozone season is mainly driven by the climate factors (e.g., enhanced biogenic emissions in response to increased temperature and reduced humidity). Although the absolute strength of isoprene emissions in the fall is much smaller than that in the summer, even during extreme episodes like October 2010, ground-level ozone during the fall is very sensitive to biogenic emissions. Because of the chemical regime shifts from NO_x-sensitive in the summer to VOC-sensitive in the fall, a moderate increase in biogenic emissions has a large impact on the ground-level ozone concentration. Our simulation also shows that further reduction of anthropogenic NO_x emissions is not very effective in reducing ground-level ozone. Therefore, air quality management will face the challenge of the extension of the ozone season driven by climate change and diminished benefit from controlling anthropogenic NO_x emissions. However, controlling measurements that aim at mitigating climate change can benefit air quality management.

5.1.4 Not-So-Well-Mixed Boundary Layer and its Implications

We find in DISCOVER-AQ aircraft data frequent occurrences of significant NO_x gradients within the BL (Chapter 3), suggesting that the widely-used well-mixed BL assumption must be applied cautiously to BL NO_x. The median vertical profile derived from aircraft spirals shows that NO_x concentration decreases by ~ 70% from 300 m to 1.4 km. Although we have focused on the vertical profiles of NO_x observed in July, 2011 over Washington-Baltimore region during the DISCOVER-AQ campaign, we expect that the large gradient of NO_x within the BL is not uncommon.

Observed NO_x gradient in the BL is highly sensitive to BL stability, which is a result of competition between chemistry and vertical mixing. Analysis of the 1-D model results shows that the chemical lifetime of NO_x is comparable to the vertical mixing time scale in the BL. The sensitivity of NO_x gradient to BL stability can mainly be explained by the variation in the vertical mixing strength. This result implicates another way that ozone chemistry interacts with climate.

The gradient of NO_x in the BL can confound the extrapolation of surface measurements to the entire BL. For example, using surface measurements in calculating the ozone production rate in the BL without considering the NO_x vertical gradient can result in a ~45% high bias. In addition, since satellite retrieval of column density utilizes a priori vertical profiles, the model skill to reproduce a realistic vertical profile of NO_x also affects our ability to correctly retrieve tropospheric NO_2 column from satellite measurements. Both spatial and temporal (inter-day) variations of BL NO_x vertical profiles affect the accuracy of the retrievals.

5.2 Recommendations for Future Work

5.2.1 Regional and Seasonal Feature of the Climate Impact

In this dissertation, we have studied the climate-driven ozone extremes over the SE region during October. The statistical analysis presented in Chapter 2 have shown that relationships between meteorological parameters and ground-level ozone vary with season and region. As a next step, research efforts should be made to extend the analysis to other regions and seasons.

In addition, the present work focuses on the extreme case of October 2010. I recommend future work to conduct long-term simulations (more than 10 years) to evaluate the model performance on the ozone-meteorology relationship and assess the relative importance of anthropogenic emissions and climate factors on a climate-relevant time horizon.

5.2.2 The Climate-Biosphere-Chemistry Feedback

In this dissertation, we propose a climate-biosphere-chemistry mechanism involving the humidity dependence of biogenic isoprene emissions. Although results from some laboratory and field measurements support this idea, the mechanism has not been thoroughly studied. Often focusing on the temperature impact during the growing season, the existing studies on biogenic isoprene emissions have largely overlooked the humidity effect and the fall season. Answers to the following questions are still not clear: "Does the humidity effect exist for most plant types", "Is the humidity effect only significant in the fall" and "Does the humidity effect vary with the course of a drought?" Therefore, future laboratory and field studies are necessary to fill the gap.

5.2.3 Vertical Distributions of Ozone Precursors in the BL

This dissertation uses only measurements sampled in DISCOVER-AQ 2011 over the Washington-Baltimore region during the summer. More vertically resolved observations using aircraft, tethered balloon, and remote sensing techniques in other seasons and locations are necessary to understand the implications of BL NO_x gradients on various applications of surface and satellite measurements in air quality studies.

In addition, most results presented in Chapter 3 are based on aircraft measurements at least ~300 m above ground. Model results suggest that the NO_x gradient between 300 m and surface tends to be larger than above 300 m due to surface NO_x emissions. Therefore, reliable profile measurements in the lowest few hundred meters are also an important area of future field experiments targeting air quality.

5.2.4 Impact of Free Tropospheric MSA on the Radiation Budget

This dissertation explores the surface and free tropospheric sources for MSA. The degassing of MSA from aerosols enhances the concentrations of MSA in the LFT. When in a cold, wet, and clean environment, MSA can form new particles, which can grow into fine-mode aerosols that attenuate solar radiation. These aerosols can also affect the formation, duration, and whiteness of clouds, and thus poses indirect effects on the radiation budget. While the current work focuses on exploring the mechanism, a future effort could be devoted to evaluating the impact of free tropospheric MSA on the global radiation budget.

APPENDIX A

AUXILURY MATERIALS FOR CHAPTER 3

The auxiliary materials for Chapter 3 include: discussions on (1) the vertical profile of NO_x in the lowest 300 m of the BL, (2) impact of the lowest 300 m on AMF calculation; (3) comparison of isoprene flux between diagnosis from the 1-D REAM and computed by MEGAN. Three additional figures are also included.

A.1 Vertical Profile of NO_x Extending to the Surface

Research-quality ground-level NO_x measurements are available at Padonia and Edgewood. Combined with aircraft-measured vertical profiles, concurrent measurements at surface sites provide additional information about the vertical distribution of NO_x in the lowest 300 m of the BL. Two distinct pictures, however, emerge from the two sites with available surface NO_x measurements: a great enhancement towards the surface in Padonia (Figure A.1 (b)) but a small difference between the surface and 300 m in Edgewood (Figure A.1 (c)). Constrained with surface-measured NO_x, 1-D REAM is able to reproduce the observed vertical profile with reasonable satisfaction in Padonia but failed to do so in Edgewood. Given that Edgewood is under the influence of the bay breeze during the daytime [*Stauffer et al.*, 2012], the failure in Edgewood is likely due to the limitation that a 1-D model is unable to resolve horizontal transport. However, we argue that in a source region without complication of terrain and land-water contrast, the sharp NO_x gradient in the lowest part of the BL found in Padonia is probably more representative. As a matter of fact, a recent study in Paris, France also reported a large gradient of NO_x within the lowest 300 m [*Dieudonné et al.*, 2013].

A.2 Impact of the Lowest 300 m on AMF Calculation

Figure A.2 shows the comparison of AMF calculated with constant NO_2 concentration versus observed gradients in the lowest 300m in Padonia and Edgewood. On average, the strong near-surface NO_2 gradient observed in Padonia leads to a considerably smaller AMF (0.76) than the AMF (0.80) calculated from a well-mixed lowest 300 m. Although what we are after here is the amount of NO_2 in the whole tropospheric column, this nontrivial difference (~5%) highlights the importance of the NO_2 gradient in the lowest 300 m of the BL.

A.3 Validation of Isoprene Flux

We utilize the 1-D REAM to diagnose the upward isoprene flux at ~ 300 m and compare the results with MEGAN results. MEGAN is an algorithm to compute biogenic emissions (e.g., isoprene) from terrestrial ecosystem. Despite its wide use, comparisons between MEGAN emissions and observed over-canopy flux in the eastern U.S. have rarely been documented. The few studies that has explored this issue [e.g., *Palmer et al.*, 2006; *Müller et al.*, 2008] report that MEGAN-calculated isoprene emissions are within a factor of two of observations and track well the observed day-to-day variations [*Palmer et al.*, 2006; *Müller et al.*, 2008]. Based on the success in reasonably reproducing the vertical profile of isoprene, we diagnose the upward isoprene flux into the lowest model layer (denoted as EMIS as it is a proxy of emissions) as

$$\mathrm{EMIS} = \frac{\partial[\mathrm{ISOP}]}{\partial \mathrm{t}} + \mathrm{FluxOut} + \mathrm{ChemLoss},$$

where $\frac{\partial[\mathrm{ISOP}]}{\partial \mathrm{t}}$ is the local tendency of isoprene concentration, FluxOut is the turbulent diffusion flux out of the upper boundary of the layer, and ChemLoss is the chemical loss of isoprene. All terms on right-hand side can be diagnosed from model results.

Figure A.3 shows that isoprene emissions calculated by MEGAN are generally within a factor of two of the isoprene flux diagnosed in 1-D REAM. In addition, the good correlation between MEGAN-calculated and REAM-diagnosed emissions indicates that MEGAN is able to capture the short-term variations of isoprene emissions in response to environmental factors such as radiation and temperature.

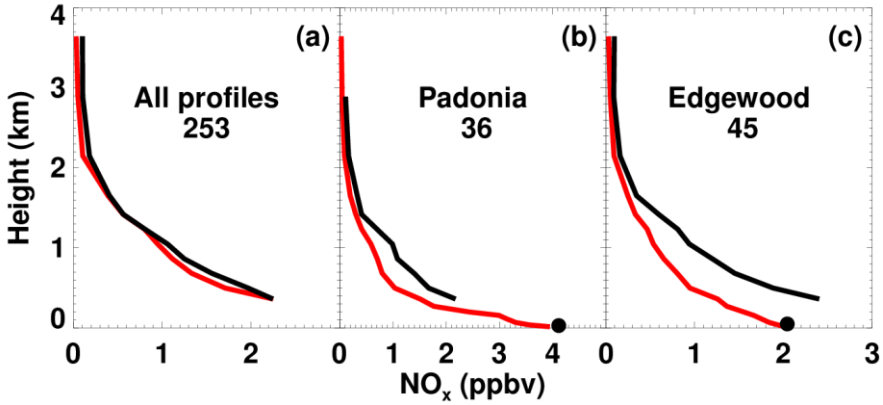

Figure A.1 Observed (black) and modeled (red) median vertical profiles of NO_x for all sites (a), Padonia (b), and Edgewood (c), respectively. The model is constrained by aircraft NO_x measurements at 300 m in (a) and surface NO_x measurements in (b) and (c). Black dots indicate the median for surface measurements. The numbers in the legend represent the count of vertical profiles.

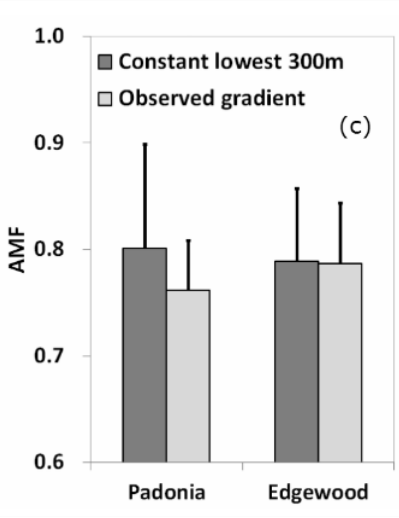

Figure A.2 AMF calculated from vertical profiles with constant NO_x in lowest 300 m or with observed NO_x gradient in lowest 300 m.

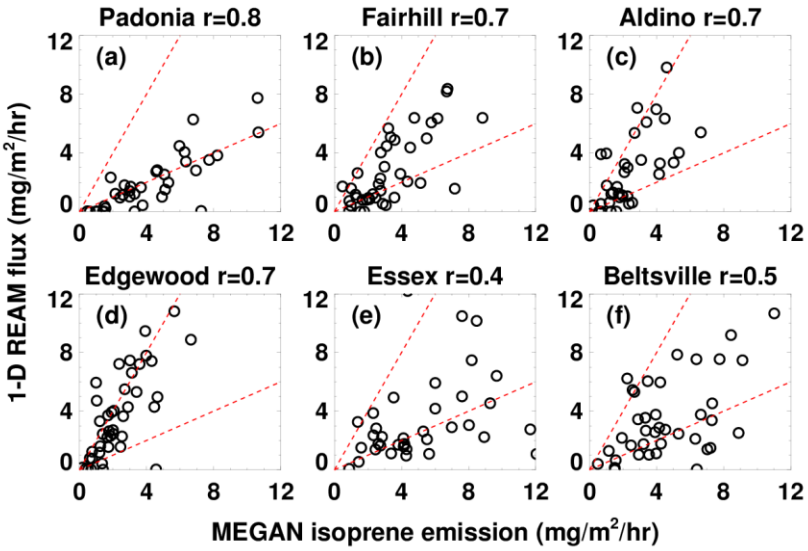

Figure A.3 Comparison between isoprene emission flux diagnosed from 1-D REAM and that calculated from MEGAN at each site. Dashed red lines bracket the area with a factor of two bias.

REFERENCES

Avise, J., J. Chen, B. Lamb, C. Wiedinmyer, A. Guenther, E. Salathé, and C. Mass (2009), Attribution of projected changes in summertime US ozone and PM2.5 concentrations to global changes, Atmos. Chem. Phys., 9(4), 1111-1124.

Bandy, A., D. C. Thornton, B. W. Blomquist, S. Chen, T. P. Wade, J. C. Ianni, G. M. Mitchell, and W. Nadler (1996), Chemistry of dimethyl sulfide in the equatorial Pacific atmosphere, Geophysical Research Letters, 23(7), 741-744.

Bandy, A., et al. (2011), Pacific Atmospheric Sulfur Experiment (PASE): dynamics and chemistry of the south Pacific tropical trade wind regime, Journal of Atmospheric Chemistry, 68(1), 5-25.

Bandy, A. R., D. C. Thornton, F. H. Tu, B. W. Blomquist, W. Nadler, G. M. Mitchell, and D. H. Lenschow (2002), Determination of the vertical flux of dimethyl sulfide by eddy correlation and atmospheric pressure ionization mass spectrometry (APIMS), Journal of Geophysical Research-Atmospheres, 107(D24).

Barnard, W. R., M. O. Andreae, W. E. Watkins, H. Bingemer, and H. W. Georgii (1982), The flux of dimethylsulfide from the oceans to the atmosphere, Journal of Geophysical Research-Oceans and Atmospheres, 87(NC11), 8787-8793.

Bassett, M., and J. H. Seinfeld (1983), Atmospheric equilibrium model of sulfate and nitrate aerosols, Atmospheric Environment, 17(11), 2237-2252, doi: 10.1016/0004-6981(83)90221-4.

Bloomer, B. J., K. Y. Vinnikov, and R. R. Dickerson (2010), Changes in seasonal and diurnal cycles of ozone and temperature in the eastern U.S, Atmospheric Environment, 44(21–22), 2543-2551.

Bloomer, B. J., J. W. Stehr, C. A. Piety, R. J. Salawitch, and R. R. Dickerson (2009), Observed relationships of ozone air pollution with temperature and emissions, Geophysical Research Letters, 36(9), L09803.

Boersma, K. F., H. J. Eskes, and E. J. Brinksma (2004), Error analysis for tropospheric NO_2 retrieval from space, Journal of Geophysical Research: Atmospheres, 109(D4), D04311, doi:10.1029/2003JD003962.

Boersma, K. F., et al. (2007), Near-real time retrieval of tropospheric NO_2 from OMI, Atmos. Chem. Phys., 7(8), 2103-2118, doi:10.5194/acp-7-2103-2007.

Boersma, K. F., et al. (2011), An improved tropospheric NO_2 column retrieval algorithm for the ozone monitoring instrument, Atmos. Meas. Tech., 4(9), 1905-1928, doi:10.5194/amt-4-1905-2011.

Brent, L. C., et al. (2013), Evaluation of the use of a commercially available cavity ringdown absorption spectrometer for measuring NO_2 in flight, and observations over the Mid-Atlantic States, during DISCOVER-AQ, Journal of Atmospheric Chemistry, 1-19, doi:10.1007/s10874-013-9265-6.

Brunekreef, B., and S. T. Holgate (2002), Air pollution and health, Lancet, 360(9341), 1233-1242.

Bucsela, E. J., E. A. Celarier, M. O. Wenig, J. F. Gleason, J. P. Veefkind, K. F. Boersma, and E. J. Brinksma (2006), Algorithm for NO_2 vertical column retrieval from the ozone monitoring instrument, Geoscience and Remote Sensing, IEEE Transactions on, 44(5), 1245-1258, doi:10.1109/TGRS.2005.863715.

Camalier, L., W. Cox, and P. Dolwick (2007), The effects of meteorology on ozone in urban areas and their use in assessing ozone trends, Atmospheric Environment, 41(33), 7127-7137.

Chameides, W. L., et al. (1992), Ozone precursor relationships in the ambient atmosphere, Journal of Geophysical Research: Atmospheres, 97(D5), 6037-6055, doi:10.1029/91JD03014.

Charlson, R. J., J. E. Lovelock, M. O. Andreae, and S. G. Warren (1987), Oceanic phytoplankton, atmospheric sulfur, cloud albedo and climate, Nature, 326(6114), 655-661.

Chen, G., D. D. Davis, P. Kasibhatla, A. R. Bandy, D. C. Thornton, B. J. Huebert, A. D. Clarke, and B. W. Blomquist (2000), A study of DMS oxidation in the tropics: Comparison of christmas island field observations of DMS, SO_2, and DMSO with model simulations, Journal of Atmospheric Chemistry, 37(2), 137-160.

Chen, J., et al. (2009), The effects of global changes upon regional ozone pollution in the United States, Atmos. Chem. Phys., 9(4), 1125-1141.

Choi, Y., Y. Wang, T. Zeng, R. V. Martin, T. P. Kurosu, and K. Chance (2005), Evidence of lightning NO_x and convective transport of pollutants in satellite observations over North America, Geophysical Research Letters, 32(2), L02805, doi:10.1029/2004GL021436.

Choi, Y., Y. Wang, Q. Yang, D. Cunnold, T. Zeng, C. Shim, M. Luo, A. Eldering, E. Bucsela, and J. Gleason (2008a), Spring to summer northward migration of high O_3 over the western North Atlantic, Geophysical Research Letters, 35(4), L04818, doi:10.1029/2007GL032276.

Choi, Y., Y. Wang, T. Zeng, D. Cunnold, E.-S. Yang, R. Martin, K. Chance, V. Thouret, and E. Edgerton (2008b), Springtime transitions of NO_2, CO, and O_3 over North America: Model evaluation and analysis, Journal of Geophysical Research: Atmospheres, 113(D20), D20311, doi:10.1029/2007JD009632.

Clarke, A. D., et al. (2004), Size distributions and mixtures of dust and black carbon aerosol in Asian outflow: Physiochemistry and optical properties, Journal of Geophysical Research-Atmospheres, 109(D15).

Conley, S. A., I. Faloona, G. H. Miller, D. H. Lenschow, B. Blomquist, and A. Bandy (2009), Closing the dimethyl sulfide budget in the tropical marine boundary layer during the Pacific Atmospheric Sulfur Experiment, Atmos. Chem. Phys., 9(22), 8745-8756.

Covington, A. K., R. A. Robinson, and R. Thompson (1973), Osmotic and activity coefficients for aqueous methane sulfonic acid solutions at 25.deg, J. Chem. Eng. Data, 18(4), 422-423.

Dahneke, B. (1983), Simple kinetic theory of Brownian diffusion in vapors and aerosols, in Theory of Dispersed Multiphase Flow, edited by R.E. Meyer, pp. 97-133, Academic Press, New York.

Davis, D., G. Chen, P. Kasibhatla, A. Jefferson, D. Tanner, F. Eisele, D. Lenschow, W. Neff, and H. Berresheim (1998), DMS oxidation in the Antarctic marine boundary layer: Comparison of model simulations and held observations of DMS, DMSO, $DMSO_2$, H_2SO_4(g), MSA(g), and MSA(p), Journal of Geophysical Research, 103(D1), 1657-1678.

Davis, D., et al. (1999), Dimethyl sulfide oxidation in the equatorial Pacific: Comparison of model simulations with field observations for DMS, SO_2, H_2SO_4(g), MSA(g),

MS, and NSS, Journal of Geophysical Research-Atmospheres, 104(D5), 5765-5784.

Dawson, J.P., P.J. Adams, and S.N. Pandis (2007), Sensitivity of ozone to summertime climate in the Eastern USA: a modeling case study. Atmos. Environ. 41, 1494–1511.

De Arellano, J. V.-G., E. G. Patton, T. Karl, K. van den Dries, M. C. Barth, and J. J. Orlando (2011), The role of boundary layer dynamics on the diurnal evolution of isoprene and the hydroxyl radical over tropical forests, Journal of Geophysical Research-Atmospheres, 116, doi:D07304 10.1029/2010jd014857.

De Smedt, I., M. Van Roozendael, T. Stavrakou, J. F. Müller, C. Lerot, N. Theys, P. Valks, N. Hao, and R. van der A (2012), Improved retrieval of global tropospheric formaldehyde columns from GOME-2/MetOp-A addressing noise reduction and instrumental degradation issues, Atmos. Meas. Tech., 5(11), 2933-2949.

De Bruyn, W. J., J. A. Shorter, P. Davidovits, D. R. Worsnop, M. S. Zahniser, and C. E. Kolb (1994), Uptake of gas phase sulfur species methanesulfonic acid, dimethylsulfoxide, and dimethyl sulfone by aqueous surfaces, Journal of Geophysical Research: Atmospheres, 99(D8), 16927-16932.

Dieudonné, E., Ravetta, F., Pelon, J., Goutail, F., and Pommereau, J. P.: Linking NO2 surface concentration and integrated content in the urban developed atmospheric boundary layer, Geophysical Research Letters, 40, 1247-1251, 10.1002/grl.50242, 2013.

EPA (2015), National Emissions Inventory (NEI) Air Pollutant Emissions Trends Data, Available from http://www3.epa.gov/ttnchie1/trends/ (Accessed 30 September 2015)

Eskes, H. J., and K. F. Boersma (2003), Averaging kernels for DOAS total-column satellite retrievals, Atmos. Chem. Phys., 3(5), 1285-1291, doi:10.5194/acp-3-1285-2003.

Eyring, V., et al. (2013), Long-term ozone changes and associated climate impacts in CMIP5 simulations, Journal of Geophysical Research: Atmospheres, 118(10), 5029-5060.

Faloona, I., S. A. Conley, B. Blomquist, A. D. Clarke, V. Kapustin, S. Howell, D. H. Lenschow, and A. R. Bandy (2009), Sulfur dioxide in the tropical marine boundary layer: dry deposition and heterogeneous oxidation observed during the Pacific Atmospheric Sulfur Experiment, Journal of Atmospheric Chemistry, 63(1), 13-32.

Fiedler, V., et al. (2005), The contribution of sulphuric acid to atmospheric particle formation and growth: a comparison between boundary layers in Northern and Central Europe, Atmos. Chem. Phys., 5(7), 1773-1785, doi:10.5194/acp-5-1773-2005.

Froyd, K. D., D. M. Murphy, T. J. Sanford, D. S. Thomson, J. C. Wilson, L. Pfister, and L. Lait (2009), Aerosol composition of the tropical upper troposphere, Atmos. Chem. Phys., 9(13), 4363-4385.

Fiore, A. M., D. J. Jacob, B. D. Field, D. G. Streets, S. D. Fernandes, and C. Jang (2002), Linking ozone pollution and climate change: The case for controlling methane, Geophysical Research Letters, 29(19), 1919.

Fu, T.-M., D. J. Jacob, P. I. Palmer, K. Chance, Y. X. Wang, B. Barletta, D. R. Blake, J. C. Stanton, and M. J. Pilling (2007), Space-based formaldehyde measurements as constraints on volatile organic compound emissions in east and south Asia and implications for ozone, J. Geophys. Res., 112, D06312, doi:10.1029/2006JD007853.

Fu, T.-M., Y. Zheng, F. Paulot, J. Mao, and R. M. Yantosca (2015), Positive but variable sensitivity of August surface ozone to large-scale warming in the southeast United States, Nature Clim. Change, advance online publication.

Geleyn, J. F. (1981), in Workshop on Radiation and Cloud-Radiation Interaction in Numerical Modeling, Eur. Cent. for Medium-Range Weather Forecast, edited, Reading, UK.

Geron, C. D., D. Nie, R. R. Arnts, T. D. Sharkey, E. L. Singsaas, P. J. Vanderveer, A. Guenther, J. E. Sickles Ii, and T. E. Kleindienst (1997), Biogenic isoprene emission: Model evaluation in a southeastern United States bottomland deciduous forest, Journal of Geophysical Research: Atmospheres, 102(15), 18889-18901.

Gilliam, R. C., and J. E. Pleim (2010), Performance assessment of new land surface and planetary boundary layer physics in the WRF-ARW, Journal of Applied Meteorology and Climatology, 49, doi:10.1175/2009JAMC2126.1.

Gray, B. A., Y. Wang, D. Gu, A. Bandy, L. Mauldin, A. Clarke, B. Alexander, and D. D. Davis (2011), Sources, transport, and sinks of SO_2 over the equatorial Pacific during the Pacific Atmospheric Sulfur Experiment, Journal of Atmospheric Chemistry, 68(1), 27-53, doi:10.1007/s10874-010-9177-7.

Gu, D., Y. Wang, C. D. Smeltzer, and Z. Liu (2013), Reduction in NO_x emission trends over China: Regional and seasonal variations, Environ Sci Technol, doi:10.1021/es401727e.

Gu, D., Y. Wang, C. D. Smeltzer, and K. F. Boersma (2014), Anthropogenic emissions of NO_x over China: Reconciling the difference of inverse modeling results using GOME-2 and OMI measurements, Journal of Geophysical Research: Atmospheres, 119, doi: 10.1002/2014JD021644.

Guenther, A., T. Karl, P. Harley, C. Wiedinmyer, P. I. Palmer, and C. Geron (2006), Estimates of global terrestrial isoprene emissions using MEGAN (Model of Emissions of Gases and Aerosols from Nature), Atmos. Chem. Phys., 6(11), 3181-3210.

Hains, J. C., et al. (2010), Testing and improving OMI DOMINO tropospheric NO_2 using observations from the DANDELIONS and INTEX-B validation campaigns, Journal of Geophysical Research: Atmospheres, 115(D5), D05301, doi:10.1029/2009JD012399.

Heckel, A., S. W. Kim, G. J. Frost, A. Richter, M. Trainer, and J. P. Burrows (2011), Influence of low spatial resolution a priori data on tropospheric NO_2 satellite retrievals, Atmos. Meas. Tech., 4(9), 1805-1820, doi:10.5194/amt-4-1805-2011.

Heffter, J. L. (1980), Transport layer depth calculations, in Second Joint Conference on Applications of Air Pollution Meteorology, American Meteorological Society, New Orleans, LA.

Heland, J., H. Schlager, A. Richter, and J. P. Burrows (2002), First comparison of tropospheric NO_2 column densities retrieved from GOME measurements and in situ aircraft profile measurements, Geophysical Research Letters, 29(20), 1983, doi:10.1029/2002GL015528.

Hong, S.-Y., Y. Noh, and J. Dudhia (2006), A new vertical diffusion package with an explicit treatment of entrainment processes, Monthly Weather Review, 134(9), 2318-2341, doi: dx.doi.org/10.1175/MWR3199.1

Hoppel, W. A. (1987), Nucleation in the MSA water-vapor system, Atmospheric Environment, 21(12), 2703-2709.

Hu, X.-M., J. W. Nielsen-Gammon, and F. Zhang (2010), Evaluation of three planetary boundary layer schemes in the WRF model, Journal of Applied Meteorology and Climatology, 49(9), 1831-1844, doi:10.1175/2010jamc2432.1.

Hudson, J. G., and S. Noble (2009), CCN and cloud droplet concentrations at a remote ocean site, Geophysical Research Letters, 36(13), L13812.

Jacob, D. J., and D. A. Winner (2009), Effect of climate change on air quality, Atmospheric Environment, 43(1), 51-63.

Jacob, D. J., L. W. Horowitz, J. W. Munger, B. G. Heikes, R. R. Dickerson, R. S. Artz, and W. C. Keene (1995), Seasonal transition from NO_x- to hydrocarbon-limited conditions for ozone production over the eastern United States in September, Journal of Geophysical Research: Atmospheres, 100(D5), 9315-9324.

Janjić, Z. I. (1990), The step-mountain coordinate: physical package, Monthly Weather Review, 118(7), 1429-1443, doi: dx.doi.org/10.1175/1520-0493(1990)118<1429:TSMCPP>2.0.CO;2.

Johnson, C.E., W.J. Collins, D.S. Stevenson, and R.G. Derwent (1999), The relative roles of climate and emissions changes on future oxidant concentrations. J. Geophys. Res. 104, 18,631–18,645.

Kanaya, Y., M. Fukuda, H. Akimoto, N. Takegawa, Y. Komazaki, Y. Yokouchi, M. Koike, and Y. Kondo (2008), Urban photochemistry in central Tokyo: 2. Rates and regimes of oxidant (O_3 + NO_2) production, Journal of Geophysical Research: Atmospheres, 113(D6), D06301, doi:10.1029/2007JD008671.

Kleinman, L. I. (2005), A comparative study of ozone production in five U.S. metropolitan areas, Journal of Geophysical Research, 110, doi:10.1029/2004JD005096.

Knepp, T., et al. (2013), Estimating surface NO_2 and SO_2 mixing ratios from fast-response total column observations and potential application to geostationary missions, Journal of Atmospheric Chemistry, 1-26, doi:10.1007/s10874-013-9257-6.

Lamsal, L. N., R. V. Martin, A. Padmanabhan, A. van Donkelaar, Q. Zhang, C. E. Sioris, K. Chance, T. P. Kurosu, and M. J. Newchurch (2011), Application of satellite observations for timely updates to global anthropogenic NO_x emission inventories, Geophysical Research Letters, 38(5), L05810, doi:10.1029/2010GL046476.

Lee, Y. C., M. Wenig, and X. Yang (2009), The emergence of urban ozone episodes in autumn and air temperature rise in Hong Kong, Air Qual Atmos Health, 2(2), 111-121.

Lee-Taylor, J., S. Madronich, B. Aumont, A. Baker, M. Camredon, A. Hodzic, G. S. Tyndall, E. Apel, and R. A. Zaveri (2011), Explicit modeling of organic chemistry and secondary organic aerosol partitioning for Mexico City and its outflow plume, Atmos. Chem. Phys., 11(24), 13219-13241, doi:10.5194/acp-11-13219-2011.

Leibensperger, E. M., L. J. Mickley, and D. J. Jacob (2008), Sensitivity of US air quality to mid-latitude cyclone frequency and implications of 1980–2006 climate change, Atmos. Chem. Phys., 8(23), 7075-7086.

Leigh, R. J., G. K. Corlett, U. Friess, and P. S. Monks (2007), Spatially resolved measurements of nitrogen dioxide in an urban environment using concurrent multi-axis differential optical absorption spectroscopy, Atmos. Chem. Phys., 7(18), 4751-4762, doi:10.5194/acp-7-4751-2007.

Lin, M., A. M. Fiore, L. W. Horowitz, A. O. Langford, S. J. Oltmans, D. Tarasick, and H. E. Rieder (2015), Climate variability modulates western US ozone air quality in spring via deep stratospheric intrusions, Nat Commun, 6.

Lindinger, W., A. Hansel, and A. Jordan (1998), Proton-transfer-reaction mass spectrometry (PTR-MS): on-line monitoring of volatile organic compounds at pptv levels, Chemical Society Reviews, 27(5), 347-354.

Liu, S. C., et al. (1992), A study of the photochemistry and ozone budget during the Mauna Loa Observatory Photochemistry Experiment, Journal of Geophysical Research: Atmospheres, 97(D10), 10463-10471, doi:10.1029/91JD02298.

Liu, Z., et al. (2010), Evidence of Reactive Aromatics As a Major Source of Peroxy Acetyl Nitrate over China, Environ Sci Technol, 44(18), 7017-7022.

Liu, Z., et al. (2012a), Summertime photochemistry during CAREBeijing-2007: RO_x budgets and O_3 formation, Atmos. Chem. Phys., 12(16), 7737-7752, doi:10.5194/acp-12-7737-2012.

Liu, Z., et al. (2012b), Exploring the missing source of glyoxal (CHOCHO) over China, Geophysical Research Letters, 39(10), doi:10.1029/2012GL051645.

Liu, Z., Y. Wang, F. Costabile, A. Amoroso, C. Zhao, L. G. Huey, R. Stickel, J. Liao, and T. Zhu (2014), Evidence of aerosols as a media for rapid daytime HONO production over China, Environ Sci Technol, 48(24), 14386-14391, doi:10.1021/es504163z.

Mauldin, R. L., D. J. Tanner, J. A. Heath, B. J. Huebert, and F. L. Eisele (1999), Observations of H_2SO_4 and MSA during PEM-Tropics-A, Journal of Geophysical Research: Atmospheres, 104(D5), 5801-5816.

Mauldin, R. L., G. J. Frost, G. Chen, D. J. Tanner, A. S. H. Prevot, D. D. Davis, and F. L. Eisele (1998), OH measurements during the First Aerosol Characterization Experiment (ACE 1): Observations and model comparisons, Journal of Geophysical Research-Atmospheres, 103(D13), 16713-16729.

Millet, D. B., et al. (2006), Formaldehyde distribution over North America: Implications for satellite retrievals of formaldehyde columns and isoprene emission, J. Geophys. Res., 111, D24S02, doi:10.1029/2005JD006853.

Mellor, G. L., and T. Yamada (1982), Development of a turbulence closure model for geophysical fluid problems. Rev. Geophys., 20(4), 851–875, doi: 10.1029/RG020i004p00851.

Müller, J. F., Stavrakou, T., Wallens, S., De Smedt, I., Van Roozendael, M., Potosnak, M. J., Rinne, J., Munger, B., Goldstein, A., and Guenther, A. B.: Global isoprene emissions estimated using MEGAN, ECMWF analyses and a detailed canopy environment model, Atmos. Chem. Phys., 8, 1329-1341, 10.5194/acp-8-1329-2008, 2008.

Ng, N. L., et al. (2007), Effect of NO_x level on secondary organic aerosol (SOA) formation from the photooxidation of terpenes, Atmos. Chem. Phys., 7(19), 5159-5174, doi:10.5194/acp-7-5159-2007.

Nolte, C. G., A. B. Gilliland, C. Hogrefe, and L. J. Mickley (2008), Linking global to regional models to assess future climate impacts on surface ozone levels in the United States, Journal of Geophysical Research: Atmospheres, 113(D14), D14307.

Nowak, J. B., et al. (2001), Airborne observations of DMSO, DMS, and OH at marine tropical latitudes, Geophysical Research Letters, 28(11), 2201-2204.

Olszyna, K. J., M. Luria, and J. F. Meagher (1997), The correlation of temperature and rural ozone levels in southeastern U.S.A, Atmospheric Environment, 31(18), 3011-3022.

Oltmans, S. J., A. S. Lefohn, J. M. Harris, and D. S. Shadwick (2008), Background ozone levels of air entering the west coast of the US and assessment of longer-term changes, Atmospheric Environment, 42(24), 6020-6038.

Palmer, P. I., D. J. Jacob, A. M. Fiore, R. V. Martin, K. Chance, and T. P. Kurosu (2003), Mapping isoprene emissions over North America using formaldehyde column observations from space, J. Geophys. Res., 108(D6), 4180, doi:10.1029/2002JD002153.

Palmer, P. I., Abbot, D. S., Fu, T.-M., Jacob, D. J., Chance, K., Kurosu, T. P., Guenther, A., Wiedinmyer, C., Stanton, J. C., Pilling, M. J., Pressley, S. N., Lamb, B., and Sumner, A. L.: Quantifying the seasonal and interannual variability of North American isoprene emissions using satellite observations of the formaldehyde column, Journal of Geophysical Research: Atmospheres, 111, D12315, 10.1029/2005JD006689, 2006.

Pegoraro, E., A. Rey, G. Barron-Gafford, R. Monson, Y. Malhi, and R. Murthy (2005), The Interacting Effects of Elevated Atmospheric CO_2 Concentration, Drought and Leaf-to-Air Vapour Pressure Deficit on Ecosystem Isoprene Fluxes, Oecologia, 146(1), 120-129.

Pegoraro, E., M. J. Potosnak, R. K. Monson, A. Rey, G. Barron-Gafford, and C. B. Osmond (2007), The effect of elevated CO_2, soil and atmospheric water deficit and seasonal phenology on leaf and ecosystem isoprene emission, Functional Plant Biology, 34(9), 774-784.

Petritoli, A., P. Bonasoni, G. Giovanelli, F. Ravegnani, I. Kostadinov, D. Bortoli, A. Weiss, D. Schaub, A. Richter, and F. Fortezza (2004), First comparison between ground-based and satellite-borne measurements of tropospheric nitrogen dioxide

in the Po basin, Journal of Geophysical Research: Atmospheres, 109(D15), D15307, doi:10.1029/2004JD004547.

Pier, P. A. (1995), Isoprene emission rates from northern red oak using a whole-tree chamber, Atmospheric Environment, 29(12), 1347-1353.

Pleim, J. E. (2007), A combined local and nonlocal closure model for the atmospheric boundary layer. Part II: Application and evaluation in a mesoscale meteorological model, Journal of Applied Meteorology and Climatology, 46(9), 1396-1409, doi:10.1175/JAM2534.1.

Pleim, J. E. (2011), Comment on "Simulation of surface ozone pollution in the Central Gulf Coast region using WRF/Chem model: Sensitivity to PBL and land surface physics", Advances in Meteorology, 2011, 1-3, doi:10.1155/2011/464753.

Potosnak, M. J., L. LeStourgeon, S. G. Pallardy, K. P. Hosman, L. Gu, T. Karl, C. Geron, and A. B. Guenther (2014), Observed and modeled ecosystem isoprene fluxes from an oak-dominated temperate forest and the influence of drought stress, Atmospheric Environment, 84(0), 314-322.

Rasmussen, D. J., A. M. Fiore, V. Naik, L. W. Horowitz, S. J. McGinnis, and M. G. Schultz (2012), Surface ozone-temperature relationships in the eastern US: A monthly climatology for evaluating chemistry-climate models, *Atmospheric Environment, 47*(0), 142-153.

Rasmussen, D.J., J. Hu, A. Mahmud, and M. J. Kleeman (2013), The ozone-climate penalty: past, present, and future, Environ Sci Technol, 47(24), 14258-14266, doi:10.1021/es403446m.

Racherla, P. N. and P. J.: Adams (2008), The response of surface ozone to climate change over the Eastern United States, Atmos. Chem. Phys., 8, 871-885, doi:10.5194/acp-8-871-2008.

Reich, P. B., and R. G. Amundson (1985), Ambient Levels of Ozone Reduce Net Photosynthesis in Tree and Crop Species, Science, 230(4725), 566-570.

Ren, X. (2003), OH and HO_2 chemistry in the urban atmosphere of New York City, Atmospheric Environment, 37, doi:10.1016/S1352-2310(03)00459-X.

Ridley, B. A., F. E. Grahek, and J. G. Walega (1992), A small, high-sensitivity, medium-response ozone detector suitable for measurements from light aircraft, Journal of Atmospheric and Oceanic Technology, 9(2), 142-148.

Russell, A. R., A. E. Perring, L. C. Valin, E. J. Bucsela, E. C. Browne, P. J. Wooldridge, and R. C. Cohen (2011), A high spatial resolution retrieval of NO_2 column densities from OMI: method and evaluation, Atmos. Chem. Phys., 11(16), 8543-8554, doi:10.5194/acp-11-8543-2011.

Sachse, G.W., Hill, G.F. , Wade, L.O. and Perry, M.G (1987), Fast response, high precision carbon monoxide sensor using a tunable diode laser absorption technique, J. Geophys. Res., 92, 2071 –2081.

Saha, S., et al. (2010), The NCEP Climate Forecast System Reanalysis, Bulletin of the American Meteorological Society, 91(8), 1015-1057.

Sander, S. P., Abbatt, J., Barker, J. R., Burkholder, J. B., Friedl,R. R., Golden, D. M., Huie, R. E., Kolb, C. E., Kurylo, M. J.,Moortgat, G. K., Orkin, V. L., and Wine, P. H. (2011), Chemical kinetics and photochemical data for use in atmospheric studies, Evaluation No.17, JPL Publication 10-6Rep., Jet Propulsion Laboratory, Pasadena, CA, USA.

Schweitzer, F., L. Magi, P. Mirabel, and C. George (1998), Uptake Rate Measurements of Methanesulfonic Acid and Glyoxal by Aqueous Droplets, The Journal of Physical Chemistry A, 102(3), 593-600.

Seinfeld, J. H., S. N. Pandis (2006), Atmospheric chemistry and physics: from air pollution to climate change, Wiley, New York.

Shin, H. H., and S.-Y. Hong (2011), Intercomparison of planetary boundary-layer parametrizations in the WRF model for a single day from CASES-99, Boundary-Layer Meteorology, 139, doi:10.1007/s10546-010-9583-z.

Shirley, T. R., et al. (2006), Atmospheric oxidation in the Mexico City Metropolitan Area (MCMA) during April 2003, Atmos. Chem. Phys., 6(9), 2753-2765, doi:10.5194/acp-6-2753-2006.

Sillman, S. (2000), Ozone production efficiency and loss of NO_x in power plant plumes: Photochemical model and interpretation of measurements in Tennessee, Journal

of Geophysical Research-Atmospheres, 105(D7), 9189-9202, doi:10.1029/1999jd901014.

Spicer, C. W. (1982), Nitrogen-oxide reactions in the urban plume of Boston, Science, 215(4536), 1095-1097, doi:10.1126/science.215.4536.1095.

Stauffer, R., Thompson, A., Martins, D., Clark, R., Goldberg, D., Loughner, C., Delgado, R., Dickerson, R., Stehr, J., and Tzortziou, M.: Bay breeze influence on surface ozone at Edgewood, MD during July 2011, Journal of Atmospheric Chemistry, 1-19, 10.1007/s10874-012-9241-6, 2012.

Steiner, A. L., A. J. Davis, S. Sillman, R. C. Owen, A. M. Michalak, and A. M. Fiore (2010), Observed suppression of ozone formation at extremely high temperatures due to chemical and biophysical feedbacks, Proceedings of the National Academy of Sciences, 107(46), 19685-19690.

Valks, P., G. Pinardi, A. Richter, J. C. Lambert, N. Hao, D. Loyola, M. Van Roozendael, and S. Emmadi (2011), Operational total and tropospheric NO_2 column retrieval for GOME-2, Atmos. Meas. Tech. Discuss., 4(2), 1617-1676, doi:10.5194/amtd-4-1617-2011.

Voulgarakis, A., O. Wild, N. H. Savage, G. D. Carver, and J. A. Pyle (2009), Clouds, photolysis and regional tropospheric ozone budgets, Atmos. Chem. Phys., 9, 8235-8246, doi:10.5194/acp-9-8235-2009.

Vukovich, F. M., and J. Sherwell (2003), An examination of the relationship between certain meteorological parameters and surface ozone variations in the Baltimore–Washington corridor, Atmospheric Environment, 37(7), 971-981.

Wang, Y., et al. (2001), Factors controlling tropospheric O_3, OH, NO_x and SO_2 over the tropical Pacific during PEM-Tropics B, Journal of Geophysical Research: Atmospheres, 106(D23), 32733-32747.

Wang, Y. H., Y. Choi, T. Zeng, D. Davis, M. Buhr, L. G. Huey, and W. Neff (2007), Assessing the photochemical impact of snow NO_x emissions over Antarctica during ANTCI 2003, Atmospheric Environment, 41(19), 3944-3958.

Wang, Y., D. J. Jacob, and J. A. Logan (1998), Global simulation of tropospheric O_3-NO_x-hydrocarbon chemistry: 3. Origin of tropospheric ozone and effects of

nonmethane hydrocarbons, J. Geophys. Res., 103, 10,757 –10,767, doi:10.1029/98JD00156.

Weber, R. J., K. Moore, V. Kapustin, A. Clarke, R. L. Mauldin, E. Kosciuch, C. Cantrell, F. Eisele, B. Anderson, and L. Thornhill (2001), Nucleation in the equatorial Pacific during PEM-Tropics B: Enhanced boundary layer H_2SO_4 with no particle production, Journal of Geophysical Research-Atmospheres, 106(D23), 32767-32776.

Weibring, P., D. Richter, J. G. Walega, L. Rippe, and A. Fried (2010), Difference frequency generation spectrometer for simultaneous multispecies detection, Opt. Express, 18(26), 27670-27681, doi:10.1364/OE.18.027670.

Wu, S., L. J. Mickley, D. J. Jacob, D. Rind, and D. G. Streets (2008), Effects of 2000–2050 changes in climate and emissions on global tropospheric ozone and the policy-relevant background surface ozone in the United States, Journal of Geophysical Research: Atmospheres, 113(D18), D18312.

Xie, B., J. C. H. Fung, A. Chan, and A. Lau (2012), Evaluation of nonlocal and local planetary boundary layer schemes in the WRF model, Journal of Geophysical Research: Atmospheres, 117(D12), doi:10.1029/2011jd017080.

Xu, L., et al. (2015), Effects of anthropogenic emissions on aerosol formation from isoprene and monoterpenes in the southeastern United States, Proceedings of the National Academy of Sciences, 112(1), 37-42.

Yang, Q., D. M. Cunnold, Y. Choi, Y. Wang, J. Nam, H.-J. Wang, L. Froidevaux, A. M. Thompson, and P. K. Bhartia (2010), A study of tropospheric ozone column enhancements over North America using satellite data and a global chemical transport model, Journal of Geophysical Research: Atmospheres, 115(D8), D08302, doi:10.1029/2009JD012616.

Yerramilli, A., V. S. Challa, V. B. R. Dodla, H. P. Dasari, J. H. Young, C. Patrick, J. M. Baham, R. L. Hughes, M. G. Hardy, and S. J. Swanier (2010), Simulation of surface ozone pollution in the central Gulf coast region using WRF/Chem model: sensitivity to PBL and land surface physics, Advances in Meteorology, 2010, 1-24, doi:10.1155/2010/319138.

Zhang, Y., Y. Wang, B. A. Gray, D. Gu, L. Mauldin, C. Cantrell, and A. Bandy (2014), Surface and free tropospheric sources of methanesulfonic acid over the tropical

Pacific Ocean, Geophysical Research Letters, 41(14), 5239-5245, doi:10.1002/2014GL060934.

Zhao, C., and Y. Wang (2009), Assimilated inversion of NO_x emissions over east Asia using OMI NO2 column measurements, Geophysical Research Letters, 36(6), L06805, doi:10.1029/2008GL037123.

Zhao, C., Y. Wang, Y. Choi, and T. Zeng (2009a), Summertime impact of convective transport and lightning NO_x production over North America: modeling dependence on meteorological simulations, Atmos. Chem. Phys., 9(13), 4315-4327, doi:10.5194/acp-9-4315-2009.

Zhao, C., Y. Wang, and T. Zeng (2009b), East China plains: A "basin" of ozone pollution, Environ Sci Technol, 43(6), 1911-1915, doi:10.1021/es8027764.

Zhao, C., Y. Wang, Q. Yang, R. Fu, D. Cunnold, and Y. Choi (2010), Impact of East Asian summer monsoon on the air quality over China: View from space, Journal of Geophysical Research: Atmospheres, 115(D9), D09301, doi:10.1029/2009JD012745.

Zhu, J., X.-Z., Liang (2013), Impacts of the Bermuda High on Regional Climate and Ozone over the United States. J. Climate, 26, 1018–1032.

Zhu, L., A. Nenes, P. H. Wine, and J. M. Nicovich (2006), Effects of aqueous organosulfur chemistry on particulate methanesulfonate to non-sea salt sulfate ratios in the marine atmosphere, Journal of Geophysical Research-Atmospheres, 111(D5).

VITA

Yuzhong Zhang

Yuzhong Zhang was born in Hangzhou, China. He received a B.S. in Environmental Sciences from Peking University, Beijing, China in 2010 before coming to Georgia Tech to pursue a doctorate in Atmospheric Science. When he is not working on his research, Mr. Zhang enjoys reading, playing tennis, and practicing Chinese calligraphy.